

High Resolution Digital Surface Model (DSM) to Support Modelling of Urban Flooding

Dissertation

Submitted to and approved by the
Faculty of Civil Engineering
University of Kaiserslautern

in candidacy for the degree of a
Doktor-Ingenieur(Dr.-Ing.)

By

Md. Aktaruzzaman

Kaiserslautern 2011

(D 386)

High Resolution Digital Surface Model (DSM) to Support Modelling of Urban Flooding

Dissertation

Submitted to and approved by the
Faculty of Civil Engineering
University of Kaiserslautern

in candidacy for the degree of a
Doktor-Ingenieur(Dr.-Ing.)

By

Md. Aktaruzzaman

Kaiserslautern 2011

(D 386)

Oral examination on September 6, 2011

Chairman of the examination committee:

Prof. Dr.-Ing. Klaus Wassermann

Professorial advisors:

Prof. Dr.-Ing. Theo G. Schmitt

Prof. Dr. Hans Hagen

Acknowledgement

I am highly grateful to my supervisor Prof. Dr.-Ing. Theo G. Schmitt for his continual mentoring and support during the last three years period of this dissertation. I thank him for the continuous guidance and advice with which my dissertation has reached its success. I especially thank Prof. Dr. Hans Hagen for giving me the opportunity to pursue my research work within the IRTG. I acknowledge financial support of German Research Foundation (DFG) as a framework of International Research Training Group IRTG 1131 of TU Kaiserslautern. I am thankful to Prof. Subhrajit Guhathakurta, Prof. Soe W. Myint and Prof. David Pijawka for their support during my stay in Arizona State University.

I would like to thank M.Sc. Md. Khalaquzzaman for his valuable discussions on MATLAB. I would also like to thank Dr.-Ing. Tanvir Hussain, Dr.-Ing. Inga Scheler and Dr. Sebastian Thelen for their help to my dissertation in various ways. I want to express my thanks to my colleagues at SIWAWI and IRTG with whom I had wonderful time in the past three years. Special thanks to Christian Scheid and Martin Thomas from SIWAWI for their valuable comments in my research work. I want to express my special thanks to Mr. Daniel Engel and Mrs. Lucie Legay from DHI, Syke, Germany, for providing me MIKE FLOOD software license.

I want to express my special thanks to Mr. David Mueller, Mr. Uwe Schmeer and Mr. Hans-Peter Frohberger from Stadt Kaiserslautern for their support in providing various formats of topographic datasets of Kaiserslautern city. Finally, I want to thank my family for their support and encouragement.

Md. Aktaruzzaman
01/07/11, Kaiserslautern

Abstract

This research work focuses on the generation of a high resolution digital surface model featuring complex urban surface characteristics in order to enrich the database for runoff simulations of urban drainage systems. The discussion of global climate change and its possible consequences have taken centre stage over the last decade. Global climate change has triggered more erratic weather patterns by causing severe and unpredictable rainfall events in many parts of the world. The incidence of more frequent rainfall has led to the problem of increased flooding in urban areas. The increased property values of urban structures and threats to people's personal safety have hastened the demand for a detailed urban drainage simulation model for accurate flood prediction. Although the use of 2D hydraulic modelling approach in rural floodplains is in practice for quite a long time, the use of the same approach in urban floodplains is still in its infancy. The reason is mainly due to the lack of a high resolution topographic model describing urban surface characteristics properly.

High resolution surface data describing hydrologic and hydraulic properties of complex urban areas are the prerequisite to more accurately describing and simulating the flood water movement and thereby taking adequate measures against urban flooding. Airborne LiDAR (Light detection and ranging) is an efficient way of generating a high resolution Digital Surface Model (DSM) of any study area. The processing of high-density and large volume of unstructured LiDAR data is a difficult and time-consuming task towards generating fine resolution spatial databases when considering only human intervention. The application of robust algorithms in terms of processing this massive volume of data can significantly reduce the data processing time and thereby increase the degree of automation as well as accuracy.

This research work presents a number of techniques pertaining to processing, filtering and classification of LiDAR point data in order to achieve higher degree of automation and accuracy towards generating a high resolution urban surface model. This research work also describes the use of ancillary datasets such as aerial images and topographic maps in combination with LiDAR data for feature detection and surface characterization. The integration of various data sources facilitates detailed modelling of street networks and accurate detection of various urban surface types (e.g. grasslands, bare soil and impervious surfaces). While the accurate characterization of various surface types contributes to the better modelling of rainfall runoff processes, the application of LiDAR-derived fine resolution DSM serves as input to 2D hydraulic models and capable of simulating surface flooding scenarios in cases the sewer systems are surcharged.

Thus, this research work develops high resolution spatial databases aiming at improving the accuracy of hydrologic and hydraulic databases of urban drainage systems. Later, these databases are given as input to a standard flood simulation software in order to: 1) test the suitability of the databases for running the simulation; 2) assess the performance of the hydraulic capacity of urban drainage systems and 3) predict and visualize the surface flooding scenarios in order to take necessary flood protection measures.

Contents

List of Figures	v
List of Tables	x
Terms and Abbreviations	xi
List of Symbols	xiii
1 Introduction	1
1.1 Motivation	1
1.2 Problem statement	2
1.3 Research objectives	5
1.4 Proposed approach	5
1.5 Organization of the dissertation	7
2 Literature review	9
2.1 Urban drainage models	10
2.2 LiDAR data to generate high resolution DSM	14
2.3 Filtering algorithms of LiDAR data	16
2.4 The identification of objects (buildings and trees)	20
2.5 Street/road detection	24
2.6 Impervious (paved) and pervious (unpaved) surface detection	29
3 Materials and data types	33
3.1 Introduction	33
3.2 Study area	33
3.3 LiDAR data	34
3.4 Aerial images	36
3.5 Topographic maps	36

3.6	Image and LiDAR data co-registration	38
3.7	Accuracy assessment and error matrix approach	39
3.7.1	Selecting sampling scheme	40
3.7.2	Error matrix computation and analysis	40
3.8	Software packages	42
3.8.1	ArcGIS	42
3.8.2	MATLAB	42
3.8.3	ECognition/Definiens	43
3.8.4	MIKE FLOOD	43
3.9	Conclusion	43
4	Filtering LiDAR data	45
4.1	Introduction	45
4.2	Proposed algorithm	45
4.2.1	Selecting the block size	46
4.2.2	Standard plane equation in 3D space	47
4.2.3	Selecting points with minimum elevations within a block	49
4.2.4	Fitting the plane	49
4.3	Results and discussions	52
4.3.1	Alcatraz study area	52
4.3.2	Sensitivity of the filtering algorithm	54
4.3.3	Casimirring study area	55
4.3.4	Sensitivity of the algorithm on threshold selection	57
4.4	Conclusion	59
5	Object classification	60
5.1	Introduction	60
5.2	Proposed methods for object classification	60
5.3	Object clustering	62
5.4	Building and tree classification	64
5.4.1	Pseudo-gridding	64
5.4.2	Planar surface analysis	71
5.5	Detection of building outlines	87
5.5.1	Separation of building points	87
5.5.2	Cleaning the small clusters	87
5.5.3	Approximating boundary outlines	88
5.6	Conclusion	90

6	Street extraction and 3D modelling	92
6.1	Introduction	92
6.2	Street as an open channel	92
6.3	Data types and sources	94
6.4	Methodology	94
6.5	Street points extraction	95
6.5.1	Point-in-polygon algorithm	95
6.5.2	Dense polygon boundary points generation	97
6.6	Street connectivity (topology) construction	99
6.6.1	Detection of centreline	99
6.6.2	Construction of street connectivity	100
6.7	Distinguishing the boundary points	102
6.8	Detection of inner boundary lines	104
6.8.1	Street kerb detection	104
6.8.2	Delineation of street kerb	105
6.9	Reconstruction of street surfaces	107
6.9.1	An ideal street model	107
6.9.2	Assigning heights to centrelines and sidelines	107
6.10	Modelling of street junctions	111
6.11	Application	112
6.12	Validation	115
6.13	Limitations	117
6.14	Summary	117
7	Impervious(paved) and pervious(unpaved) surface detection	120
7.1	Introduction	120
7.2	Overall approach	120
7.2.1	Image layer stacking	121
7.2.2	Chessboard segmentation	123
7.2.3	Selection of region of interest (ROI)	124
7.2.4	Multiresolution segmentation	125
7.2.5	Rule-set development	127
7.2.6	Classification results	128
7.2.7	Accuracy of the final map	130
7.3	Application to Casimirring study area	132
7.4	Differentiating grassland and bare soil	135

7.5	Conclusion	136
8	Resulting data model	139
8.1	Introduction	139
8.2	DSM generation	140
8.3	Qualitative assessment	144
8.4	Preparing the land use and land cover (LULC) map	144
8.5	Running the simulation	146
8.5.1	MOUSE module	147
8.5.2	MIKE 21 module	151
8.5.3	Coupling 1D and 2D flow	151
8.5.4	Simulation and results	152
8.6	Application to Casimirring study area	154
8.7	Summary	156
9	Summary and recommendations	160
9.1	Summary	160
9.1.1	LiDAR data processing	161
9.1.2	Object classification	161
9.1.3	3D street modelling	162
9.1.4	Pervious (unpaved) and impervious (paved) surface detection .	163
9.1.5	Resulting/integrated data model	163
9.2	Recommendations / Future needs	164
	References	166

List of Figures

1.1	Overall workflow to generate high resolution digital surface models. . .	6
2.1	A typical airborne LiDAR system mounted on the aircraft with its embedded components (www.fs.fed.us).	15
2.2	Filtering of LiDAR point data.	17
2.3	Filtering technique by surface fitting approach.	19
2.4	Detection of simple horizontal curve (Easa et al. [38]).	27
2.5	Different types of paved surfaces.	29
3.1	Aerial image of the Alcatraz dataset (a) and a part of the Casimirring dataset (b).	34
3.2	The citymap of Kaiserslautern city and the location of the study areas.	35
3.3	LiDAR elevation data (a) and intensity data (b) of the Alcatraz study area.	35
3.4	High resolution image capturing soccer players (a) and detailed street view (b).	36
3.5	Topographic map of street networks (a) and buildings (b).	37
3.6	Topographic map of buildings (a) and streets (b) overlaid on the aerial image.	38
3.7	Co-registration of LiDAR data and aerial image: LiDAR point data overlaid on the building before (a) and after (b) performing image co-registration technique.	39
4.1	The concept of creating surface block. $P_1P_2P_3P_4$ is the whole study area and $abcd$ is one block within the study area.	48
4.2	Detection of minimum elevation point along the borders. Here surface block border P_4P_1 has minimum elevation point at B.	50
4.3	Flowchart of plane fitting algorithm.	51
4.4	Separation of non-ground points greater than the threshold (Δh) from the plane.	52
4.5	Cross-sectional profile of digital surface model of Alcatraz study area.	53

4.6	Segmentation of LiDAR point data into objects (blue) and terrain (red) using plane fitting algorithm.	53
4.7	Influence of height threshold in object separation.	55
4.8	Cross-sectional profile of digital surface model of Casimirring study area.	56
4.9	Segmented LiDAR data into ground (red) and non-ground (blue) points (a). The aerial image of the Casimirring study area (b).	57
4.10	Effect of thresholding in object separation in Casimirring dataset: Higher threshold extracts coarse objects information (a). Smaller threshold extracts dense object information (b).	58
5.1	Extracted objects appearing as clusters (left) and enlarged view of an object (right).	63
5.2	Region-growing clustering algorithm. The blue points are the algorithm termination points.	63
5.3	Concept of pseudo-gridding.	66
5.4	Flowchart of pseudo-gridding algorithm.	67
5.5	Spectral information integration (SII) technique. A building object with misclassified points i.e., the blue points (a). SII technique fixes the misclassified points (b).	69
5.6	Alcatraz dataset. Aerial image of the study area at Alcatraz (244 m x 177 m) (a). Classified buildings (red) and trees (blue) with pseudo-gridding algorithm (b).	69
5.7	Casimirring dataset. Aerial image of relatively larger study area at Casimirring (300 m x 516 m) (a). Classified buildings (red) and trees (blue) with pseudo-gridding algorithm (b).	71
5.8	Flowchart of the region-growing segmentation.	76
5.9	LiDAR points of a building object overlaid on the aerial image (a). Region-growing segmentation algorithm subdivides the point clouds into 11 regions (b).	77
5.10	From point cloud to classified object.	78
5.11	Segmentation and separation of roof planes.	83
5.12	Flowchart of plane separating algorithm.	84
5.13	Classified map of Alcatraz dataset by applying planar surface analysis.	85
5.14	Aerial image of Casimirring study area (a) and classified map of Casimirring dataset by applying planar surface analysis (b).	86
5.15	Roofs under different conditions: a pyramid roof (a), a hipped roof (b) and a roof covered by trees (c).	86

5.16	Classified dataset featuring buildings and trees (a) and only building (b).	88
5.17	Classified building objects only after removing small objects.	89
5.18	Approximation of building outline.	89
5.19	Validation of approximated building outlines.	90
6.1	Cross-section of a rectangular open channel.	93
6.2	2D topographic map (a) and aerial photograph with clipped street network (b) of the study site.	94
6.3	Workflow of 3D street network modelling.	96
6.4	Implementation of the Point-in-polygon (PIP) algorithm.	97
6.5	Application of PIP algorithm.	98
6.6	Topographic map of a street network with coarse boundary points (a); Dense boundary point generation with linear interpolation (b).	98
6.7	Detection of centreline in the street network.	99
6.8	Representation of the connectivity matrix.	100
6.9	Detection of junction point at the intersection.	102
6.10	Distinguishing left-side and right-side boundary points.	103
6.11	Clipped aerial image of a street segment (a) and detected edges (b).	105
6.12	Mapping of detected edges from pixel domain to feature space (a) and interpolated boundary and kerb line (b).	106
6.13	An ideal street cross-section.	107
6.14	Formation of rectangular blocks.	108
6.15	Planimetric view of a street segment with boundary, kerb and centreline points.	108
6.16	Threshold set up and removing of outliers.	110
6.17	Assigning height value to the centreline point.	110
6.18	3D visualization of a junction point with detailed sidewalks, kerbs and traffic lanes information.	111
6.19	Modelling of the street junction.	113
6.20	Planimetric view of the modelled street network at Alcatraz area.	114
6.21	Highlighting a boundary line and a centreline for generating height profile (a); Height profile of the highlighted street segment (b).	114
6.22	Planimetric view of a relatively complex street network near Casimir-ring after the application of the 3D reconstruction techniques.	115
6.23	Differences in ground truth height and calculated height of Alcatraz street model.	116

6.24	Differences in ground truth height and calculated height of Casimir-ring street model.	116
6.25	Shift in kerb line to accommodate the parking place next to the street.	118
7.1	The work flow of pervious and impervious surface detection.	122
7.2	Stacking of image layers: Aerial image of the Alcatraz study area with RGB layers (a) and LiDAR-derived intensity layer (b).	122
7.3	Example of chessboard segmentation.	123
7.4	Masking out the buildings and streets in the aerial image of the Alcatraz study area. Topographic map of buildings and streets (a). Masked area highlighted in yellow (b).	124
7.5	Detection of region of interest: a subset of the study area featuring region of interest (ROI) in maroon (a). Multiresolution segmentation applied only in the ROI, excluding areas covered by buildings and streets (b).	125
7.6	Multiresolution segmentation at different scale parameters: scale parameter 20 (a); Scale parameter 70 (b).	127
7.7	Detection of grasslands under the shadow: two types of surfaces, e.g. concrete and grassland under the shadow cast by the buildings (a); a threshold of the blue band value can separate the grassland from the concrete under the shadow (b).	129
7.8	Detection of impervious areas: A subset of the study area featuring impervious areas and grasslands (a). Expert system rule-set 2 detects most of the impervious areas excluding shadow-covered impervious areas (highlighted by zooming in) (b).	131
7.9	Classified maps after integrating different rule-sets: A subset image of the study area (a); detection of impervious areas under the shadows (b). Detection of impervious areas exposed to sun (in red) (c); resultant classification (d).	132
7.10	Detection of pervious and impervious areas in the Alcatraz dataset after masking out buildings and streets.	133
7.11	Pervious and impervious surface detection in the Casimirring area. . .	134
7.12	Trees with reddish leaves (a) are classified as impervious (b) surface. .	134
7.13	Aerial image with exposed soils (a) and classified image with soils + impervious surfaces (red) and grasses (green) (b).	136
7.14	Aerial image with exposed soils, impervious surfaces and grasses (a) and classified image with soils (red), impervious (yellow) and grasses (b).	137
7.15	Aerial photo of the Harzhübel area (a) and the classified image after the application of OBIA approach (b).	138

8.1	Workflow of DSM generation from LiDAR points.	141
8.2	Perspective view of different topographic layers.	141
8.3	Schematic diagram of natural neighbour interpolation.	143
8.4	Grid/raster representation of the Alcatraz study area.	143
8.5	Qualitative assessment of the generated DSM.	145
8.6	LULC map in vector format: buildings (maroon), streets (cyan), paved (red) and unpaved (green) surface.	146
8.7	Setup of MOUSE nodes and links of Alcatraz study area.	148
8.8	Delineation of catchment and sub-catchments of the region of interest.	149
8.9	The rainfall data used for the flood simulation.	150
8.10	Importing DSM and selection of model domain.	152
8.11	Coupling between the nodes and the surface model.	153
8.12	Extent of flood inundation at four different simulation stages (Alca- traz study area).	154
8.13	Flood water escaping into private ground from the street.	155
8.14	The interpolated DSM (a) and land cover maps of the Casimirring area.	156
8.15	Setup of sewer networks and discretization of catchment of the Casimir- ring area.	157
8.16	Results of the flood simulation in the Casimirring area at four different stages.	158
8.17	Event of flooding in one of the streets in Casimirring area (a) and the aerial image of that street (b).	159

List of Tables

3.1	An error matrix of four classes	41
4.1	Error matrix of Alcatraz dataset for filtering algorithm.	54
4.2	Calculation of various accuracies of Alcatraz area.	54
4.3	Error matrix of Casimirring area for filtering algorithm.	56
4.4	Calculation of various accuracies of Casimirring area.	57
5.1	Error matrix of D1 dataset for pseudo-gridding algorithm.	70
5.2	Error matrix of D2 dataset for pseudo-gridding algorithm.	70
5.3	Calculation of ξ values for sample objects.	82
5.4	Error matrix of D1 dataset for planar surface analysis.	84
5.5	Error matrix of D2 dataset for planar surface analysis.	85
7.1	Expert system rule-sets developed for the Alcatraz area.	128
7.2	Error matrix calculation for verifying surface classification accuracy for Alcatraz area.	131
7.3	Error matrix calculation for verifying surface classification accuracy for Casimirring area.	133
7.4	Expert systems rule-sets for Harzhübel study area.	135
7.5	Error matrix calculation for verifying surface classification accuracy for Harzhübel area.	137

Terms and Abbreviations

DEM:

DEM is an acronym for digital elevation model. The definition of DEM is equivalent to that of DSM meaning both DEM and DSM contains surface information of the earth including objects on top of it.

DHI:

Danish Hydraulic Institute is an independent and international consulting organization dealing with mainly water related issues. This institute has developed a number of software tools for the purpose of modelling the water of the world.

DSM:

DSM is an acronym for digital surface model. A digital surface model represents height information of the earth surface including the objects such as, buildings, trees, bridges, etc. on it.

DTM:

DTM is an acronym for digital terrain model. A digital terrain model represents height information of the bare earth surface excluding buildings, trees and other objects.

EXTRAN:

EXTRAN is a 1D hydraulic flow routine model for open channel and/or closed conduit systems. EXTRAN is developed by Storm Water Management Model of United States Environmental Protection Agency (EPA-SWMM).

IKONOS:

A commercial satellite responsible for earth observation and offers satellite imagery at 1m (panchromatic) and 4m (multispectral) spatial resolution.

ISODATA

Isodata is an acronym for Iterative Self-Organizing Data Analysis Techniques. This is an unsupervised clustering algorithm.

LiDAR

LiDAR is an acronym for Light Detection and Ranging. This is an active remote sensing technique used for capturing the topographic elevation data.

LULC:

LULC is an acronym for Land Use and Land Cover. LULC refers to a database of land surface categories which is derived

MIKE 11/21:

MIKE 11 and MIKE 21 are the software tools for modelling 1D and 2D flow respectively. Both of the tools are developed by DHI.

MOUSE:

This is a software tool responsible for simulating pipe flows of an urban drainage network and also developed by DHI.

OBIA:

Object-based Image Analysis approach to deal with high resolution imagery for accurate land cover classification.

QUICKBIRD:

A commercial satellite responsible for earth observation and offers satellite imagery at 0.6m (panchromatic) and 2.6m (multispectral) spatial resolution.

SOBEK:

This is a software tool developed by Delft hydraulic software and responsible for 1D and 2D flood modelling.

List of Symbols

(x, y, z)	three coordinates of lidar points in 3-D Cartesian space \mathcal{R}^3
(x, y)	two coordinates of a point in 2-D Cartesian space \mathcal{R}^2
Z_{ori}	real-world elevation of a point on earth surface
Z_{ori}	calculated elevation of a point using 3D plane equation
Δh	height threshold value for object detection purpose
(A, B, C, D)	coefficients of a plane equation
M_x	first moment of area in the x direction
M_y	first moment of area in the y direction
S_x	static moment in the x direction
S_y	static moment in the y direction
S_z	static moment in the z direction
S_t	total static moment
covar	covariance between the variables
\bar{x}	mean value of the vector x
\bar{y}	mean value of the vector y
CM	covariance matrix
λ_i	eigenvalues of a covariance matrix
Λ_i	eigenvectors of a covariance matrix
$N(p)$	neighbourhood of point p
ξ	ratio of a eigenvalue to the sum of all eigenvalue

Chapter 1

Introduction

1.1 Motivation

The discussion of global climate change and its possible consequences have taken centre stage over the last decade. Global climate change has triggered more erratic weather patterns by causing severe and unpredictable rainfall events in many parts of the world. The incidence of more frequent rainfall has led to the problem of increased flooding in urban areas as well as raised increased awareness of this problem. The process of urbanization in the form of continual infrastructure development transforms the natural vegetated catchment into concrete and asphalt sealing. Thus urbanization exerts a great impact on urban hydrology by increasing the surface runoff. It is a standard practice to design urban drainage systems based on historical rainfall data. As climate change is already having effects, conventional design methods of urban drainage systems that do not consider climate change scenario will prove inadequate to accommodate large volumes of water originating from intense rainfall and subsequent excessive surface runoff. A drainage system collects the stormwater and conveys it further downstream before it reaches a receiving body of water. In a built-up area, the surface runoff travels faster over impervious surfaces and quickly reaches the sewer system, posing the risk of an overflow from the underground pipe systems. When the peak flow rate exceeds the capacity of the pipe flow, the excess water is flushed back to the surface through manholes and

water inlets as well as it prevents surface runoff from entering the sewer systems, resulting in surface flooding. This phenomenon is known as urban flooding. At this point no water can enter into the pipe system and water travels down the street and spills over the neighbouring topography exposing settlements and properties to the risk of damage.

Modelling of urban flooding is important in order to reproduce the runoff behaviour and simulate the flood depth. The results of the simulation also provide clear understanding of the drainage system weakness. Thus, information acquired from the simulation results help the engineers and planners to take necessary steps for the possible renovations and improvements of the hydraulic capacity. A flood model generally consists of two modules: hydrologic (surface) module and hydraulic (sewer) module. The hydrologic module calculates the runoff from a given intensity of rainfall. The hydraulic module attempts to simulate the overland flow movements and determines the flood depth and flow velocity. However, the accuracy of the simulated results largely depends on the quality of the input data and full consideration of surface flow as well as underground pipe flow. The main inputs for a flood model featuring the 2D flow are topographic elevation data, runoff coefficients of different surface types and boundary conditions (Bishop et al. [16]). The topographic elevation data, also known as DEM/DSM is the most important input data to any urban flood model and the quality of the DEM directly influence the result of the model. A high-resolution DEM representing urban structure such as buildings and streets etc. and a detailed friction map of various urban surfaces can only simulate the realistic flow velocity and flood depth of a real-world urban flooding scenario.

1.2 Problem statement

The use of two-dimensional hydraulic modelling in rural floodplains has been well-documented in a number of studies (Neelz et al. [95]; Romanowicz and Bever [105]; Nicholas and Mitchell [96]; Bates et al. [15]). The last decade has seen a huge increase in the computational power of the desktop computers and the availability of topographic data at reasonable spatial resolution has caught the attention of river engineers/hydrologists, leading them to adopt a two-dimensional approach to flood

modelling. However, the enthusiasm for the widespread application of 2D models was limited to rural floodplains until the recent availability of very high resolution terrain data of complex urban scenes. With the introduction of a dual drainage approach (Djordjević et al. [35]), the necessity for a high-quality DEM was seriously addressed in order to model the urban flooding problem. Initially, the dual drainage approach was based on the 1D surface models which represented the detailed DEM of the streets and the neighbouring urban structures. With the emergence of software packages supporting 1D hydraulic models such as MOUSE/MIKE 11 [147], SOBEK [146] and EXTRAN [150], and their applicability for modeling the urban flooding problem, the simulated flood depth and flow velocity showed good correspondence with the field values, although they were not exactly the same. The inherent shortcomings of the 1D approach, such as the limited capacity to calculate flow velocity at the street cross-section and for the topography beyond the street network, still remain a challenge. The demand for more realistic overland flow modelling and consideration of extensive impacts of buildings make it essential to adapt the urban flooding problem to 2D hydraulic models.

While the recent advancements provided by the increased computational power have facilitated the setting-up of the 2D models, the requirement for a fine-resolution topographic data of a relatively large urban area and subsequent data processing still remain a problem for efficient implementation of 2D model approaches (Bishop et al. [16]). Apart from the requirements for a fine-resolution and large-scale database, a clear insight into and deep understanding of various urban structures and their potential impact on the water flow behaviour is vitally important for modelling the urban scene's complexity. With the availability of new-generation high resolution satellite imagery such as IKONOS and QUICKBIRD and the emergence of airborne laser altimetry (LiDAR), topographic elevation data and surface information at higher spatial resolution are becoming increasingly affordable. For quite a few years, some researchers have already been using high resolution topographic data, mainly LiDAR derived elevation data for modelling rural and urban floodplains (Bates et al. [15]; Neelz and Pender [94]. High resolution topographic data collection based on field surveys for the purpose of modelling urban flooding has also been reported in the literature (Bishop et al. [16]; Schmitt et al. [111]).

Although LiDAR technology has a clear advantage over traditional field surveys in terms of faster data collection, the processing of large volumes of LiDAR point data, often totalling millions of readings for a 1km by 1 km study area, poses a challenge to the generation of accurate DEM. Manual processing of this huge volume of data by a human operator is a tedious as well as a time-consuming task and requires repeated manual efforts for every new study area. The application of robust data processing techniques is necessary in order to extract features such as buildings, trees and streets from a large volume and highly unstructured LiDAR point cloud. Fortunately, researchers working in the field of photogrammetry and remote sensing have come up with a set of algorithms in order to segment and classify LiDAR data. The proposed algorithms are diverse in nature and targeted at specific applications. For example, the task of updating existing city building maps require a LiDAR filtering algorithm that detects only building objects. On the other hand, the purpose of generating a virtual city model requires a filtering algorithm that not only detects the building objects but also recognizes each planar surface of the roofs. However, there is potential scope for applying different LiDAR filtering/classifying techniques in order to detect and model urban structures such as buildings, streets, boundary walls, street kerbs etc. Unfortunately, the hydrologists, flood modellers and river engineers have either used manual processing of LiDAR data or utilized the already processed DEM provided by a third party (an exception is Mason et al. [88]).

Apart from generating LiDAR-derived DEM, the task of detecting different land cover types plays an important role in improving the overall accuracy of urban runoff model. Accurate extraction of urban land cover types using LiDAR data and aerial images provides not only useful information in terms of infiltration, evapotranspiration and surface runoff parameters and characteristics but also facilitates the calculation of surface roughness coefficients in terms of hydraulics. However, recent works related to urban flood modelling have not used any image classification technique to extract urban land cover types. Image classification approaches are techniques that produce classified maps of the land cover types of a study scene. Most of the traditional image classification routines work on a per-pixel basis adopting the maximum likelihood classification (MLC). Pixel-based classification is reported as

producing unacceptable results when the pixel size of the aerial image is too small, i.e. having finer resolution (< 10 cm to 2 m).

1.3 Research objectives

The main goal of this research is to generate a high resolution DSM capturing detailed urban surface characteristics using LiDAR data, aerial images and topographic maps. This research study focuses on the following specific objectives:

- To provide a suitable database for 2D surface flow modelling using dual drainage approach.
- To achieve higher degree of automation in terms of processing unstructured LiDAR data.
- To explore the suitability of using other datasets such as aerial images and topographic maps in order to improve the overall quality of urban drainage modelling and simulation.
- To use the integrated database in a simulation model for assessing the hydraulic capacity of the urban drainage systems.

1.4 Proposed approach

Surface flow due to urban flooding is a dynamic process and is heavily dominated by the complex urban terrain. A detailed description of the complex terrain requires detection of the topographic objects and different land cover types. The task of topographic feature detection can be viewed as a classification task of a built-up urban area. The goal of the classification task is to deliver a land use and land cover (LULC) map featuring clear object boundaries as well as topographic elevation data of a complex urban scene. Figure 1.4 shows the overall workflow of the proposed approach. The proposed approach is a stepwise classification technique for detecting objects (i.e., buildings and trees) and surfaces (pervious and impervious). The

proposed approach utilizes LiDAR point data as a primary data source while aerial images and topographic maps serve as ancillary data for feature extraction. The first step is to separate the LiDAR point data into ground and non-ground points by applying a suitable filtering algorithm. Both the ground and non-ground points are treated separately in order to implement subsequent feature extraction and surface detection techniques.

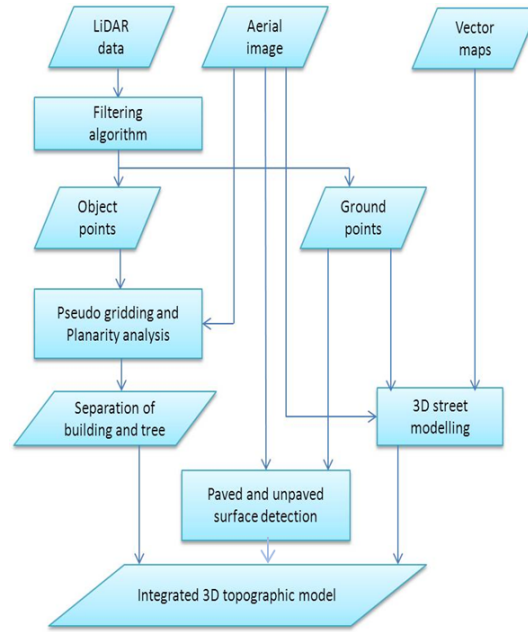


Figure 1.1: Overall workflow to generate high resolution digital surface models.

Thus, the overall approach is to introduce the concept of hierarchical object detection and classification techniques. The topographical features can be grouped into a number of objects such as buildings, trees, streets, micro objects (walls, fences) and the remaining ground points. In order to perform object classification, a user needs to handle only the non-ground points, which reduces the search domain and computation time. Should a user be interested in street extraction and modelling, the use of ground points only can be considered. The proposed approach is based on the idea of automatic deployment of data processing, the selection of a suitable algorithm and subsequent classification. The processing of various types of datasets such as unstructured LiDAR point data, aerial images and topographic maps and their integration in order to achieve the maximum benefit, robust algorithms per-

taining to point data and image processing are essential to produce an accurate classified topographic map. This study attempts to introduce efficient algorithms from the perspective of computer vision and image processing in order to address the task of generating high resolution urban DSM.

1.5 Organization of the dissertation

The dissertation is structured as follows:

Chapter 1 (this chapter) presents the motivation for this research work and explains the proposed approach. This chapter also contains the research objectives and the contribution of this research work.

Chapter 2 discusses the related work. It describes the state-of-the-art urban drainage modelling, LiDAR data filtering, objects classification street extraction and object-based image classification.

Chapter 3 contains information on the study areas, data types and materials used in this study.

Chapter 4 describes the implementation of a LiDAR filtering algorithm and its application to the two study areas.

Chapter 5 describes two classification algorithms for separating buildings and trees from non-ground LiDAR point data. The first algorithm uses LiDAR data and aerial images whereas the second algorithm uses only LiDAR data.

Chapter 6 describes street extraction and subsequent 3D modelling framework using LiDAR data, topographic maps and aerial images.

Chapter 7 presents object-based image analysis (OBIA) techniques in order to detect different surface types using aerial images and LiDAR intensity data.

Chapter 8 presents the resulting data model by integrating different topographic data layers. This chapter also describes the application of this resulting data model to a standard urban drainage simulation model.

Chapter 9 presents the summary of the entire research work. Some future recommendations are made for possible improvement and continuation of this research.

Chapter 2

Literature review

The occurrence of urban flooding is the result of functional deficiency of the urban drainage systems. The main components of an urban drainage system are the underground pipe networks and the surface drainage paths as well as retention ponds. The performance of each individual component determines the overall hydraulic capacity of the urban drainage system. Thus, one of the main objectives of modelling an urban drainage system is to understand the behaviour of the system and its response to a specified rainfall event (Akan [3]). While the representation of sewer networks is *a priori* in a flood model, modelling of surface drainage systems is much more complex as it depends on the topography of the urban scene. The necessity of having high-resolution spatial data to describe the hydraulic and hydrologic properties of a complex urban scene has always been a primary demand for modelling of urban flooding using a suitable flood model.

The advancement in airborne laser scanning (LiDAR) technology has emerged as an alternative to the field-based survey techniques and have enabled the faster collection of topographic data. The generation of high spatial resolution LiDAR-derived DSM featuring detailed surface drainage characteristics can serve as input data to the existing flood simulation models. This high resolution DSM will surely increase the surface drainage capacity of an urban drainage system and will thereby provide a better understanding of the behavior of the systems and facilitate realistic prediction of the flood inundations. This chapter presents state of the art urban drainage

models and techniques related to urban surface information extraction using LiDAR and other ancillary data such as topographic maps and aerial images. The suitable LiDAR processing algorithms/techniques are chosen in order to address the problem of detailed surface drainage system generation.

2.1 Urban drainage models

Conventionally, the surface runoff or surface flow is simulated by using hydrological approaches where the runoff is computed from the rainfall using a unit hydrograph. Traditional sewer models attempt to simulate underground drainage networks to the point where water is inside the pipe network and there is no overflow of water through manholes (Dey and Kamioka [33]). Without considering this sewer overflow situation, it is difficult to simulate the realistic flooding scenario. This type of model mainly attempts to solve Saint-Venant 1D flow equations and simulate the flow behaviour within a drainage pipe network (Hénonin et al. [61]). Software packages such as MOUSE (DHI [149]), INFOWORKS-CS (Wallingford Software Ltd. [154]), and SWMM (US EPA [153]) are examples of 1D drainage network models. These models are not able to simulate the water movement on the surface when the water escapes from the sewer system and reaches the street surfaces (Chen et al. [23]). Urban drainage systems have two components: 1) the underground sewer networks; 2) the surface drainage structures such as flow pathways and retention ponds. The integration of both drainage components is important for correctly simulating the bi-directional flow phenomena at manhole locations where subsurface (sewer) and surface flow come into contact to exchange water. Thus, this integrated model can make actual predictions of the extent of urban flooding. The concept of this integrated model in urban drainage systems was first introduced in the nineties by Djordjević et al. [36]. This concept is also known as the dual drainage model (Djordjević et al. [35]).

In the dual drainage concept, the surface flow paths and retention ponds and basins are considered a major drainage system for routing surface flow while underground pipe networks, manholes and inlets are considered a minor drainage system to carry off subsurface flow (Chen et al. [23]). Dual drainage models are the implementation

of 1D-1D model which means that both the drainage components have 1D hydraulic models and the bi-directional flow exchange between surface networks and underground pipes occurs through the manholes and inlets (Mark et al. [85], Schmitt et al. [112]). However, this type of 1D modelling approach has inherent limitations in terms of calculating surface flow at street cross-sections or on the surface where the flow pathways are not predefined (Chen et al. [27]). Some researchers have suggested implementing a 2D hydraulic model for overland flow simulation. In Carr and Smith [20], a linking approach between 2D overland flow models and 1D pipe flow models is described using high resolution (2m) spatial grid data. Their approach explores many hidden flow paths on the surfaces and identifies the flood-risk areas in a variety of urban catchments in Australia and New Zealand. Chen et al. [24] present an inundation model by integrating a 1D dynamic channel flow model and a 2D non-inertia overland flow model in order to evaluate the hydraulic behavior of urban catchments with different characteristics.

There are a number of models, both commercial and open source, available to simulate sub-surface and surface drainage networks. The Storm Water Management Model (SWMM) was developed by the U.S. Environmental Protection Agency (Rossman et al. [106]) and is believed to be the most widely-used software for design and analysis of drainage systems. SWMM is a dynamic rainfall-runoff simulation model and is used for hydraulic performance assessment and water quality modelling too (Ha et al. [53]). The runoff component of SWMM collects the precipitation and calculates the runoff whereas the routing component of SWMM conveys the runoff through channels and pipes (US EPA [153]). Chen et al. [23] describe the SWMM model as an open source and its hydraulic engine is widely used in commercial software packages such as PC SWMM (Computational Hydraulics Int. [151]), XP SWMM (XP Software Inc. [152]) and MIKE SWMM (DHI Software 2002 [149]). However, there are other software packages that do not use SWMM; rather, they have their own hydraulic solvers such as MOUSE (DHI Software 2003 [149]) and Infoworks-CS (Wallingford Software Ltd. 2006 [154]). Apart from the above-mentioned software, there are other software packages that are the research products of certain research groups working at universities or research institutes. SIPSON

(Djordjević et al. [36]), RiSurSIM (Schmitt et al. [112]) and UIM ((Chen et al. [24]) are some examples, to mention but a few.

Djordjević et al. [36] use the SIPSON model to describe the interaction between pipe flow and overland flow. They use 62 street channels, cross-sections at nine points and 26 points where manholes link between sewer and surface flow to represent a catchment area of 15 ha. The SIPSON model works on the assumption that the surface flow is 1D and the simulation results show good agreement with the reality as long as the sewer system is not overloaded. However, the simulation results show large discrepancies when the sewer system is surcharged. They do not properly delineate the surface storage volume where water can stay longer. The problem mentioned hints at the basic necessity of detailed surface model generation to feed into the SIPSON model. Consideration of street channels alone is not a real-world representation of the catchment and there are other types of land cover in a built-up urban area that have a potential impact on runoff, surface routing and flow velocity. Schmitt et al. [112] use the RisUrSim model to make an assessment of urban flooding by dual drainage simulation. Very high-resolution surface data of two streets in a residential area are chosen as input data to the RisUrSim model. The data collection procedure is, however, manual and they could not validate the model against field data as there were no flooding events during that time.

Ettrich [42] uses airborne LiDAR-derived DSM for a relatively large ($500\text{m} \times 500\text{m}$) study area as input surface data to the RisUrSim model. He describes the importance of assigning hydrologic properties characterization to the catchment area such as degrees of impermeability and permeability. However, he does not perform any surface characterization and assumes that runoff occurs only on the street and that water is fed into the street from the surrounding catchment area in a unidirectional way. Ettrich [43] presents an updated version of his previous work by considering the surface property of the catchment area in addition to elevation data. Surface properties such as friction loss, depression loss and infiltration loss are assigned to each type of surface. Another aspect of this work includes detailed modelling of streets, street kerbs, sidewalks and boundary walls next to streets. The building footprints on the catchment area are kept as holes (no area) on the assumption that flood water cannot replace building positions. Modelling of street kerbs and bound-

ary walls is performed manually and surface classification is dependent on visual interpretation from aerial photos.

Chen et al. [23] present an integrated numerical model to describe overland flow by UIM model (Chen et al. [24]) and pipe flow by SIPSON model. They use LiDAR-derived DSM (digital surface model) for the surface model. The spatial resolution of the grid is coarse (2m) and they do not make any surface classification. Bishop et al. [16] use a detailed 2D hydraulic modelling in three urban developments. They investigate the typical friction parameters of residential properties in predicting flood inundation using MIKE 21 environment. They make a very detailed field survey in order to generate 2m resolution DEM. Vojinovic et al. [125] study the effects of DEM resolution on urban flooding. They use two types of DEM: 1) a DEM where buildings and streets are kept as hollow objects; 2) a DEM where streets are lowered intentionally relative to the surrounding topographic height. They apply the friction coefficients as a general rule of thumb. Hunter et al. [69] present a study on benchmark testing of 2D hydraulic models for urban flooding using high-resolution DEM and six 2D hydraulic models. However, they use 2m resolution DEM provided by a third party (OS Mastermap) and the insertions of street kerbs are manually edited.

In essence, a number of flood simulation models are available, both commercial and open source. The fully integrated 1D-2D approaches are becoming popular for modelling urban flooding. The requirement for high-resolution surface data to describe complex urban surfaces is still an ongoing research topic. The emergence of LiDAR technology has met the demand for high-resolution spatial topographic information. But the efficient processing of large volumes of unstructured point data acquired by LiDAR sensor and subsequent automatic urban feature detection remains a challenge for the flood modellers. Very recent studies (Vojinovic et al. [125]; Hunter et al. [69]) still rely on a significant amount of human interaction in producing a DEM before feeding it into a 2D hydraulic model. A land cover map of an urban scene deriving from a suitable image classification technique is a potential source for acquiring runoff coefficients of different types of urban surface. Determination of runoff coefficients (i.e. friction parameters) based on advanced image classification has not been fully employed within the context of urban flood

modelling. Although there exists a number of detailed urban drainage simulation models, still there is a high need for a high resolution spatial database representing urban surface characteristics.

2.2 LiDAR data to generate high resolution DSM

This section briefly presents the technical aspects and operating principles of the LiDAR (Light Detection and Ranging) system. LiDAR is an active remote sensing technology meaning it is capable of operating independently of sunlight conditions. In recent years, LiDAR has emerged as a surveying tool, especially for the acquisition of terrain data. The LiDAR system, when mounted on an aircraft, can measure the topographic elevation data by sending a laser pulse to target the ground. At the same time, the LiDAR system records the geographic coordinates of the targeted ground points and delivers them as discrete point clouds. The history of LiDAR technology can be traced back over 40 years. In the 1970s the National Aeronautics and Space Administration (NASA) developed the LiDAR technology, and its commercial application started in the mid-1990s (Bartels and Wei [13]; Pfeifer and Briese [98]). Figure 2.1 illustrates a typical airborne LiDAR system with its embedded components: a laser scanner, a GPS (Global Positioning System) and an INS (Inertial Navigation System).

LiDAR technology also ensures a high level of accuracy while collecting topographic elevation data. LiDAR technology is reported as having a vertical accuracy of 15cm and a horizontal accuracy of 50cm (Neelz and Pender [94]). However, the vertical accuracy can be improved to 10cm with a low (i.e., 400m) flying height (Hu [68]). The horizontal inaccuracy can be fixed up to a desired level by applying image co-registration techniques. At present, there are many commercial LiDAR systems available on the market providing high-density and high-accuracy topographic elevation data (Baltsavias [12]; Hu [68]). The typical point densities of LiDAR sensors vary from 1 point in 2-4 square meters to 1-8 points per square meter. Besides elevation information, LiDAR data contain rich information about different surface types in a complex urban scene, such as bare earth, buildings, streets and parking lots. LiDAR-derived height information is an important attribute for differentiating ter-

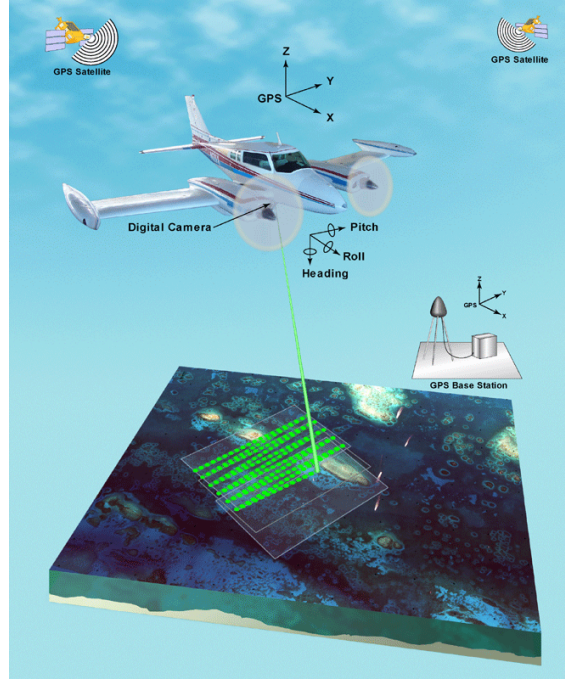


Figure 2.1: A typical airborne LiDAR system mounted on the aircraft with its embedded components (www.fs.fed.us).

rain and non-terrain points, while LiDAR intensity data can provide information on various surface types. The emergence of LiDAR technology and its ability to acquire high-density topographic data along with its cost-effectiveness have made it a more popular choice than field survey and conventional photogrammetry-based terrain modelling (Liu [82]). The accurate and efficient generation of DTM and DEM can be greatly facilitated by using LiDAR data (Forlani and Nardinocchi [47]). There has been a remarkable increase in the use of LiDAR data for DTM and DEM generation over the last decade as more reliable and accurate LiDAR systems have been developed during this time (Sithole and Vosselman [119]).

In traditional photogrammetry, there is a branch known as stereoscopy or stereophotogrammetry which deals with 3D observation of a scene with the help of two or more photographic images of the same scene viewed from different observation points. However, in a dense urban scene with tall buildings creating occlusions and in forested areas with a thick canopy layer, traditional stereoscopic techniques cannot perform well due to the lack of viewing clarity from different positions in

a particular scene. Krauss and Pfeifer [79] demonstrate that the accuracy of the LiDAR-derived DEMs in forested areas is equivalent to that of photogrammetry-derived DEMs in open areas (Liu [82]). Knabenschuh and Petzold [76] describe the suitability of using Laser scanning in surveying and mapping agencies in Germany. Since 1994, in the field of modelling rural and urban river flooding, there has been increased use of LiDAR-derived high spatial resolution DTMs (Neelz and Pender [94]). Mark and Bates [86] use LiDAR-derived topographic representation of the River Stour floodplain. They predict realistic discharge at the downstream using a 2D hydraulic finite element scheme and LiDAR-derived accurate DEM. Bates et al. [15] investigate the optimal use of high-resolution topographic data in river flood inundation models. They suggest the extraction of linear features from LiDAR data. Neelz and Pender [94] experimentally show that artificial roughness added to DEMs can significantly slow the flow velocity, thereby affect the manning's 'n' value. Objects on the DEMs, such as buildings, constructed river banks, streets and dykes, play an important role in flow dynamics and flood propagation, and those objects must be accounted for in any flood model set-up with the help of LiDAR-derived DEM and DTM (Vyas [129]).

2.3 Filtering algorithms of LiDAR data

Filtering is the process of separating LiDAR data into ground (terrain) and non-ground (objects) points. Thus, filtering serves the purpose of generating a DTM by removing the objects on top of it as well as acting as a pre-classification step towards identification of different objects (buildings, trees etc). Figure 2.2(a) presents the schematic diagram of an urban topography and LiDAR points hitting the ground as well as the objects. Figure 2.2(b) illustrates the separation of ground (red) and non-ground (black) points after filtering process.

Many algorithms have been designed in the last decade to filter LiDAR data into ground and non-ground points (Vosselman [128]; Sithole [118]; Shan and Sam-path [115]). Vosselman [128] proposes a 'slope-based' method from a morphological image-processing context and the use of an erosion operator. He assumes that the

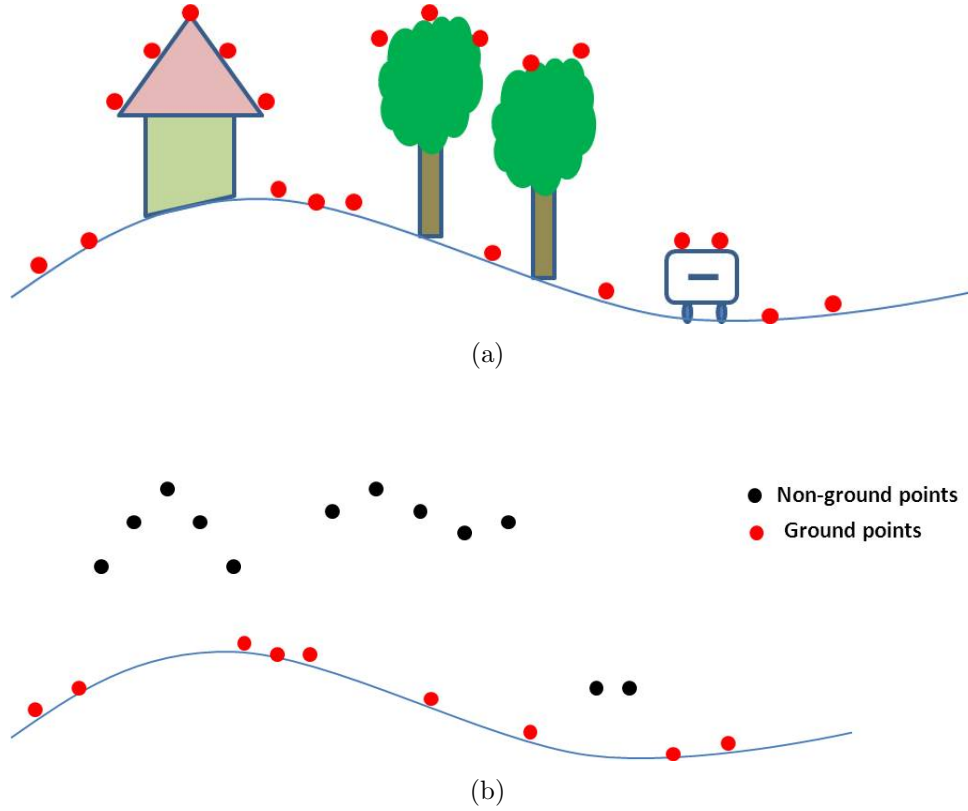


Figure 2.2: Filtering of LiDAR point data.

performance of the filter deteriorates with the decreasing number of LiDAR points. Sithole [118] modifies the ‘slope-based’ filter by incorporating a threshold value that takes into account both terrain and slope information. Shan and Sampath [115] address the problem of separating LiDAR point data into ground and non-ground points as a labelling process. They introduce the concept of one-dimensional labelling followed by a linear regression technique. Most of the aforementioned algorithms work on the LiDAR grid data or LiDAR-derived range image. Few of them work on the raw LiDAR point clouds. There are advantages and disadvantages of performing filtering operations on both types of LiDAR data (i.e. raw and grid data). Raw LiDAR point clouds are supplied as irregularly distributed points capturing the three-dimensional information of the topography. When the raw point cloud is transformed into image data or grid data, the original surface information is interpolated and to some extent altered. The conversion of raw point data into

image or grid data is known as ‘rasterization’. Rasterization creates “raster images” which offer the ability to exploit the standard image-processing tools (Filin and Pfeifer [45]). The rasterization process also involves some disadvantages in terms of neighbourhood definition and retrieval of original data. Also, during the process of rasterization, the original x, y coordinates of LiDAR data are converted into matrix indices containing elevation data for each grid. The matrix or raster format is actually a 2.5D model, which is the representation of original 3D LiDAR data. Therefore, rasterization involves interpolation resulting in the masking of the original data (Filin and Pfeifer [45]).

There are some filtering algorithms designed for raw LiDAR point data (Bartels and Wei [13] ; Roggero [104]; Bartels and Wei [14]). Bartels and Wei [13] propose an algorithm called ‘skewness balancing’ in order to separate ground and object points. The assumption behind their algorithm is that terrain points tend to exhibit normal distribution while object points cause disturbance in the normal distribution pattern. So removal of those object points in an iterative manner in order to restore the normal distribution of the terrain points is the main goal of their algorithm. Bartels and Wei [14] propose an extended version of the ‘skewness balancing’ algorithm in order to make this algorithm perform better in a terrain with steep slopes. Roggero [104] develops the region-growing algorithm, which is based on a principal component analysis of noisy raw LiDAR point data. The principle behind his region-growing technique is the aggregation of neighbourhood points.

Automatic separation of ground and non-ground points from LiDAR data has proved to be a difficult task when dealing with large areas of varied terrain characteristics (Liu [82]). Scientists working with LiDAR data have not yet been able to come up with a universal error-free solution that can ensure accurate object extraction. In the last ten years, many filtering algorithms have been developed for automatic separation of ground and non-ground points from LiDAR point clouds (Nardinocchi et al. [92]; Sithole and Vosselman [119]; Filin and Pfeifer [46]; Kobler et al. [77]). Forlani and Nardinocchi [47] put all the existing filtering algorithms into three categories. The first category of algorithms searches for the minimum elevation point in a neighbourhood scale and assigns it as a ground point by using morphological filters with appropriate structuring elements (Vosselman [128]; Sithole [118]).

The second group of algorithms attempts to fit an interpolating surface to the data and calculate the distance of each individual point from this surface. Points having a measured distance bigger than a threshold are labelled as non-ground points (Krauss and Pfeifer [79]; Axelsson [10]; Brovelli et al. [18]). The following Figure 2.3 illustrates the concept of surface based filtering techniques.

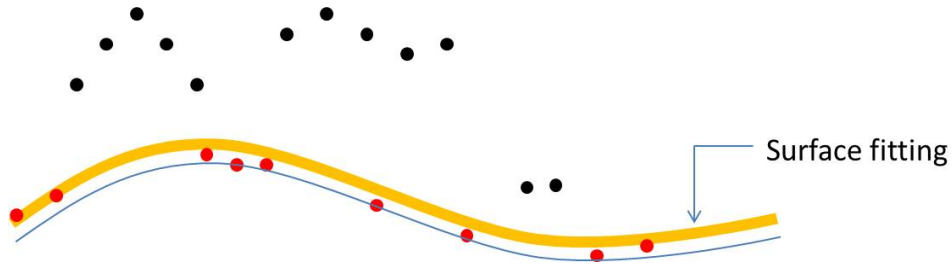


Figure 2.3: Filtering technique by surface fitting approach.

The third category of algorithms performs segmentation as a pre-step to classification. When the segmentation is finished, classification of ground and non-ground points is performed using clustering techniques (Roggero [104]; Nardinocchi et al. [92]). Although many filtering algorithms have been proposed in recent years, no single filtering algorithm can perform equally well in a variety of landscapes. The reasons for these limitations are mostly related to the degree of complexity of terrains, and assumptions or threshold values to separate features do not match the reality (Forlani and Nardinocchi [47]). The sensitivity of the LiDAR filtering algorithm may affect the performance of the flood simulation model if it underestimates the object definition. Objects such as boundary walls, fences and other artificial items may be erroneously removed from DTM if the height and slope threshold value of the filtering algorithm is set too low, as these objects guide the overland flow (Neelz and Pender [94]). Abdullah et al. [1] describe the DTM generation process by considering the idea of micro objects detection. They describe objects such as ramps, dividers and boundary walls as micro objects. They tested existing filtering algorithms on their cases and chose the best one depending on the RMSE error analysis.

In essence, the field of LiDAR filtering has been enriched by the contribution of many researchers, most of whom have backgrounds in geosciences and computer

sciences. Generation of a detailed DEM by applying a suitable filtering algorithm is a crucial issue in retaining the urban micro structures on the DEM. Further insight and careful parameterisation are necessary for an accurate representation of a DEM adaptive to urban flood modelling. In this study a surface-based filtering algorithm will be discussed in Chapter 4. The concept of fitting a parametric plane equation is implemented here for the separation of ground and non-ground points while retaining the micro-objects on the ground.

2.4 The identification of objects (buildings and trees)

This section presents the State of the art of object classification i.e. buildings and trees. In recent years researchers have proposed a number of methods to detect buildings and trees using different sensors' data. All those methods vary in approach, degree of automation and use of data types. This section will restrict itself to describing the literature related to LiDAR and other ancillary data in detecting buildings and trees. Previous work on LiDAR classification can be categorized as follows: (i) classification of LiDAR data into terrain and non-terrain points; and (ii) classification of non-terrain points into features such as trees and buildings (Charaniya et al. [22]). The first type of classification is known as filtering algorithm and is presented in Section 2.3.

The automatic detection of buildings and trees using only LiDAR data has been well documented in various studies (Roggero [103]; Carlberg et al. [19]; Chen and Zakhor [25]). Roggero [103] fits a local plane for separating buildings and trees from non-ground LiDAR point data. A non-ground point belongs to a building if there exists a local plane and the central point fits the plane. Carlberg et al. [19] present the classification of urban landscape using airborne LiDAR data and employing 3D shape analysis technique. They apply a region-growing technique for identifying 'planar' and 'scatter' regions. They consider the 'scatter' regions as trees and planar regions as ground/buildings. They further separate the buildings from ground using local height texture. Chen and Zakhor [25] convert LiDAR point data

into depth image and perform segmentation followed by classification techniques. They compute height variation, edge density and contour non-linearity in order to classify buildings and trees.

The aforementioned works are examples of a segmentation-based classification approach. Some researchers have attempted to perform per-pixel classification (Lodha et al. [83]; Charaniya et al. [22]). Lodha et al. [83] present a multiclass classification approach using scattered LiDAR height data and applying a machine learning algorithm called AdaBoost. They identify five attributes, namely height, height variation, normal variation, LiDAR return intensity and image intensity, in order to produce training data for carrying out supervised classification. They manually label 25-30% of the entire dataset. Charaniya et al. [22] present a similar multiclass classification approach using a parametric supervised classifier. They use a Gaussian mixture model for training data generation which covers 30% of the entire dataset. Thus, both the approaches proposed by Charaniya et al. [22] and Lodha et al. [83] require significant effort to train the dataset.

Some research in the direction of multiclass classification with a higher degree of automation has also been carried out (Axelsson [10]; Maas [84]; Filin [44]). Axelsson [10] separates the ground surface from LiDAR point data by applying Minimum Description Length (MDL) models and constrained spline functions. Later he classifies buildings and trees from non-ground points using a cost function based on the second derivatives of the height function. However, he does not present any classification accuracy of the produced result. Maas [84] describes the potential use of height data and height texture measurement in LiDAR data segmentation and classification. He segments the LiDAR point data into ground and non-ground points using height data. In the next step, he applies height texture measurement to separate buildings and trees from non-ground points. Filin [44] describes a clustering technique for extracting various surface patterns from airborne LiDAR data. Later he applies height and slope threshold to each surface patch to distinguish four surface categories: 1) forest, 2) low vegetation, 3) smooth topography and 4) planar surface. Alharthy and Bethel [6] propose a two-stage classification algorithm to distinguish between buildings and trees using first and last pulse LiDAR return. First, they calculate the difference between first and last pulse and then apply local

statistical inference over a small window. Oude Elberink and Mass [39] investigate the potential of the anisotropic height texture in the LiDAR range image for automatic detection of trees. Demir and Baltsavias [32] focus on the accurate detection of buildings using LiDAR data and multispectral aerial images. They apply a series of classification methods in two test areas. Their methods include: 1) comparison of DSM/DTM in combination with vegetation index analysis; 2) supervised classification and 3) analysis of raw LiDAR DSM.

There has been some research devoted to detecting buildings and trees by combining aerial image and LiDAR data. While some researchers use colour infrared (CIR) images with LiDAR data (Haala and Brenner [54]); Vögtle and Steinle [124]), others preferred, green and blue (RGB) images (Matikainen et al. [89]); Salah et al. [109]; Demir and Baltsavias [32]). Haala and Brenner [54] describe the technique of combining LiDAR-derived DSM as an additional channel in combination with three CIR channels. They use ISODATA clustering technique to classify different objects. Vögtle and Steinle [124] present a method of stepwise elimination of objects that are not buildings. They calculate the Normalized Difference Vegetation Index (NDVI) followed by the masking out of vegetated areas. Their method exploits both the spectral as well as spatial information such as shape and size parameters of an object. Matikainen et al. [89] present a classification tree-based approach to detecting buildings. In their method, they utilize different combinations of 44 attributes deriving from first pulse DSM, last pulse DSM and aerial image. Their proposed method requires a significant number of training segments for the construction of a classification tree. Salah et al. [109] describe a multiclass classification method using Self-Organizing Map(SOM). They calculate 22 uncorrelated feature attributes from aerial image, LiDAR intensity image and LiDAR DSM.

In recent years there has been a tendency to use decision tree classifiers in order to classify remotely sensed data. In Friedl and Brodley [49], the suitability of decision tree classification algorithms for classifying remotely sensed images has been tested. They apply three different types of classification algorithms- univariate decision tree, multivariate decision tree and hybrid decision tree to classify remotely sensed data. Their methods outperform the maximum likelihood classification approach. The main strength of a decision tree classifier is its ability to split up a complex deci-

sion systems into a number of simpler decisions by virtue of its explicit classification structure (Safavian and Landgrebe [108]). Lawrence et al. [80] introduce the concept of stochastic gradient boosting (SGB) in order to enhance the capability of traditional classification tree analysis (CTA). They make a comparison of CTA and SGB approaches using three remotely sensed data including an IKONOS image. They conclude that the results of the SGB approach show higher accuracy than the CTA approach. The use of a decision tree is particularly interesting when it comes to the use of multisource datasets when different types of possible input attributes are used (Matikainen et al. [89]).

Pfeifer et al. [99] present an overview of the algorithms devoted to the detection of buildings using airborne LiDAR data. They perform the evaluation of two algorithms: 1) building detection based on hydrological raster tools and 2) building detection by Dempster-Schafer fusion of LiDAR data and multispectral images. They conclude that on pixel level hydrological tool approach performs better than Dempster-Schafer approach. However, their work is not fully automatic. Zhang et al. [138] present an automatic framework of building footprint reconstruction. Their proposed framework involves a series of algorithms. In the first step, they apply filtering technique in order to separate ground and non-ground points. In the second step, a segmentation algorithm followed by a plane-fitting technique is implemented to separate the buildings from the non-ground points. In the final stage they connect the boundary points of the raw building points.

The previous works on the classification of buildings and trees use a variety of data sources. Some researchers have used only LiDAR height data while the others opt for the combination of different data sources. Various combinations of data sources for the task of classifying buildings and trees can be assembled as follows:

- The use of LiDAR height data only.
- The use of LiDAR height and intensity data.
- The use of LiDAR height data and aerial image.
- The use of LiDAR height, intensity and aerial image.
- The use of LiDAR height data and topographic maps.

In this study, two different approaches for classifying buildings and trees using different combination of data sources will be presented in Chapter 5. Both approaches are structured as an unsupervised region growing clustering technique which is followed by a knowledge-based classifier. The first approach uses LiDAR height and aerial image information whereas the second approach uses the LiDAR height data only.

2.5 Street/road detection

Streets are the primary preferential paths for the propagation of flood water in the event of urban flooding. Proper representation of street networks in the urban DSM and their geometric characterization are important for better quality of the simulation results. This section presents the literature works devoted to the detection of streets using remotely sensed images, LiDAR and other ancillary data.

Automatic street/road extraction from aerial and satellite imagery has been a research topic for more than twenty years. The resolution of optical images has a direct influence on the proposed approaches to automated street extraction. For example, an image with a spatial resolution of about 1 metre or more would cause a given street network to appear as a linear feature with bright or dark radiance (Rottensteiner [107]). It has been standard practice to treat the roads/streets as linear features (Hu [68]). A line-fitting or curve-fitting algorithm is an appropriate choice to extract a street network in the presence of coarse resolution imagery (Wiedemann and Ebner [132]; Dial et al. [34]; Gecen and Sarp [51]; Heipke et al. [60]). Wiedemann and Ebner [132] present the idea of link generation between the extracted road components. Their methods result in better reconstruction of road connectivity and network topology. Gecen and Sarp [51] use four satellites imagery and apply a high pass filtering technique to extract streets automatically. They also compare the effect of image resolutions on the degree of automation. Heipke et al. [60] describe three techniques to extract streets in an automatic way from both high and low resolution imagery. They apply 1) a line-fitting algorithm, 2) a combination of line-fitting and high resolution grouping and 3) a combination of line-fitting algorithm and snake theory. With the emergence of very high-resolution

aerial and satellite images, streets are being treated as having distinct geometric patterns. Besides, a street surface is believed to exhibit spectral homogeneity which might be disturbed by the presence of occlusions such as cars or trees (Hinz and Baumgartner [63] ; Zhang [136]). Hinz and Baumgartner [63] exploit contextual information in high-resolution images. They use multiple views of urban scenes in order to deal with occlusions. Zhang [136] applies a knowledge-based image analysis technique for constructing a 3D street network. He uses colour images and spatial database for this purpose.

In recent years, many approaches and algorithms have been proposed in the literature. Mena [90] presents the state of the art of street/road extraction algorithms from aerial and satellite imagery. The author includes almost 250 references which cover a variety of topics such as street extraction and modelling, street-tracking algorithms and morphological and dynamic approaches related to automatic street extraction. Mena [90] also classifies the street extraction algorithms based on: 1) present objective, 2) extraction technique applied, 3) types of sensor utilized and 4) mid- and high-level methods. Most of the approaches are different in nature because of the use of different objectives, data sources, various assumptions about street models and their degree of automation. Some methods work without using much prior knowledge and they are thereby vulnerable to disturbances such as shadows and other occlusions (Park and Saleh [97]; Hu [68]).

Price [100] takes an urban scene as a case-study and explains that street extraction using only spectral information is not sufficient when dealing with complex urban areas. For example, the similarity in spectral response from objects such as buildings and streets always produce misclassification. The situation worsens when overhanging trees, roofs and tall walls cast a shadow on the street, thus making it difficult for any kind of algorithm to work (Hu [68]). Other sources of data, such as DTM/DSM and existing GIS maps, can be used to improve the quality of the extracted street network in an urban scene.

Two types of algorithms have been proposed in recent years, namely automatic and semi-automatic. The semi-automatic system implies that the algorithm needs user-defined input or seed points. The first stage of a semi-automatic system is to input seed points interactively; the next stage is street centerline extraction by template

matching (Airault et al. [2]; Hu and Tao [67]; Ameri et al. [7]). Airault et al. [2] present two different techniques in order to improve the semi-automatic street extraction process from digital image. They incorporate the idea of fully automatic initialization by a pre-computed street network graph. Hu and Tao [67] propose a method for extracting the street centerline from high-resolution imagery using a hierarchical grouping approach. Their method is computationally less expensive as they select the street segments gradually. Ameri et al. [7] describe a semi-automatic street extraction approach where they combine several techniques such as spectral clustering, morphological filtering and the use of graph theory. They use multispectral and pan-sharpened IKONOS images in their study.

Easa et al. [38] propose an automatic street extraction algorithm using IKONOS image with 1m spatial resolution considering two types of horizontal curves. Their proposed street extraction algorithm is designed to detect two types of curves: circular curve and reverse circular curve. The automatic extraction system avoids the necessity of any user-defined seed points and detects street/road candidate pixels in the image by edge detection followed by the line-fitting Hough transform algorithm. Figure 2.4 illustrates the detection of simple curve. In Wang and Trinder [131], an automatic street extraction algorithm is proposed using low-resolution images. They assume streets as linear features and apply a morphological operator to extract the street pixels. Later they apply split-and-merge algorithm in order to smooth the extracted street lines.

There are other approaches that combine aerial images and LiDAR data to produce 3D street networks in an automatic way (Hu et al. [66]; Zhu et al. [140]). Zhu et al. [140] present a fully automatic street extraction algorithm by combining aerial photos and LiDAR data. They introduce the concept of associated road line (ARL) and real road line (RRL) and the gaps of RRL are compensated by the corresponding ARL. A great deal of existing works focus on the use of 2D images. This may be useful as long as the intention is to produce 2D cadastral maps or any other 2D visual interpretation. But height and slope are important criteria of a street segment or a whole street network in urban flooding simulation. Inherent and contextual information on the street network can be exploited by using elevation data. When the existing algorithms based on 2D image processing techniques show limitations

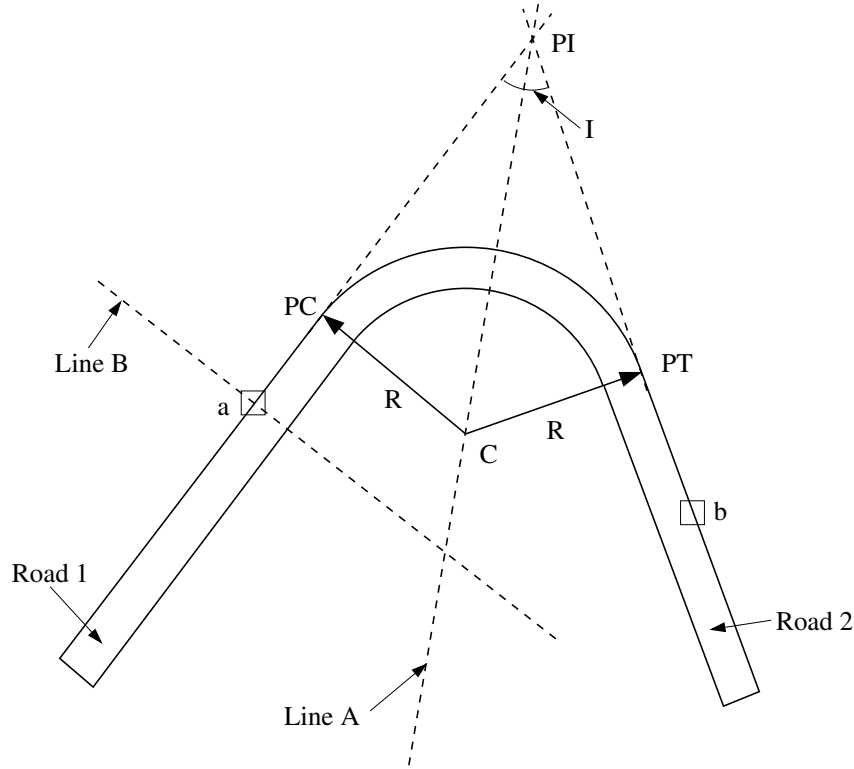


Figure 2.4: Detection of simple horizontal curve (Easa et al. [38]).

or perform poorly because of the presence of shadows/occlusions, the use of elevation data as DSM derived from LiDAR technology can provide information on the shadow/occluded regions.

Some automatic methods extract the street network only by exploiting LiDAR data (Clode et al. [29]). Sometimes, automatic methods can also use existing GIS databases as ancillary information to guide the street extraction procedure accurately and improve the accuracy and reliability (Zhang et al. [137]). Zhang et al. [137] use elevation data as additional information along with colour aerial images for improving the result of street classification of the regions that were under shadow. Their developed framework takes into consideration contextual information as well as knowledge-based decision rules. Zhang [139] photogrammetrically reconstructs and updates 3D street networks by combining GIS data and stereo aerial photo (Chen and Lo [26]). Chen and Lo [26] propose a street modelling approach divided into two parts: 2D street networking and surface modelling. The street network-

ing stage is implemented by establishing street centrelines from sides of the street polygons. In the surface modeling stage, airborne LiDAR data are extracted using a local neighborhood definition. The data combination techniques using LiDAR and topographic maps have been described in the literature to produce 3D street models. Hatger and Brenner [59] combine GIS map and LiDAR-derived DSM to compute street centrelines by employing a region-growing technique and computing geometric parameters.

Kada et al. [73] use GIS data to detect the street centreline first and then constructed the street surface from LiDAR-derived DEM by using a least square adjustment technique. Thus they produce a 3D street network with clearly defined boundaries. Vosselman [126] integrate LiDAR data and GIS maps to reconstruct single-layer street models. In this model, street polygons are manually edited and street candidate points obtained from LiDAR data inside street polygons are extracted. Later, the triangular irregular network (TIN) is generated to construct the street surfaces. Oude Elberink and Vosselman [40] concentrate on the construction of multi-layer street networks. They combine LiDAR data and GIS maps for this purpose. They extract street candidate points with the help of GIS polygon maps and determined different level of street networks from LiDAR elevation information. Oude Elberink and Vosselman [41] present an extension of their previous work by incorporating a full degree of automation and consideration of constraints for modelling topological properties.

The recent research trend has shown that fusion of LiDAR data and topographic maps (GIS maps) is the most effective way of constructing realistic street models. There are algorithms and techniques available to extract street/road networks from LiDAR data alone or with the help of other ancillary data. But there is hardly any work describing the automatic extraction of street network from LiDAR data and applying it within the context of urban flooding simulation. Moreover, detailed street modelling, such as street models with distinct sidewalks, kerbs and traffic lane elements, has not been described in recent works in an automatic fashion.

2.6 Impervious (paved) and pervious (unpaved) surface detection

Urban areas are usually covered by an overwhelming amount of concrete jungles (e.g. buildings, bridges) and paved surfaces (e.g. streets, parking lots, tennis courts). However, the presence of unpaved surfaces (e.g. grass and bare soil) is also noticeable if not as pervasive as paved surfaces. Paved surfaces can be impervious, partially pervious and pervious as shown in Figure 2.5(a), (b) and (c) respectively. In this study the term ‘pervious surface’ refers to both the grassland and bare soil while the term ‘impervious surface’ includes all types of paved surfaces. The reason behind this simplification is linked to the fact that both the investigated study areas: the Alcatraz and the Casimirring do not present variety of paved surfaces except the fully impervious paved surfaces. At the same time this study does not overlook the importance of differentiating among the subclasses of paved and unpaved surfaces. A subset of image containing bare soil and grassland surfaces is attempted to classify in Chapter 7 as an additional investigation.

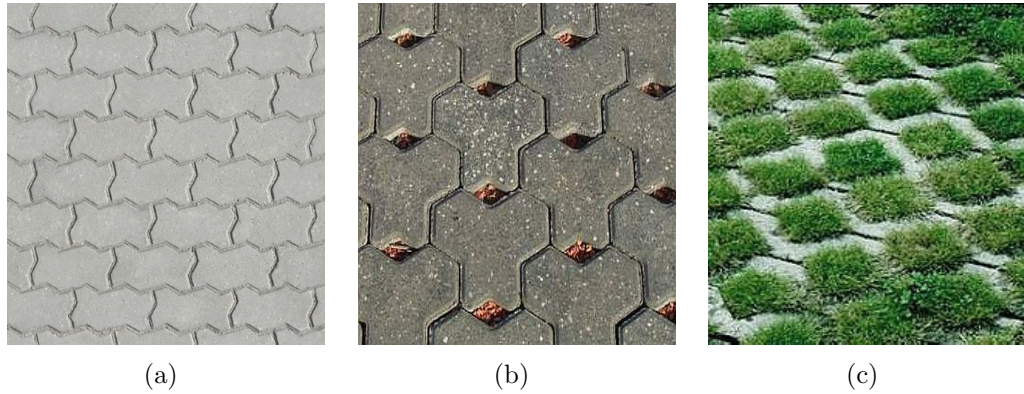


Figure 2.5: Different types of paved surfaces.

The runoff coefficient in an urban catchment area is highly influenced by the impervious and pervious surface characteristics, as they play a big role in creating discharge and affecting the amount of rainwater entering a storm sewer system (Ravagnani et al. [101]). The process of urbanization involves the increase of impervious surfaces by encroaching natural watersheds and vegetation. In fact, the urbanization pro-

cess and the increase in impervious surfaces are the flip side of a coin. Impervious surfaces such as those with concrete and asphalt layers on top do not allow water to percolate through them. In cases of precipitation, this surface produces maximum runoff, leading the water into the drainage network. Urban flooding is mainly caused by ‘rainfall overwhelming drainage capacity’, so proper identification of impervious surfaces is an important task in modelling urban flooding (Aktaruzzaman and Schmitt [4]).

A considerable amount of remote sensing research has focused on the issue of how to accurately map impervious surfaces. Ridd [102], Ji and Jensen [72], and Wu and Murray [133] mostly use statistical classification approaches with moderate-resolution satellite imagery. Hodgson et al. [64] use high-resolution aerial images and LiDAR height data for mapping urban parcel imperviousness. The automatic detection of different types of land cover from satellite imagery can be traced back to 40 years ago. This was the time when the Landsat-1 satellite was launched into space. Statistical classification approaches such as maximum likelihood (supervised) and ISODATA clustering (unsupervised) were widely used until the mid-90s by many researchers (Anderson and Anderson [8]; Anderson et al. [9]; Jensen [70]; Smith et al. [120]). With the emergence of a new generation of satellite images, e.g. IKONOS and QUICKBIRD, with finer spatial resolution, researchers in the field of remote sensing have tended to switch to non-statistical land cover classification approaches such as artificial neural networks and expert systems. One of the main advantages of non-statistical approaches over statistical approaches is that there is no need to make any statistical assumptions (Tullis and Jensen [122]; Hodgson et al. [64]). Both neural networks and expert systems are approaches that require a considerable amount of human interaction to train the datasets; this is often tedious and time-consuming. A neural network can mimic the human brain by learning and adapting itself to better classify a dataset. Neural networks are designed by assigning a hidden weighting layer which cannot be modified directly by the users during the application period (Tullis and Jensen [122]). On the other hand, expert systems are designed from the knowledge base of human expertise that users can directly control [141]. Expert systems are easy to implement and are more widely used than neural networks [142].

Frankhauser [48] uses high resolution aerial images (25cm, 30cm and 75cm) in order to automatically detect impervious areas in an urban scene by applying a pixel-based maximum likelihood classifier (MLC). Despite satisfactory accuracy ($>90\%$), the classified image shows some misclassified pervious pixels on the rooftops and some impervious pixels in the middle of pervious areas. Frankhauser [48] explains that MLC attempts to classify each individual pixel instead of taking into account the spatial information of the neighbouring pixels.

Pixel-based image classification exploits only spectral information hidden in each pixel as digital numbers (DNs) and calculates some kind of spectral similarity measures (Gao and Mas [50]; Dean et al. [30]). This type of approach does not consider spatial and contextual information about the image. The efficiency of the pixel-based classification approach is questionable when dealing with high resolution satellite imagery such as QUICKBIRD (Xiaoxia et al. [134]). In order to overcome the limitations of the pixel-based image classification, the concept of Object-based Image Analysis (OBIA) has gained popularity recently. The idea of OBIA was first introduced in the 1970s when Kettig and Landgrebe [75] propose an image classifier by using both the spectral and spatial information (De Kok et al. [78]). The concept of OBIA gained further popularity with the development of edge-based and texture-based segmentation algorithms (Haralick and Shapiro [57]; Hofman et al. [65]). In the last decade, the astonishing improvement in computer hardware and computational power, the availability of high-resolution satellite imagery and the emergence of Definiens software [156] have triggered a massive demand for the OBIA approach. The OBIA approach segments an image into a number of homogeneous image objects. Afterwards, a knowledge-based rule-set approach or nearest neighbour classifier is used to assign a class label to each segmented image object (Myint and Stow [91]). In the OBIA approach the classifiers are soft-classifiers which means that they are designed based on the theory of fuzzy logic. A soft-classifier assigns a class label to an image object by using a membership function (Dehvari and Heck [31]). The rule-set approach also uses a membership function in order to define the user's expert knowledge to guide the classification procedure (Myint and Stow [91]).

In this study, the OBIA approach has been used in order to extract urban land cover types using high resolution (10cm) aerial images and LiDAR intensity data. The accurate detection of land cover types can ensure appropriate assignment of runoff coefficients to an existing urban flood model and improve the quality of rainfall-runoff modelling while using 1D-2D approach.

Chapter 3

Materials and data types

3.1 Introduction

This chapter contains information on the study areas, different source of data types and software packages used in this research work. The quality of various data sources influences the desired level of accuracy in the output map. The application of suitable data processing techniques depends on the inherent characteristics of the data.

3.2 Study area

Two test areas with different topographic characteristics are chosen for this study. Both of the areas are located in the neighborhood of the University of Kaiserslautern, Germany. The first area is known as Alcatraz and has a spatial covering of $244\text{m} \times 175\text{m}$. This is a fairly residential area with few trees and a very steep slope. Figure 3.1(a) presents the aerial image of the Alcatraz study area. The second test area is also located near the University of Kaiserslautern and has a larger spatial covering of $300\text{m} \times 510\text{m}$. This area is known as Casimirring and has a smoothly varying slope. Figure 3.1(b) presents the aerial image of a part of the Casimirring study area. This area contains a large number of trees, bushes and complex roof



Figure 3.1: Aerial image of the Alcatraz dataset (a) and a part of the Casimirring dataset (b).

planes. Throughout this research work, these two study areas are taken as case studies and the LiDAR data processing techniques are implemented for both the study areas towards generating high resolution spatial database. A third study area is chosen in this research work as an additional investigation for detecting grassland, bare soil and other impervious surfaces. This study area is called Harzhübel and also locates in the neighborhood of University of Kaiserslautern. In Chapter 7, Figure 7.15(a) illustrates the aerial image of the Harzhübel study area. However, this study site is exempted from implementing any LiDAR filtering, object classification and street extraction algorithm. Figure 3.2 presents the city map of Kaiserslautern city indicating the location of the three study sites.

3.3 LiDAR data

LiDAR data was acquired over both the study areas with Optech ALTM 300 sensor on 1st April, 2007. BSF Swissphoto, a Switzerland-based company, was responsible for acquiring LiDAR data over the Kaiserslautern city area. The density of the acquired LiDAR data is 4 points/m² and was supplied as ASCII data with elevation



Figure 3.2: The citymap of Kaiserslautern city and the location of the study areas.

and intensity information. The unstructured point data is resampled into grid data for visualization and digital image analysis purposes. Figure 3.3(a) shows LiDAR range image featuring elevation data where dark pixels represent lower elevation and bright pixels represent higher elevation. Figure 3.3(b) shows LiDAR intensity image featuring different surface characteristics.

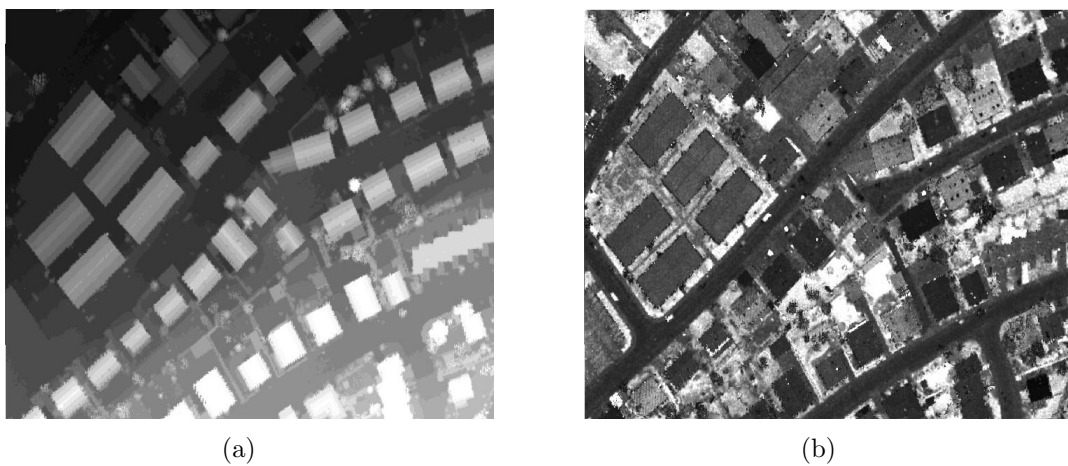


Figure 3.3: LiDAR elevation data (a) and intensity data (b) of the Alcatraz study area.

3.4 Aerial images

The aerial images of both study areas were scanned in April, 2008. Both the images have three colour channels (red, green and blue) and spatial resolution of 10 cm. This high resolution image can even capture humans on the ground. Figure 3.4(a) shows some people playing soccer on the University playground. Street elements such as sidewalks, kerbs and even manholes can be seen in the high resolution aerial images used in this study (Figure 3.4(b)). Thus, high resolution aerial images contain spectrally rich information requiring robust processing techniques and posing a challenge to efficient computational power.



Figure 3.4: High resolution image capturing soccer players (a) and detailed street view (b).

3.5 Topographic maps

The topographic maps are generally vector-based 2D representations of a study area in a geographic information system (GIS) database. Geometric primitives such as points, lines and polygons are the key elements for delineating topographic objects in any vector-based representation. Roads and rivers are presented as linear or curvi-

linear lines in a low-resolution topographic map. In a high-resolution topographic map, those features usually appear as polygons. In this study, a high-resolution topographic map of Kaiserslautern city featuring street network (Figure 3.5(a)) and building polygons (Figure 3.5(b)) is used. The quality of the topographic maps is



Figure 3.5: Topographic map of street networks (a) and buildings (b).

assessed by overlaying them on the aerial image. In Figure 3.6, the location, orientation and shape of the topographic maps are checked against the reference image. When overlaid on the aerial image, the building polygon maps appear to cover part of the building roofs leaving some roof areas exposed (Figure 3.6(a)). The reason behind this underrepresentation can be linked to the fact that building polygons collected from field survey data usually estimate only the floor plan of a building. The use of underrepresented building polygon maps can introduce errors in estimating the total roof areas which is important for runoff volume generation. In this research work, an attempt has been made to generate accurate building polygon maps by automatically detecting the roof outlines (Chapter 5). However, the qual-

ity of the street polygon maps shows exact correspondence with the reference image (Figure 3.6(b)).

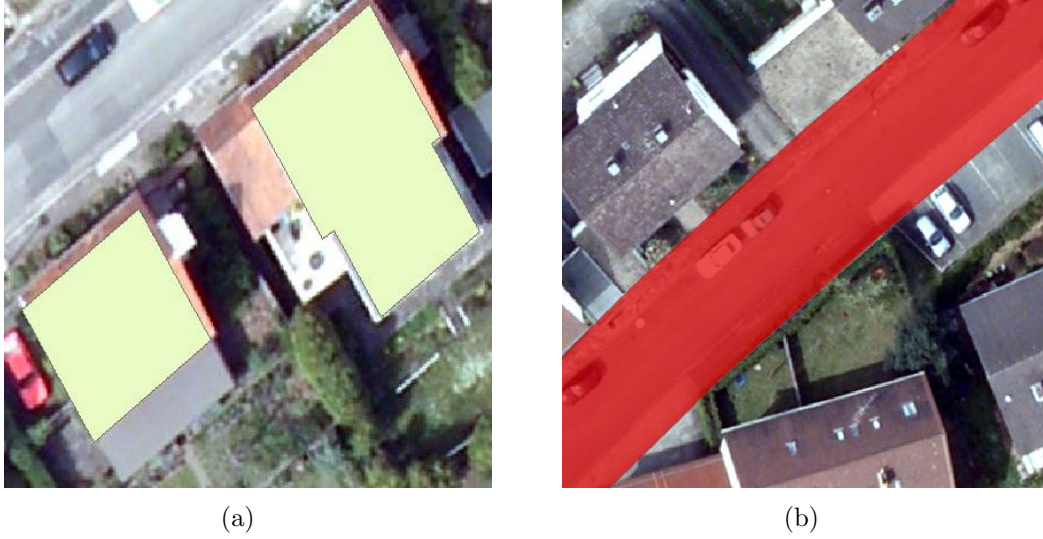


Figure 3.6: Topographic map of buildings (a) and streets (b) overlaid on the aerial image.

The quality testing of the topographic maps is important for the implementation of an automatic street extraction algorithm. Displacement in position and orientation of the topographic maps may yield unrealistic object representation in the output map while using any standard object extraction algorithm that combines digital image and spatial database. In this study, the proposed building extraction algorithms working on LiDAR data makes the use of topographic maps redundant. On the contrary, the proposed street extraction and modelling approach takes into account the street topographic maps which are already well-aligned with the reference image.

3.6 Image and LiDAR data co-registration

Image registration is the technique of bringing different datasets into a single coordinate system. However, multiple datasets acquired by different sensors but having the same coordinate system may still require some kind of additional pixel-to-pixel or point-to-pixel matching in order to ensure higher reliability in data fusion tech-

niques. This kind of matching is known as image co-registration. For example, LiDAR has a horizontal accuracy of 50cm and raw LiDAR point data often need to be co-registered with a reference image. When overlaid together, LiDAR data on the Alcatraz study area shows a clear horizontal shift in relation to the aerial image (Figure 3.7(a)). In this study, the LiDAR point data are aligned with the reference aerial image using a projective transformation. While performing image co-registration, the RMS (Root Mean Square) errors are kept to 0.02m in both the X and Y directions. The employment of the co-registration technique improves the overall alignment of both the datasets (Figure 3.7(b)).

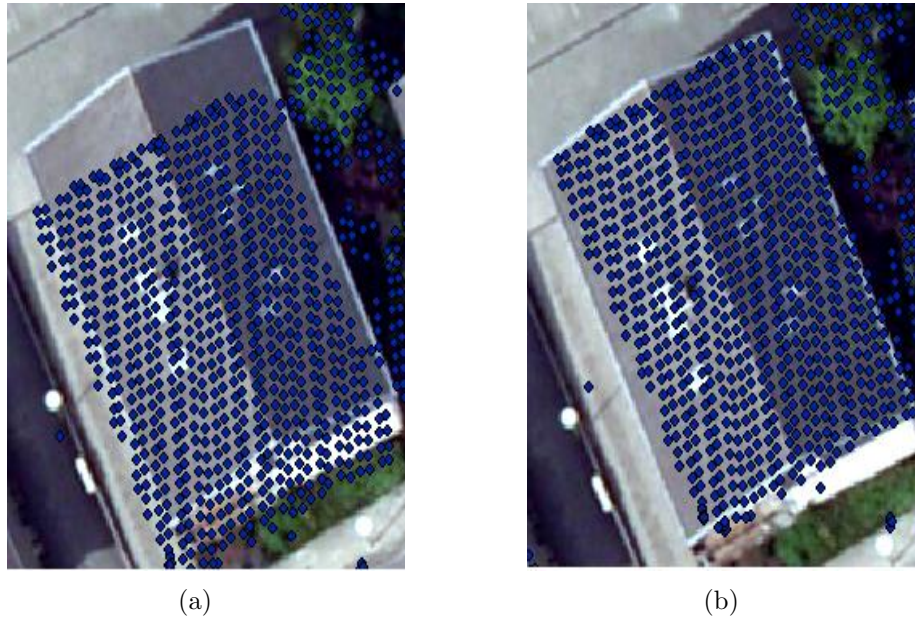


Figure 3.7: Co-registration of LiDAR data and aerial image: LiDAR point data overlaid on the building before (a) and after (b) performing image co-registration technique.

3.7 Accuracy assessment and error matrix approach

While remotely-sensed data are capable of providing a great deal of information on the characteristics of the earth's surfaces, an appropriate technique of accuracy assessment is necessary for the qualitative analysis of these data and their meaningful

application (Senseman et al. [113]). Accuracy assessment is performed by comparing a classified map derived from automated image classification with a reference map produced from field data or ground truth data. This method follows a pixel-by-pixel comparison between the classified and reference maps of a specific area with identical thematic information. The common practice for generating a reference map is to collect an adequate number of sample points representing each theme of a study scene. The choice of an appropriate sampling technique is important in order to produce adequate sample points which are representative of the land use classes. The main steps in performing an accuracy assessment are:

1. Selecting sampling scheme
2. Error matrix computation and analysis

3.7.1 Selecting sampling scheme

The following five common sampling techniques are widely used in the remote sensing community:

- Random sampling
- Systematic sampling
- Stratified random sampling
- Stratified systematic unaligned sampling
- Cluster sampling

Each technique has its advantages and disadvantages. For details of each of the technique, readers are referred to (Senseman et al. [113]; Jensen [71]). In this study, a random sampling scheme is chosen for generating reference data.

3.7.2 Error matrix computation and analysis

An error matrix is a two dimensional matrix or table displaying statistics of a classified map and a reference map for assessing the classification accuracy [148]. The

	Reference map					
		class 1	class 2	class 3	class 4	Totals
Classified map	class 1	D1				R1
	class 2		D2			R2
	class 3			D3		R3
	class 4				D4	R4
	Totals	C1	C2	C3	C4	$T = \sum R/C$

Table 3.1: An error matrix of four classes

error matrix is also known as a confusion matrix. The error matrix allows performing a number of statistical measures such as user's accuracy, producer's accuracy, errors of omission and errors of commission and overall accuracy for describing the accuracy of the classified map with respect to the reference map. In an error matrix, the vertical columns represent the thematic classes of the reference map while the horizontal rows correspond to the classified map derived from automated image classification. There is no hard and fast rule for that and the orientation of the recorded data in rows and column can be inverted [148]. Table 3.1 shows an error matrix of four imaginary classes.

The value of a diagonal cell of the error matrix represents the correctly classified pixels/points and the sum of the diagonal cells ($\sum D$) represents the total number of correctly classified pixels/points. The ratio of the correctly classified pixels to the total number of pixels is termed as 'overall accuracy'. For each column in the error matrix, the ratio of the correctly classified pixels to the total number of pixels represents producer's accuracy for each thematic class. Conversely, for each row in the error matrix, the ratio of the correctly classified pixels to the total number of pixels represents user's accuracy for each thematic class. For each column in the error matrix, the total of the non-diagonal cell values represents the number of pixels which are incorrectly classified. The misclassified pixels propagate to other classes. The ratio of the total number of misclassified pixels to the total number of pixels contained in that column is known as the error of commission. Similarly, for each row, the number of incorrectly classified pixels gives an indication of how many pixels from other sources are included in that particular class. The ratio of misclassified pixels included in a class to the total number of pixels in a given row is known as the error of omission. An image analyst can interpret the image by

looking at the computed descriptive statistics from the error matrix. The analyst has the option to improve the classification accuracy by retraining the datasets and choosing a different approach in case the produced results are not satisfactory.

3.8 Software packages

A number of software packages are used in this research study for the purpose of data processing, analysis, visualization, output map generation and running the flood simulation model. The software packages are listed below with their main features,

3.8.1 ArcGIS

ArcGIS is a collection of GIS software suits produced by ESRI [157], Redlands, California. ArcGIS consists of software packages such as ArcMap and ArcScene. ArcMap is responsible for geospatial data preparation, organization, analysis and map creation. ArcScene is used for 3D analysis and visualization. In this study ArcMap is used mainly for the purpose of data conversion. The raw LiDAR data provided as ASCII file can be easily converted to 3D feature class by using spatial analysis toolbox. This 3D feature class can be converted to grid/raster data by choosing a user defined grid size. When converted to grid data, this format is also known as LiDAR depth image upon which image processing algorithms can be applied for further processing.

3.8.2 MATLAB

MATLAB is the acronym for matrix laboratory and is a product of MathWorks [155]. MATLAB provides an excellent numeric computing environment for the manipulation of data mainly in matrix format, 2D and 3D visualization, programming, image processing and implementation of algorithms. In this study, MATLAB has been extensively used in order to implement algorithms for processing LiDAR data. The

task of programming pertaining to LiDAR data filtering, object classification and 3D street modelling is implemented in MATLAB environment.

3.8.3 ECognition/Definiens

Definiens is an Object-based Image Analysis (OBIA) software produced by Germany-based Definiens GmbH [156]. Definiens offers a number of image segmentation tools and flexibility to design decision rules for the purpose of classification. In this study two types of segmentation algorithm: the chessboard and multiresolution segmentation algorithms are used. The application of chessboard segmentation with the help of thematic maps allows the users to select ROI (Region of Interest). The implementation of multiresolution segmentation produces spatially and spectrally homogeneous object patches which are the building blocks of the OBIA approach.

3.8.4 MIKE FLOOD

MIKE FLOOD is a collection of flood modeling software packages produced by DHI. MIKE FLOOD consists of MOUSE, MIKE 11 and MIKE 21 engines. MIKE FLOOD software brings together the modules MIKE 11, MOUSE and MIKE 21 into a single modelling platform featuring a dynamically coupled modelling environment. The coupling of more than one module offers the advantage of reaping the benefit of all the modules. The module MIKE 11 is mainly responsible for modelling 1D flow in rivers, irrigation channels and estuaries. The module MOUSE offers modelling of 1D flow in sewer pipes and other closed conduits. Modelling of 2D flow can be implemented using the module MIKE 21.

3.9 Conclusion

Three sources of datasets - 1) LiDAR point data, 2) aerial image and 3) topographic maps - are used in this study to generate a high-resolution digital surface model. High-density LiDAR data (4 points/m²) and high-resolution aerial images (10cm) are the potential data sources for exploiting accurate surface information

of a complex urban scene. The necessity of image and LiDAR data co-registration plays an important role on the accuracy of object classification. Special care is needed to take during the image co-registration process while using a commercial software package. The MATLAB computing environment is capable of handling and manipulating large volume of LiDAR point cloud and offers excellent flexibility in implementing data processing algorithms. The use of MIKE FLOOD software verifies the applicability of the generated high-resolution database by feeding them into 2D hydrodynamic model.

Chapter 4

Filtering LiDAR data

4.1 Introduction

This chapter presents a filtering algorithm based on the concept of surface fitting. This filtering technique is applied directly to the raw LiDAR point data in order to separate ground and non-ground points. Two study sites: the Alcatraz and the Casimirring are taken as the case studies. The purpose of this chapter is thus two-folds: 1) to propose a filtering algorithm suitable for raw point cloud and based on the idea of standard plane equation by least square fitting; and 2) to incorporate the idea of threshold parameter in the filtering algorithm to influence LiDAR data segmentation according to the requirement.

4.2 Proposed algorithm

As already described in Chapter 2 (Literature review), many filtering algorithms have been developed in recent years with the intention of segmenting LiDAR data into ground (i.e. terrain) and non-ground (i.e. buildings, trees) points. Apart from ground and non-ground points, an urban catchment contains a number of other man-made objects such as boundary walls, thin embankments, elevated basements of houses, fences and hedges. These objects have a potential impact on the flow

dynamics of flood water during a surface flooding event. In Abdullah et al. [1], these objects are termed 'micro objects'. The sensitivity of the LiDAR filtering algorithm might affect the performance of the flood simulation model were it to underestimate the object definition. Objects such as boundary walls, fences and other artificial objects may be erroneously removed from DTM if the height and slope threshold value of the filtering algorithm is set too low (Neelz and Pender [94]).

In this study, a filtering algorithm is proposed with the intention of detecting micro objects. The proposed algorithm is based on the idea of fitting a standard plane equation in 3D space. In Aktaruzzaman and Schmitt [5], this proposed LiDAR filtering algorithm with the concept of 3D plane equation is described in great details. In reality, the characteristics of a terrain are complex. The earth's surface is not flat at all due to the existence of valleys, reliefs and objects (buildings and trees). The bare earth surface can be assumed to be a flat plane in a small patch of land. This is the assumption behind the proposed algorithm to be presented here. But in real case small depressions and ridges might be present on the surface ground. The attempt of fitting a standard plane equation over a surface ground is disturbed by the presence of the aforementioned depressions and ridges. But by considering an appropriate height threshold value, those depressions and ridges can be considered within the influence zone of the flat plane surface. This proposed algorithm consists of the following steps:

1. selecting the block size
2. application of a standard plane equation in 3D space
3. minimum point elevation determination
4. fitting the plane

All the steps mentioned above are discussed elaborately in the following subsections.

4.2.1 Selecting the block size

The formation of square/rectangular block within a study area offers small patches of land areas suitable for applying a filtering algorithm. A small surface patch

retains local terrain characteristics and thereby gets less vulnerable to global terrain complexities. A surface based filtering algorithm aiming at operating on block basis would ensure the maximum accuracy in separating ground and non-ground points. The whole study area is split up into a number of blocks by choosing a user-defined threshold which depends on the size of the largest building in the scene (Axelsson [10]; Salah et al. [109]). Figure 4.1 presents the concept of generating blocks within the study area. Let $P_1P_2P_3P_4$ be an arbitrary study area and $abcd$ is a rectangular block within this area. Let L_x is the length and L_y is the width of the block. In the case of a square block, L_x and L_y are identical. The size of the block is determined by the formula;

$$L_x = D_1/K \quad (4.1)$$

$$L_y = D_2/K \quad (4.2)$$

Where,

- L_x Length of the block
- L_y Width of the block
- D_1 Distance between points P_1 and P_2
- D_2 Distance between points P_1 and P_4
- K A constant value depending on the scene and larger than the length of the biggest building.

4.2.2 Standard plane equation in 3D space

The second step is to fit a standard plane in each block. The task of block-wise plane equation fitting ensures higher accuracy in LiDAR point data separation while preserving the local topographic characteristics. Before exploring the plane-fitting approach, it is important to discuss the mathematical definition of a standard plane in 3D space. The standard equation of a plane in 3D space is,

$$Ax + By + Cz + D = 0 \quad (4.3)$$

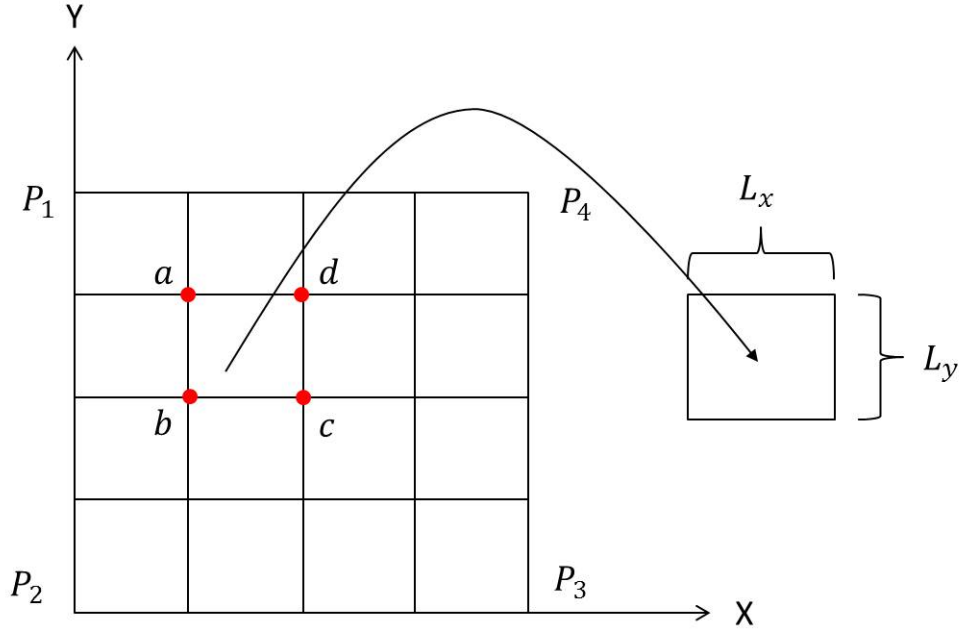


Figure 4.1: The concept of creating surface block. $P_1P_2P_3P_4$ is the whole study area and $abcd$ is one block within the study area.

The equation of the standard plane can be rewritten as follows,

$$z = -\frac{A}{C}x - \frac{B}{C}y - \frac{D}{C} \quad (4.4)$$

This takes the following form,

$$z = ax + by + c \quad (4.5)$$

Where, $a = -\frac{A}{C}$, $b = -\frac{B}{C}$ and $c = -\frac{D}{C}$. The above equation has three unknowns and thus requires a minimum of three equations to solve it. The required three equations can be obtained when the plane passes through three points (x_1, y_1, z_1) , (x_2, y_2, z_2) and (x_3, y_3, z_3) in space.

$$z_1 = ax_1 + by_1 + c \quad (4.6)$$

$$z_2 = ax_2 + by_2 + c \quad (4.7)$$

$$z_3 = ax_3 + by_3 + c \quad (4.8)$$

The above equations give rise to a system of linear equations and can be solved by Gaussian elimination method in order to obtain the coefficients a , b and c .

4.2.3 Selecting points with minimum elevations within a block

The third step in this method is to make a least square fit of the plane derived in step two for each block. The purpose of selecting these points is to solve the plane equation and determine the coefficients. Placing the plane model into a block primarily requires a minimum of three points. In this study, four minimum points are chosen for each block. The extra point provides additional set of points permitting the solvers to choose best fitted solutions. More specifically, these are the four points with minimum height and searched for along the four borders lines for each surface block. Figure 4.2 shows the detection of minimum elevation points along the border lines within a block. P1P4 is a border line and Q1Q2 is a line drawn parallel to P1P4. The distance P1Q1 should be greater than LiDAR resolution (> 0.25 m). It is decided to set P1Q1 equal to 0.35 m and P1Q1Q2P4 forms a thin rectangular patch. The minimum elevation point B is searched for within the rectangle P1Q1Q2P4. The reason for considering this rectangular thin patch instead of only border line is that the noisy and random LiDAR data along only P1P2 may not have representative minimum value. So, the consideration of a thin patch alongside the border line increases the search domain as shown in Figure 4.2.

4.2.4 Fitting the plane

In this step, the four minimum points are fed into the standard plane equation in order to calculate the coefficients of the plane equation. Once the calculation of three coefficients is completed, they are used to calculate the new z (height) value on the plane for each individual point (x_i, y_i) lying within each block. Later the original z value of LiDAR point data for each individual point is compared against the calculated (plane-fitted) z value. At this point, the position of an original z

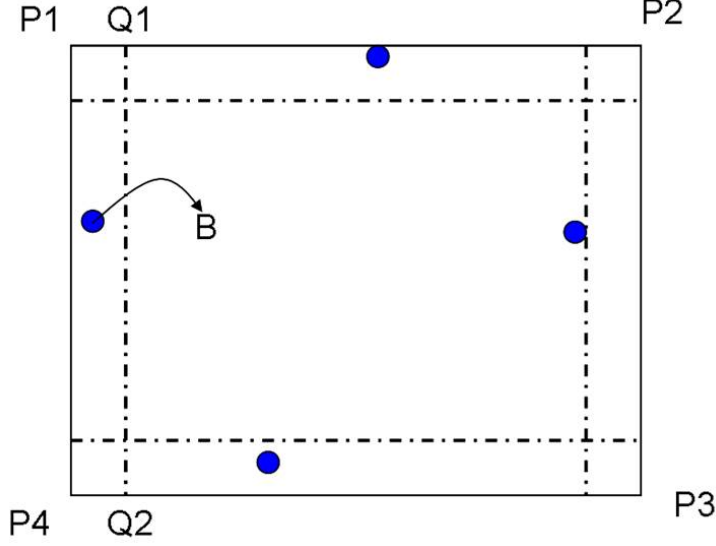


Figure 4.2: Detection of minimum elevation point along the borders. Here surface block border P4P1 has minimum elevation point at B.

elevation point in relation to the calculated (plane-fitted) z value can be described in the following ways:

- i) The original z value is greater than the calculated z value

$$Z_{\text{ori}} > Z_{\text{cal}}$$

- ii) The original z value is equal to or approximately equal to the calculated z value

$$Z_{\text{ori}} = Z_{\text{cal}} \quad \text{or} \quad Z_{\text{ori}} \approx Z_{\text{cal}}$$

- iii) The original z value is smaller than the calculated z value

$$Z_{\text{ori}} < Z_{\text{cal}}$$

In the first case, the original z points are the object points. However, a threshold is set with the calculated height and an original z point greater than this threshold ($Z_{\text{ori}} > Z_{\text{cal}} + \Delta h$) is labelled as a non-ground point. In the second case, any

original z point lying within the threshold $\Delta h (Z_{\text{ori}} < Z_{\text{cal}} + \Delta h)$ is labelled as a ground point. In the last case, the original elevation points are considered as ground points. Those are the points featuring the local depressions or outliers. The implementation of the algorithm is represented by the flowchart in Figure 4.3. Apart from the aforementioned cases, sometimes LiDAR points may contain signals returned from birds and power lines (Stoker et al. [121]). In this situation the original z points rest too high from the calculated z point ($Z_{\text{ori}} \gg Z_{\text{cal}} + \Delta h$). These points are declared as outliers if there are any. In Figure 4.4, the bottom black line symbolizes fitted plane in the LiDAR point data and the broken red line is the demarcation line of the threshold value. Any point above this broken red line is a non-ground point.

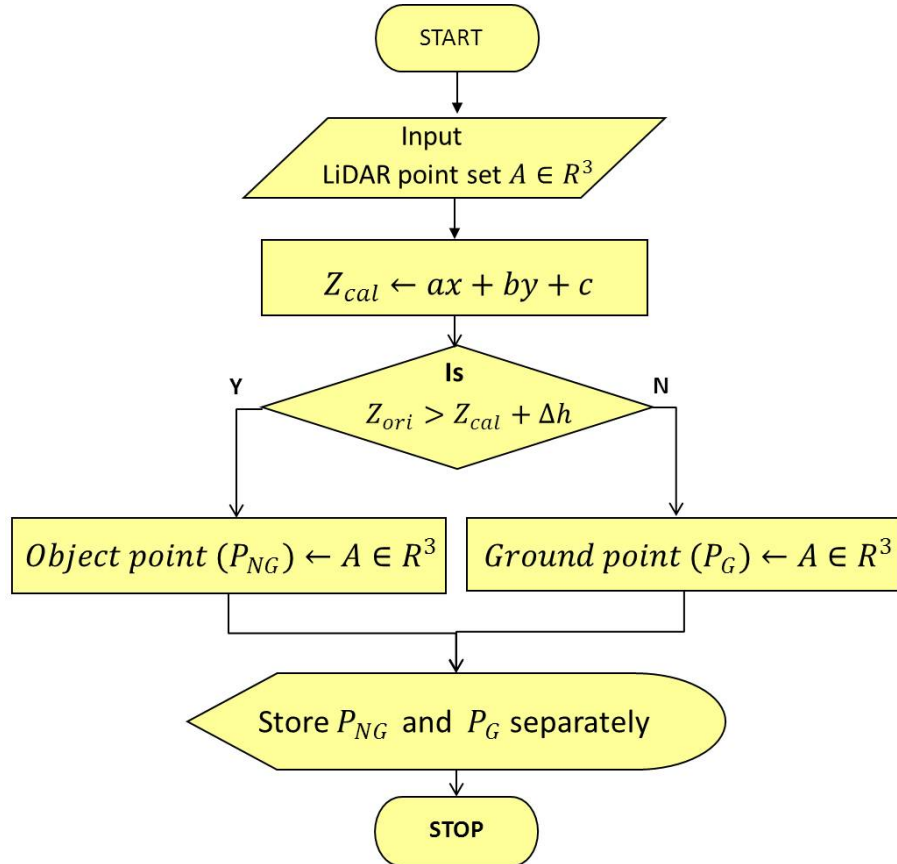


Figure 4.3: Flowchart of plane fitting algorithm.

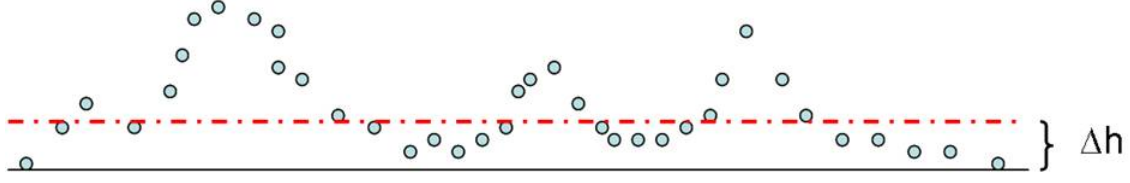


Figure 4.4: Separation of non-ground points greater than the threshold (Δh) from the plane.

4.3 Results and discussions

In order to test its effectiveness, the proposed algorithm is applied to two study areas: 1) the Alcatraz and 2) the Casimirring. The following subsections present the application of the filtering algorithm to both the areas.

4.3.1 Alcatraz study area

The Alcatraz study area has a very steep slope as well as some challenging terrain features including stairs, high basement walls and boundary walls. Figure 4.5 features the cross-sectional profile of the Alcatraz study area along the NE-SW direction. The minimum and maximum elevations are found to be 244m and 268m respectively along this profile. The largest building is 40m long which provides information for choosing an appropriate grid size. The standard plane fitting algorithm is implemented with a threshold (Δh) of 1.5m in order to separate the ground and non-ground points. Figure 4.6(a) illustrates the segmented results where blue points denote the objects and red points denote the grounds. Figure 4.6(b) presents the aerial image of the Alcatraz area as a reference map for qualitative assessment of the applied filtering algorithm.

In order to assess the quality of the LiDAR point data segmentation, an error matrix approach is adopted. The error matrix approach allows the use of two thematic maps; one is a reference map or ground truth map and the other is a classified map that is produced after applying the filtering algorithm. In this case the reference map is the aerial image and the classified map is the segmented LiDAR point data. There are only two classes in the segmented LiDAR data, ground and non-ground

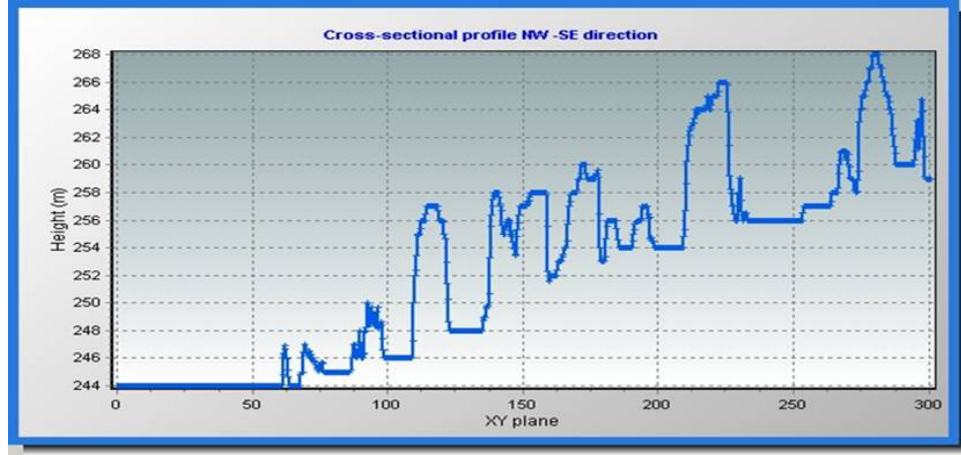
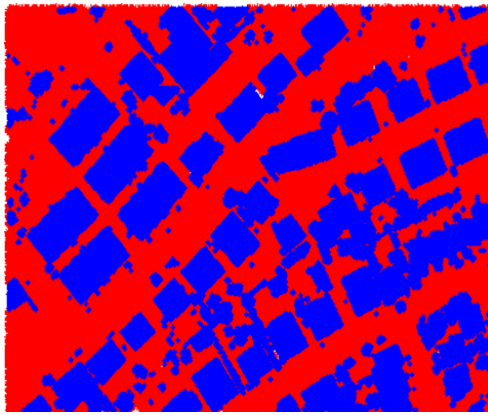


Figure 4.5: Cross-sectional profile of digital surface model of Alcatraz study area.



(a)



(b)

Figure 4.6: Segmentation of LiDAR point data into objects (blue) and terrain (red) using plane fitting algorithm.

points. The error matrix compares how similar the segmented ground and non-ground points are compared to the reference image. For the error matrix test, 150 randomly distributed points are generated across the whole study area and later overlaid it on the aerial image to visually distinguish between ground and non-ground points. Table 4.1 presents the computed error matrix for the Alcatraz area. In an error matrix, the diagonal elements represent the correctly classified points. The ratio of correctly classified points to the total number of points is known as

overall accuracy. The computed overall classification accuracy for the Alcatraz area is 96.66%. The other classification accuracies are presented in Table 4.2.

	Reference map		
Classified map		Objects	Ground
	Objects	64	3
	Ground	2	81

Table 4.1: Error matrix of Alcatraz dataset for filtering algorithm.

	Ground	Non-ground
User's accuracy (%)	96.43	96.96
Producer's accuracy (%)	97.6	95.53
Errors of omission (%)	3.57	3.04
Errors of commission (%)	2.40	4.47

Table 4.2: Calculation of various accuracies of Alcatraz area.

The ground points have errors of omission of 3.57% and errors of commission of 2.4% while object points have errors of omission of 3.04% and errors of commission of 4.47%. One important issue to mention here is the definition of reference object against which the classified (filtered) map is compared. At this point only buildings and trees are considered as objects leaving the boundary walls, bushes and fences as ground points. The next section will discuss the importance of sensitivity of a filtering algorithm which can alter the object definition of the extracted objects.

4.3.2 Sensitivity of the filtering algorithm

The performance of the filtering algorithm in terms of object separation can be influenced by setting appropriate threshold values. By sensitivity of a filtering algorithm, the study refers to the height threshold as the plane fitting algorithm takes into account the height difference calculated from the plane to a point to be classified. The definition and choice of the threshold type will be different for slope-based filters (Vosselman [128]; Roggero [103]; Sithole [118]; Shan and Sampath [115]) and morphological filters (Zhang et al. [139]; Zaksek and Pfeifer [135]; Chen et al. [27]). To explain the influence of the height threshold in object separation from LiDAR point

data, two different height thresholds of 1m and 1.8m are chosen in the plane fitting filtering algorithm. Figure 4.7(a) presents objects (in blue) separation from LiDAR data with a height threshold of 1m. This is the example of setting a low threshold value. The position S1 indicates boundary walls next to a building and S2 indicates garage and bushes. Figure 4.7(b) presents objects (in blue) with a height threshold of 1.8m which is the example of setting a relatively high threshold. Position S1 shows no boundary walls and position S2 shows less dense object information. This is an obvious example of how threshold value can influence LiDAR point data

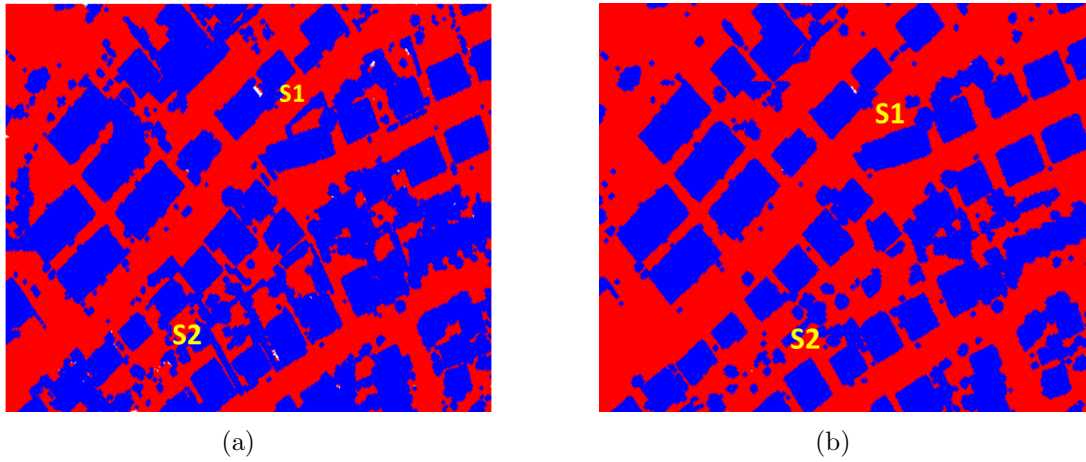


Figure 4.7: Influence of height threshold in object separation.

segmentation. The plane fitting algorithm is flexible enough to set a threshold value according to the requirements of the users.

4.3.3 Casimirring study area

The Casimirring study area has a larger scene coverage (510m x 292m) and features a gradual slope change across the landscape. This study area has a relatively large number of trees. Most of the trees have large amounts of foliage being attached to the buildings and sometimes overshadowing them. This area also contains dense low-vegetation and hedges. Figure 4.8 shows the transverse cross-section of the digital surface model of the Casimirring study area. The standard plane fitting algorithm is applied to the LiDAR point data of the Casimirring study area. In

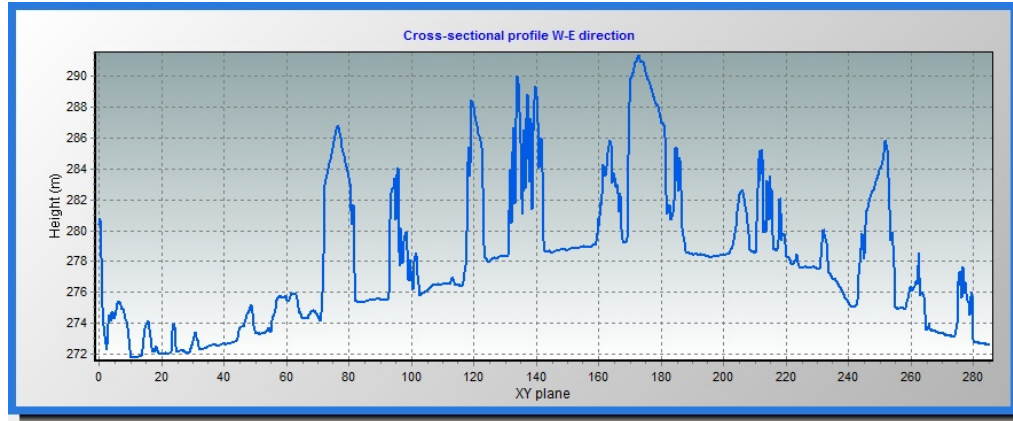


Figure 4.8: Cross-sectional profile of digital surface model of Casimirring study area.

this case a chosen height threshold (Δh) of 1.5m is set in relation to the fitted plane. Figure 4.9(a) illustrates the segmented results where blue points denote the objects and red points denote the grounds. Figure 4.9(b) presents the aerial image of the Casimirring area as a reference map for the qualitative assessment of the applied filtering algorithm. In order to assess the quality of the filtering algorithm, an error matrix test is performed in a similar way to that described for the Alcatraz dataset. Table 4.3 shows the computed error matrix for the Casimirring study area. The overall accuracy is reported to be 97%. Table 4.4 presents user's accuracy, producer's accuracy, errors of omission and errors of commission of the Casimirring area. The ground points have errors of omission of 3.53% and errors of commission of 2.29% while object points have errors of omission of 1.8% and errors of commission of 4.49%.

Classified map	Reference map		
		Objects	Ground
	Objects	85	4
	Ground	2	109

Table 4.3: Error matrix of Casimirring area for filtering algorithm.

	Ground	Non-ground
User's accuracy (%)	98.2	95.51
Producer's accuracy (%)	96.47	97.71
Errors of omission (%)	3.53	2.29
Errors of commission (%)	1.8	4.49

Table 4.4: Calculation of various accuracies of Casimirring area.

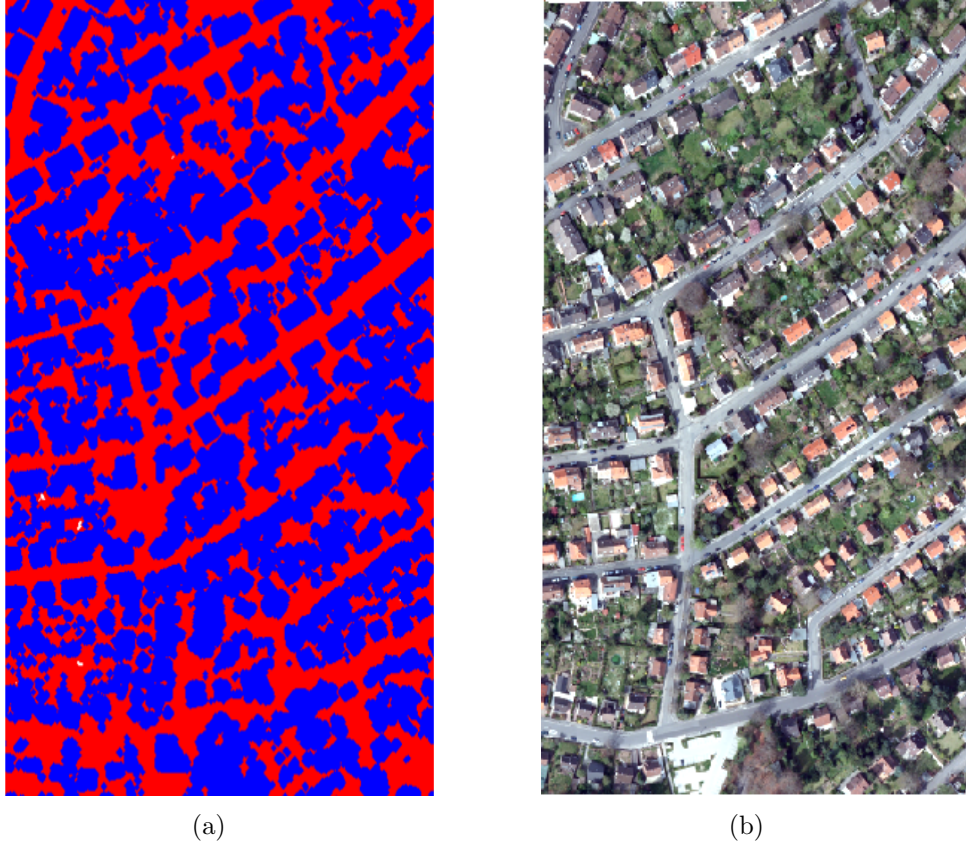


Figure 4.9: Segmented LiDAR data into ground (red) and non-ground (blue) points (a). The aerial image of the Casimirring study area (b).

4.3.4 Sensitivity of the algorithm on threshold selection

In order to analyse the sensitivity of the proposed segmentation algorithm, two different threshold values (Δh) of 1.5m and 1m are set into the algorithm. Different choices of produce different output maps with varying levels of object details. The choice of threshold (Δh) 1.5m mainly attempts to classify buildings and trees of

medium to large height as non-ground points. The low-lying vegetation, small bushes and boundary walls that fall within this threshold value are therefore classified as ground points.

Visual inspection of Figure 4.10(a) and Figure 4.10(b) generated by choosing threshold values of 1.5 m and 1.0 m respectively reveals comparatively dense object information for the latter threshold. Statistics on the number of the extracted objects using two different thresholds also show agreement on this issue. The Casimirring dataset has 509,387 LiDAR points and threshold value of 1.5 m extracts 209,433 points while a threshold value of 1.0 m extracts 250,265 object points.

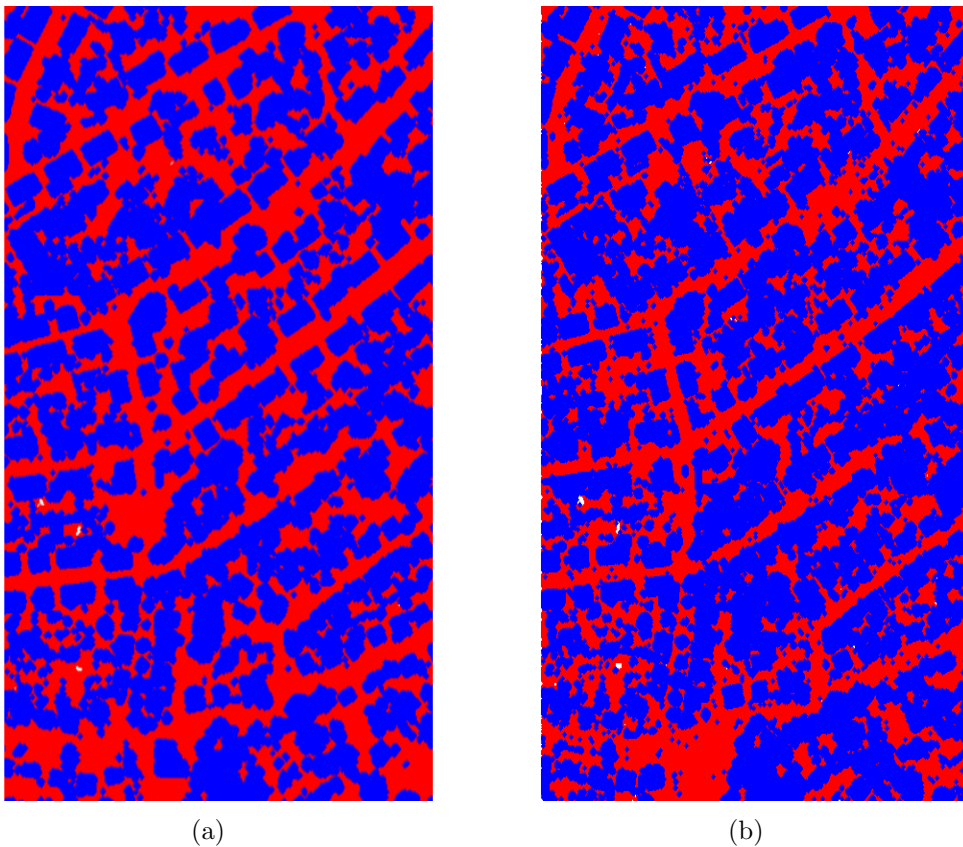


Figure 4.10: Effect of thresholding in object separation in Casimirring dataset: Higher threshold extracts coarse objects information (a). Smaller threshold extracts dense object information (b).

4.4 Conclusion

In this chapter, a simple but robust plane fitting algorithm has been proposed in order to separate LiDAR point data into ground and non-ground points. This algorithm incorporates the idea of choosing a suitable threshold value that has potential influence in detecting different levels of objects. The proposed plane fitting algorithm performs substantially well in two different study areas with varied topography. Application of a filtering algorithm is the primary step in processing LiDAR data. The accuracy of the following classification and object detection algorithms largely depends on the efficiency of the associated filtering algorithm. Although researchers in the field of geosciences have come up with a variety of sophisticated filtering algorithms, the suitability of a filtering algorithm in terms of detecting micro-objects is yet to be explored. The proposed plane fitting algorithm is a promising approach in addressing the existence and detection of micro objects or intermediate objects that have potential impact on the surface flow behaviour. This algorithm has been applied to two study areas and more insight is needed into the performance of this algorithm in more complex and large topographic areas.

Chapter 5

Object classification

5.1 Introduction

In the previous chapter, the filtering algorithm separates the LiDAR data into ground (i.e. terrain) and non-ground (i.e. objects) points. This chapter presents two algorithms working on the raw LiDAR data for efficient classification of objects into two classes: buildings and trees. The first algorithm uses LiDAR elevation data and aerial images while the second algorithm only uses LiDAR elevation data.

5.2 Proposed methods for object classification

The main motivation for building and tree classification is to produce a DSM with the buildings attached to it. As already described in Chapter 2, a variety of techniques have been proposed by researchers using different data sources. The use of LiDAR data alone or in combination with other ancillary data such as aerial images and topographic maps has been a popular choice for the task of building and tree classification in recent years. Most, if not all, of the presented works are targeted at 3D city modelling. The proposed algorithms do not use the building topographic maps as input mainly for the following reasons:

- The building topographic maps usually represent only the floor plan of buildings
- Many cities do not have the updated topographic maps.
- Automated building classification can help update the building maps

The task of detecting buildings and trees on a digital surface model provides important information on the locations, shapes and sizes of the objects in order to understand their influence on the surface run-off behaviour. While modelling the overland flow caused by excessive rainfall, the accurate delineation of the surface pathways in a given topography is important for guiding the floodwater to further downstream. These surface pathways also collect water from the surrounding topography and convey them down to the street network. The accurate delineation of surface pathways and depression ponds can be greatly influenced by the presence of solid structures, e.g. buildings. On the other hand, the roofs of the buildings contribute to the direct runoff, conveying the water to the sewer system. Thus, automatic detection of buildings can facilitate the calculation of roof areas and estimate the run-off volume with higher accuracy. Unlike buildings, trees do not appear as solid objects on the DSM. During the overland flow, only the trunk of a tree interacts with flood water and the above-ground crown remains untouched by this interaction. In surface reconstruction techniques from LiDAR point data -either in the form of triangulation or rasterization - trees with crowns will be represented as solid objects. Thus, interpolated tree objects will block much of the terrain which will otherwise in reality remain free around the trunk. Although the leaves of trees serve as interceptors during rainfall events and impact on the rainfall-runoff process, this study does not consider this impact but provides the database for the tree objects in case a flood modeller might be interested to use it.

Before performing any classification technique, the filtered object points are grouped into a number of clusters by applying a region-growing clustering technique. Afterwards, each cluster is evaluated automatically by assigning a class label. The details of this clustering technique will be described in Section 5.3 of this chapter. In this context, two algorithms are proposed to classify buildings and trees by using LiDAR height data and aerial photography. In the first algorithm, the concept of

‘pseudo-gridding’ is introduced. The assumption behind this algorithm is to break an object cluster into relatively smaller virtual grids. Height texture (variation) is analysed for each grid and a class label (either building or tree) is assigned to each of these grids. This region-growing clustering technique is the prerequisite for the assignment of class labels of both the algorithms.

In the second algorithm, an unsupervised segmentation technique is designed to apply to each object cluster followed by surface planarity analysis. This segmentation technique is based on the work of Roggero [104]. Each segmented patch within an object cluster is further investigated by looking at the criterion of surface planarity i.e., if a surface is planar or non-planar. This algorithm is known as ‘planar surface analysis’.

5.3 Object clustering

Clustering is a technique used to sort a set of observations into subsets so that observations in the same set are similar (Enclust [143]). After the application of a filtering algorithm, the LiDAR point data are separated into ground and non-ground/object points. The object points are mainly buildings and trees. The non-ground points, i.e. the objects, appear as clusters in the feature space. An object consists of many points ranging from one to several hundred. The laser pulses returning from a street lamp post might result in one object with one point while a rooftop of a moderately large building could produce several hundred points. Figure 5.1 shows extracted object points and an enlarged view of an object denoted by the arrow. This object consists of several hundred points. The human visual system can interpret the arrangement of the object points as clusters or even label them as a building or a tree cluster. An automatic computer-based classification needs to be informed of the number of object clusters present in a scene.

In this study, a region-growing clustering technique is presented in order to segment the objects into meaningful clusters. The segmentation method is controlled by a threshold value calculated from the Euclidean distance. The region-growing technique starts with the selection of a seed point. This seed point is randomly

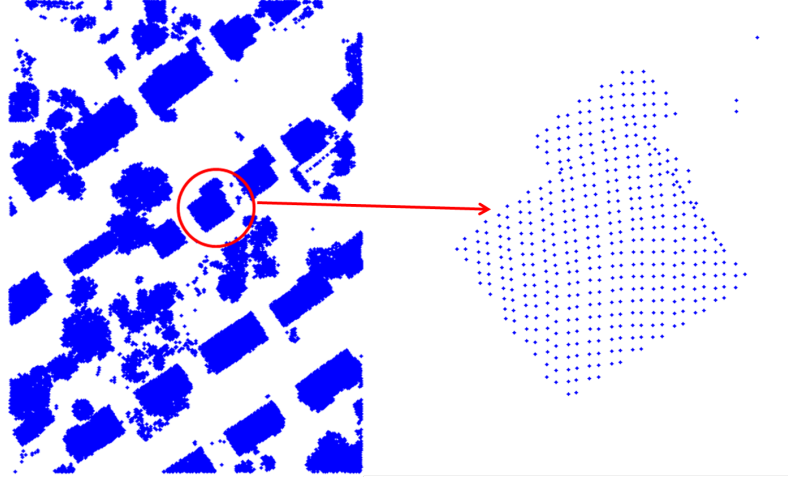


Figure 5.1: Extracted objects appearing as clusters (left) and enlarged view of an object (right).

selected from a given set of object points. A circular neighborhood is imagined around the seed point. The distances between the seed point and the points within the neighborhood are calculated by considering Euclidean distance metric. A user-defined threshold is set to sort out the points that will be merged with the seed point to grow the region from a single point. Each of the merged points starts searching for the neighborhood and selects the candidate points to be merged with that region. When there exist no more new points in the neighborhood, the region growing process terminates. The distance $d_i \{i = 1, 2, \dots, 5\}$ is calculated between

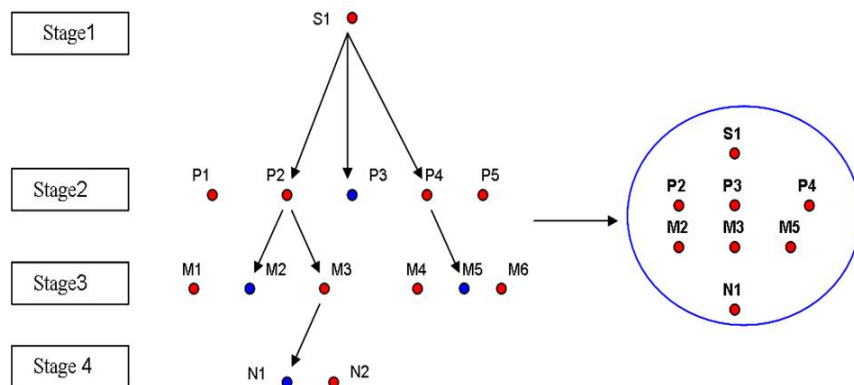


Figure 5.2: Region-growing clustering algorithm. The blue points are the algorithm termination points.

the pairs $(S_1, P_i) \{i = 1, 2, \dots, 5\}$. Any point having the distance d_i smaller than a user-defined distance threshold d_t ($d_i < d_t$) is merged with the seed point. Thus points P_2 , P_3 and P_4 meet the criterion and are merged with S_1 . The points P_1 and P_5 are disregarded at this stage and left out to be considered for the next seed point. In stage 2, a circular neighbourhood is imagined for each of P_2 , P_3 and P_4 . The point P_2 repeats the procedure described in stage 1 and finds two points M_2 and M_3 to be merged, while point P_4 finds only point M_5 to be merged. However, at this stage the point P_3 does not find any further point to merge with and the point searching procedure is terminated. In stage 3, points M_2 , M_3 and M_5 start to search new neighbourhood points and only M_3 can include a point N_1 leaving M_2 and M_5 as terminated points. In stage 4, point N_1 does not find any further point and the process terminated. Thus, the region-growing clustering technique described through stage 1 to stage 4 creates a subset $\{S_1, P_2, P_3, P_4, M_2, M_3, M_5, N_1\}$ out of a set of non-ground points. The new seed point is chosen randomly out of rest of the data points and the region growing process continues.

5.4 Building and tree classification

The object classification algorithm is concerned with assigning a class label to an object cluster. Each segmented cluster might represent either a building or a tree. A relatively larger cluster may also contain both a building and a tree when they are attached together in reality. The classification algorithms used here are,

1. Pseudo-gridding approach
2. Planar surface analysis

5.4.1 Pseudo-gridding

Cho et al. [28] use the term ‘pseudo-grid’ while working on a 3D building reconstruction. They define a square grid taking into account the LiDAR density sampling where each pseudo-grid virtually stores the LiDAR point data in grid form. Their intention is to perform pseudo-grid-based building extraction by applying a local

maximum filter. Han et al. [56] use the term ‘virtual grid’ while describing an efficient PC cluster method to handle large volumes of airborne LiDAR data. The prefix ‘pseudo’ originating from the Greek word ‘pseudein’ means ‘lying’ or ‘false’. Thus the term ‘pseudo-gridding’ means to draw a ‘virtual grid’ or ‘false grid’ within an object element to perform further classification in a smaller domain. In this study, pseudo-gridding is an approach used to break a non-ground object into small rectangular grids (Figure 5.3). In Figure 5.3(a), LiDAR points of a building object is overlaid on the image. Figure 5.3(b) illustrates the subdivision of an object cluster into rectangular blocks. A non-ground object cluster contains irregularly distributed 3D points captured by a LiDAR sensor on board of an aircraft. Thus a LiDAR sensor enables the capturing of the top-view of an object with elevation information. The choice of a suitable classifier can analyse the surface properties of an object before assigning any class label to them. The hypotheses of a suitable classifier would be as follows:

1. Buildings may have constant height profile (flat roofs) or linear change in height profile (gable roofs).
2. Trees have irregular height profile.

In support of the above mentioned hypotheses, the following phenomena can be described:

1. A height threshold could be set to distinguish buildings and trees on a neighbourhood basis.
2. The concept of pseudo-gridding would provide a pre-defined square/rectangular neighbourhood for analysing object surface properties (i.e., height).
3. Many rooftops might have an irregular surface due to the presence of chimney, solar panel or water tank. A building roof with a chimney might exhibit two types of class labels i.e., buildings and trees. The square grid containing the chimney might be classified as a ‘tree’ because of a large height difference whereas the other grids containing the homogeneous parts of a roof would probably be classified as a ‘building’.

4. The situation might become complex when trees and buildings are attached together representing a single object. The implementation of an optimal square grid would capture the properties of both types of surfaces.

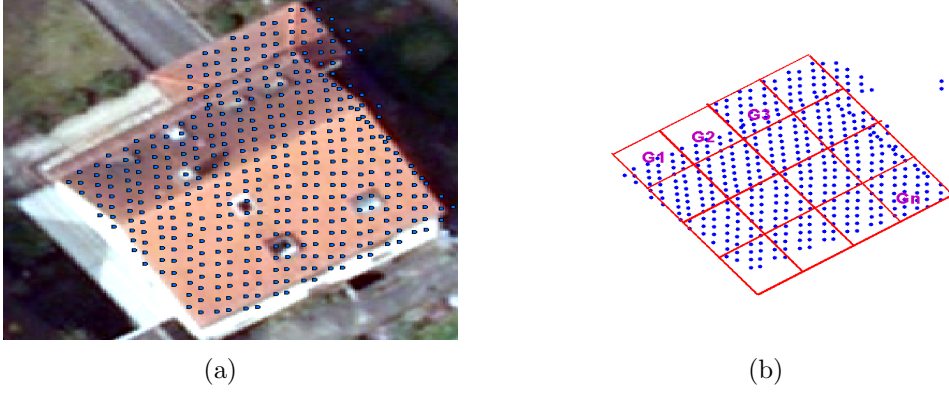


Figure 5.3: Concept of pseudo-gridding.

5.4.1.1 Basic algorithm

The pseudo-gridding algorithm starts with the selection of an object cluster from a pool of objects. A rectangle is drawn through the top-left and bottom-right (x,y) coordinates of the selected object. The rectangle is subdivided into a number of square grids (G1, G2, ..., Gn) having the length of the sides between 1m and 1.5m (Figure 5.3)(b). The height texture (variation), i.e. the minimum height (h_{\min}) and the maximum height (h_{\max}) for each grid is computed for all the grids within an object cluster. A user-defined height threshold (Δh) is set and any grid having $h_{\max} - h_{\min} < \Delta h$ is categorised as a building. Otherwise, the grid will be categorised as a tree. In this way, the algorithm keeps checking the height texture for all the grids within a selected object cluster. Then the algorithm moves to the next object cluster and repeats the same procedure of assigning a class label. Figure 5.4 shows the implementation of the pseudo-gridding by flowchart.

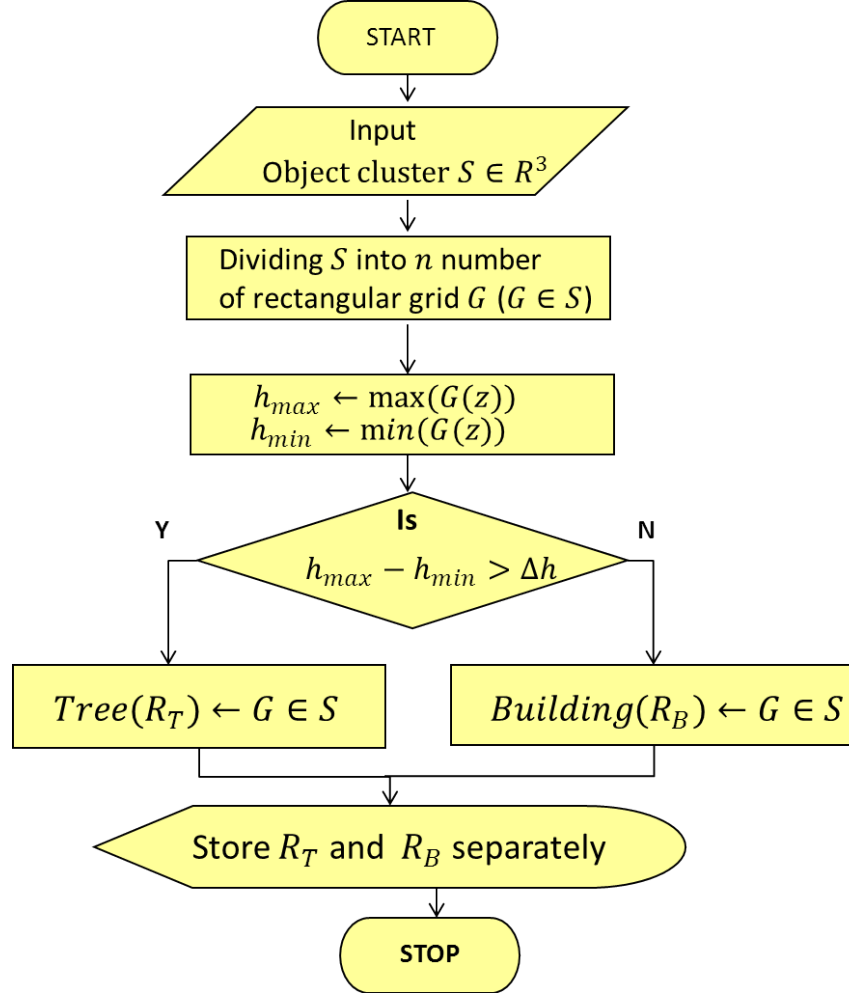


Figure 5.4: Flowchart of pseudo-gridding algorithm.

5.4.1.2 Spectral information integration

Spectral information integration (SII) is a technique of mapping the spectral value of an object from image pixel to LiDAR point data (Aktaruzzaman and Schmitt [4]). The pseudo-gridding approach does not produce an error-free classified map. There are many exceptional cases prevailing in the real-world scenario that are difficult to justify with the simple assumptions described in Section 5.4.1. For example, many buildings have very steep roof planes while some trees have flat surfaces which cause the pseudo-gridding algorithm to perform poorly. Also, the grid adjustment

technique is not sensitive enough to repair the misclassification when there are points with sharp discontinuities at the edges of buildings and trees.

Spectral information contained in an aerial image can provide useful information about the surface of an object. The aerial image usually comes with three colour channels: Red, Green and Blue. Generally, an image pixel featuring a tree shows a dominant green value. But there are also exceptions, such as when the tree has red leaves or the aerial image is taken during leave-off condition. Similarly, as a general rule, a building with a coloured roof shows a dominant red or blue value. In fact, classification based solely on spectral information may lead to confusion, as in the real-world scenario, many objects have similar colours. In this study a colour index is computed followed by a user-defined threshold value in order to distinguish a point as building or tree. The colour index (CI) is calculated by the following formula,

$$CI = (green/red + green + blue) \quad (5.1)$$

The spectral information integration (SII) works on an object cluster in cases where it contains two types of classified points within it. For example, an object cluster is classified as two types of classification: building (red) and tree (blue) with red points being in the majority (Figure 5.5(a)). SII technique checks only the minor group of points to fix them in order to save computational time and reassign the new classification (Figure 5.5(b)).

5.4.1.3 Results and discussions

In this study, two different datasets are used: Alcatraz dataset and Casimirring dataset. This is to remind that each dataset contains only object points. The ground points are filtered out by applying an appropriate filtering algorithm, which has been discussed in Chapter 4. The Alcatraz and the Casimirring datasets are termed as D1 and D2 respectively. D1 dataset has 53,729 object points and the clustering algorithm (discussed in Section 5.3) produces 210 object clusters from the dataset. Conversely, the D2 dataset has 209,433 object points and the clustering algorithm produces 970 object clusters. The scene complexity and size of both the study areas differ significantly from one another. The Alcatraz study site is relatively

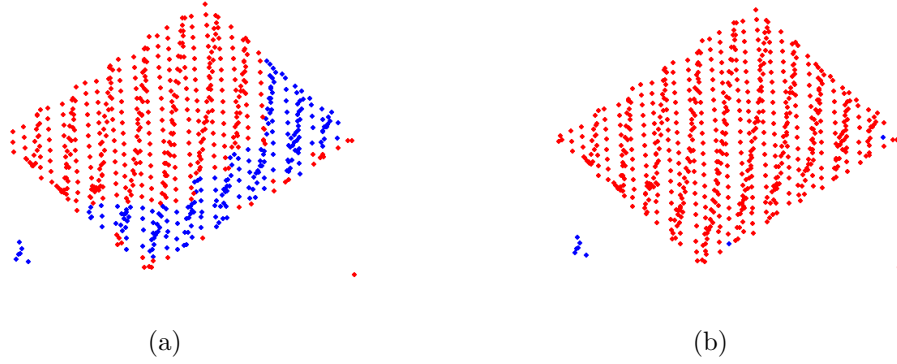


Figure 5.5: Spectral information integration (SII) technique. A building object with misclassified points i.e., the blue points (a). SII technique fixes the misclassified points (b).

small and has homogeneous building structures and few trees (Figure 5.6(a)). The Casimirring site is relatively large and features a variety of buildings with rough roof surfaces. This site also has many trees (Figure 5.7(a)). The pseudo-gridding

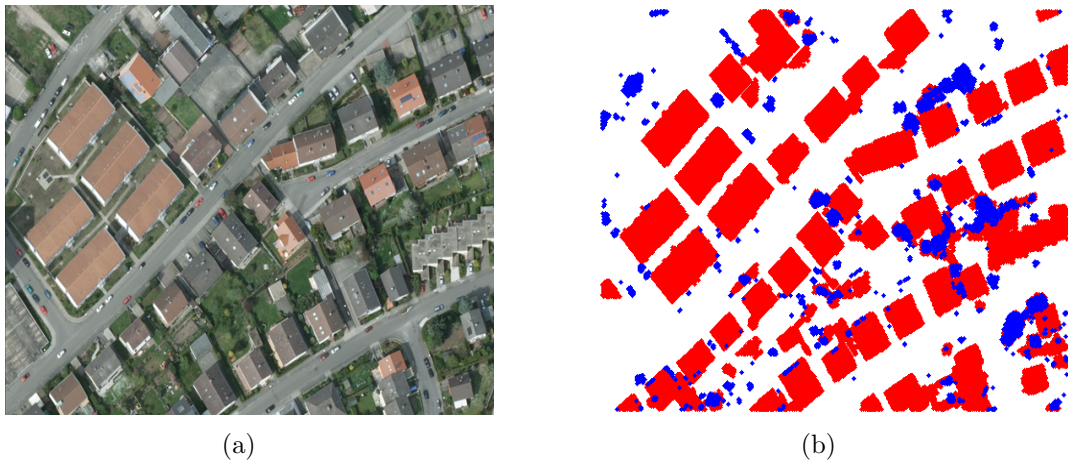


Figure 5.6: Alcatraz dataset. Aerial image of the study area at Alcatraz (244 m x 177 m) (a). Classified buildings (red) and trees (blue) with pseudo-gridding algorithm (b).

algorithm is applied to both the datasets D1 and D2, and the classified map is presented in Figure 5.6(b) and in Figure 5.7(b) respectively. In Figure 5.6(b), a close visual inspection into the classified D1 dataset reveals that some building

points on the roofs are classified as trees because of the presence of dormer window. Some tree points are also classified as building points because of the partly smooth leaf surfaces. In order to assess the accuracy of the classified maps, an error matrix approach is adopted for both the datasets. Table 5.1 shows the computed error matrix for the Alcatraz area. The overall accuracy computed from the error matrix is reported to be 95%. Building objects have errors of omission of 3.75% and errors of commission of 2.53% while tree objects have errors of omission of 10.00% and errors of commission of 14.28%. In Figure 5.7(b), a close view into the classified D2

Classified map	Reference map		
		Building	Tree
	Building	77	2
	Tree	3	18

Table 5.1: Error matrix of D1 dataset for pseudo-gridding algorithm.

dataset shows that many buildings are classified as trees because of the presence of chimneys and trees overhanging on the buildings. Table 5.2 shows the computed error matrix for the Casimirring area. The overall accuracy computed from the error matrix is reported to be 86.5%. Building objects have errors of omission of 8.77% and errors of commission of 19.76% while tree objects have errors of omission of 14.5% and errors of commission of 12.65%.

Classified map	Reference map		
		Building	Tree
	Building	104	17
	Tree	10	69

Table 5.2: Error matrix of D2 dataset for pseudo-gridding algorithm.

The overall accuracy computed for both the areas using psudo-gridddding approach shows quiet contrasting results. While the computed overall accuracy (95%) is satisfactory for Alcatraz area, that of Casimirring area shows realtively lower accuracy (< 90%). It can be said that, for a complex urban scene (i.e.,Casimirring area) the performance of pseudo-gridding algorithm is not satisfactory and it requires more sophisticated approach for identifying feature description.

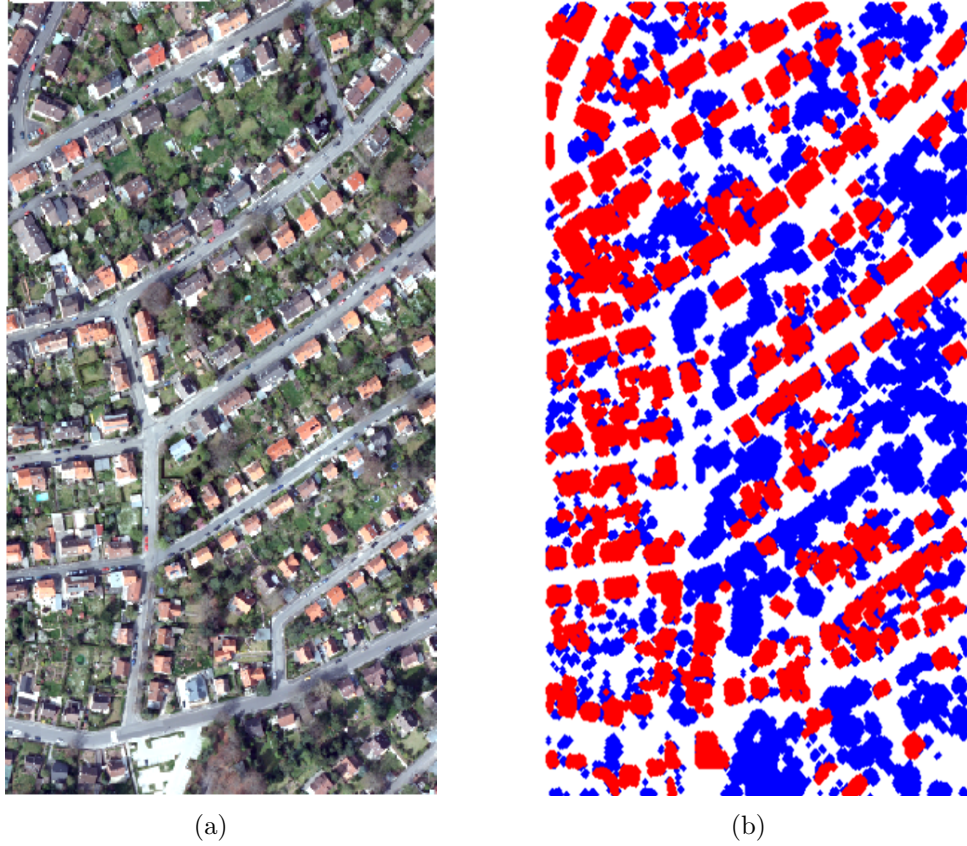


Figure 5.7: Casimirring dataset. Aerial image of relatively larger study area at Casimirring (300 m x 516 m) (a). Classified buildings (red) and trees (blue) with pseudo-gridding algorithm (b).

5.4.2 Planar surface analysis

The planar surface analysis algorithm has two parts: i) segmentation and ii) determination of surface planarity. The segmentation process is further divided into two stages: i) region-growing segmentation and ii) separation of roof planes. Data mining, which is a branch of computer science, is a technique to extract meaningful information, shapes and patterns from a large data set which is apparently unstructured. The act of information extraction is achieved by employing mainly classical statistics, e.g., clustering and regression analysis as well as new-generation statistics such as decision tree and rule-based classifier (Endata [144]). In this study, a data segmentation approach is implemented to divide an object cluster into sub-objects.

Later each of the sub-object is classified into either buildings or trees following the application of rule-based classifiers. Each of the segmented objects was investigated to seek the hidden pattern, e.g., surface planarity in 3D points. A surface is said to be a ‘planar surface’ if it has a flat two-dimensional space and a normal vector perpendicular to it. In computer vision, segmentation is the process of partitioning a digital image into smaller units containing similar pixels. This partitioning is useful for better handling, and extracting features from those pixel units. In the context of 3D point clouds, segmentation refers to the subdivision of a set of 3D points into spatially homogeneous groups having similar surface properties. Airborne LiDAR sensors capture the planimetric information of the topographic objects with elevation data attached to it, and provide unstructured and noisy 3D data for further processing. These high-density 3D point data are utilized in many fields of research ranging from high resolution digital elevation model generation to 3D city models construction (Vosselman et al. [127]). The automatic processing of large volumes of point clouds is a challenging task and requires implementation of robust algorithms. The first phase of automatic processing is the provision to apply an appropriate segmentation technique. Segmentation is also the foundation stage to perform any further feature extraction or shape recognition from 3D point clouds (Chen and Zakhor [25]; Vosselman et al. [127]). There are different types of segmentation methods depending on their applications to various problems. Wang and Shan [130] present a detailed description of various segmentation methods frequently used by both the airborne and terrestrial LiDAR communities. They categorize the segmentation methods into the following groups,

1. Edge detection method
2. Surface/region growing method
3. Scan line method
4. Clustering method
5. Graph partitioning method

Edges contain valuable information about shape and size of the objects in an image. The segmentation technique based on edge detection can only be applied to images.

Thus the conversion of LiDAR 3D point clouds to 2.5D range data is the precondition before applying this segmentation technique. The choice of a suitable edge detector (e.g. canny, sobel etc.) with an appropriate threshold influences the segmentation process. But this edge-based segmentation performs poorly in presence of multi-layer objects such as tree branches overhanging the roofs (Wang and Shan [130]).

Surface-growing segmentation technique begins with the selection of a seed point and continues by growing the seed point into a region by aggregating the neighbouring points. The aggregation criteria depend on the similarity measures, such as slope, curvature and proximity. LiDAR communities widely use this segmentation method (Wang and Shan [130]). This method is also known as region-growing technique. The scan line method is mainly applicable for range images. This segmentation method splits the image into scan lines along the direction of rows or columns. Later, each scan line is further segmented and finally the segmented parts are merged depending on some criteria similar to region-growing method.

Cluster-based segmentation methods take into account the feature vectors consisting of geometric and radiometric descriptors which are associated with a single point data (Sapkota [110]; Wang and Shan [130]). A clustering technique, such as k-means or fuzzy-clustering is used for segmenting LiDAR data in feature space. This method performs equally well on point cloud, grid/image and TIN. Graph partitioning methods are based on the idea that points in the same segment are more closely connected. A neighbourhood graph $G(V, E)$ is constructed on the point clouds where V represents a set of nodes and E represents a set of edges. The segmentation is implemented by finding an optimal cut between two segments (Wang and Shan [130]).

However, there is another type of segmentation method that combines more than one method to detect a homogeneous segment. This type of segmentation is known as hybrid method (Sapkota [110]). Roggero [104] describes a segmentation method that works by combining hierarchic region-growing and computing geometric descriptors to segment 3D noisy point data. Dorninger and Nothegger [37] describe a segmentation method applied to predefined building point data in order to separate the roof planes by combining a clustering technique and a Fast Minimum Covariant Determinant (FMCD) approach. Oude Elberink and Vosselman [40] present

a surface-growing segmentation technique with additional incorporation of Hough transformation to select seed points. In this study the hybrid segmentation method described by Roggero [104] is applied. The details of this segmentation are described in the following section. The region-growing segmentation technique subdivides an object cluster into meaningful regions based on the information of proximity and similarity in geometric descriptors.

5.4.2.1 Region-growing segmentation with static moment calculation

The region-growing segmentation is based on the idea that the neighbourhood of a point can be described by considering not only Euclidean distance but also by considering physical or geometrical properties (Roggero [104]). Roggero [104] describes three geometric descriptors, namely static moment, curvature and junction. These descriptors, when calculated for a single point p_i , are able to detect discontinuities in the neighbourhood and can thus provide better segmentation.

In the field of solid mechanics, when a scalar quantity such as the area or mass of an object is multiplied by the perpendicular distance from a point connected with that object (such as the centroid of the area or the centre of mass) to a reference axis, the result of the multiplication is known as the static moment. Sometimes the static moment is also known as the first moment of area/mass. Let A be the area of an object with any arbitrary shape. Area A is further subdivided into n small element areas (dA_i). If x_i and y_i are the distances for each dA_i from the 2D coordinate $x - y$ axis respectively, then the first moment of area in the x direction is:

$$M_x = A\bar{y} = \sum_{i=1}^n y_i dA_i \quad (5.2)$$

And the first order of moment in the y direction is:

$$M_y = A\bar{x} = \sum_{i=1}^n x_i dA_i \quad (5.3)$$

In the context of a subset of a point cloud, each point can be assumed as a discrete point with a unique mass attached to it. The distance of each point can be calculated

from the centroid of the subset points. From the above two equations it can be seen that first order moment has larger values for the element areas lying on or near the boundaries. Similarly, in a set of points the maximum static moment can be observed for the points lying on the edges. In Roggero [104], for a given 3D point data, the static moments for each point against each reference axis can be defined as:

$$S_x = \sum m_i(y_i + z_i) \quad (5.4)$$

$$S_y = \sum m_i(z_i + x_i) \quad (5.5)$$

$$S_z = \sum m_i(x_i + y_i) \quad (5.6)$$

Thus a single point data has three static moments with reference to x , y and z axes. The value of m_i is assigned to 1 considering each point having unit mass. The total static moment for a single point data can be computed as:

$$S_t = |S_x * S_y * S_z| \quad (5.7)$$

To calculate the total static moment of any randomly extracted point, a rectangular neighbourhood is defined around a point of interest. The basic steps of the region-growing segmentation can be outlined in Figure 5.8.

The above algorithm partitions an object cluster into a number of subgroups. The 3D surface information of an object acquired by the LiDAR sensor exhibits different levels of discontinuity in the point data. These discontinuities are the structural information of an object of interest. A building roof shows two types of discontinuity: i) crisp-edge discontinuity at the roof edges and ii) soft-edge discontinuity at the junctions of the roof planes. Wang and Shan [130] describe these types of discontinuities caused by jump edge and crease edge. In Figure 5.9(a), LiDAR data are overlaid on a building with protruded parts. Region-growing segmentation subdivides the building surface into nine spatially homogeneous regions. The protruded parts are separated from the main roof because of the presence of crisp-edges while the two roof planes are still attached together because of the soft-edge at their junction (Figure 5.9(b)).

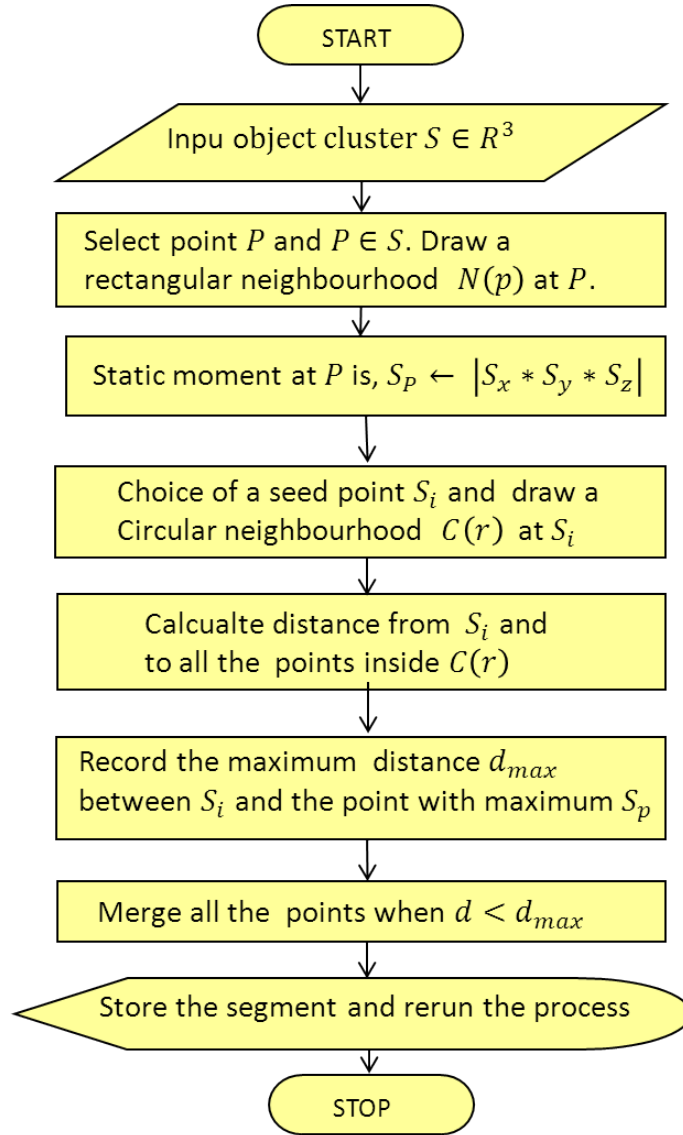


Figure 5.8: Flowchart of the region-growing segmentation.

Another example of a relatively complex case with connected buildings and trees is presented in Figure 5.10. A subset is taken from the Casimirring study area where two buildings are connected by trees and bushes (Figure 5.10(a)). The LiDAR data capture the surface of the objects in the scene (Figure 5.10(b)). Region-growing segmentation splits the object cluster into twenty-six meaningful homogeneous segments (Figure 5.10(c)). The segmented parts in Figure 5.10(c) are classified into

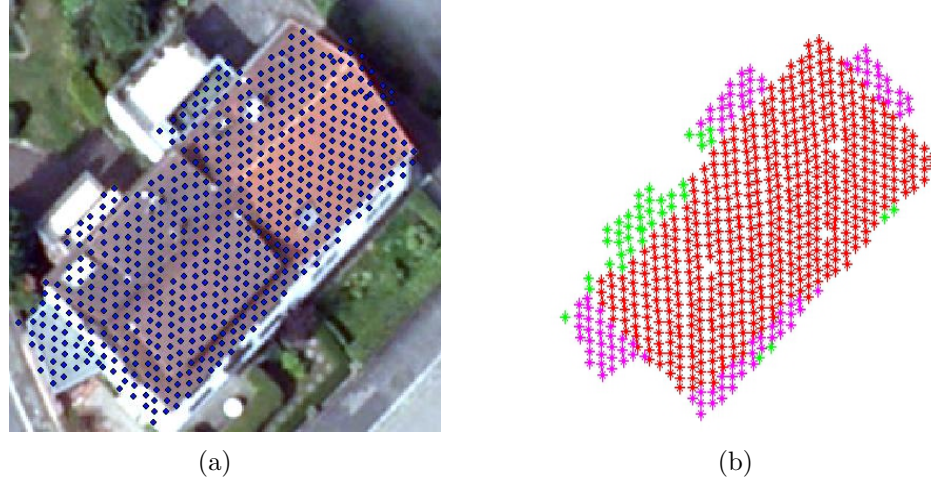


Figure 5.9: LiDAR points of a building object overlaid on the aerial image (a). Region-growing segmentation algorithm subdivides the point clouds into 11 regions (b).

two types, building (red) and tree (blue), by applying the surface planarity criterion (Figure 5.10(d)). The details of determination of surface planarity are presented in the following subsection.

5.4.2.2 Identification of planar surface

Planar surface analysis is a method based on the principal component analysis (PCA) to identify planar regions in 3D point cloud data. PCA is a mathematical technique to reduce the number of variables in a dataset. Some of the variables in a dataset may be correlated, meaning they have similar statistical properties (e.g., variance) while the other variables have less correlation or are totally uncorrelated with each other. PCA attempts to find the correlated variables and brand them as ‘redundant variables’ on the assumption that the correlated variables can be replaced by an imaginary variable i.e., a principal component. Thus, PCA technique classifies a set of variables into correlated and uncorrelated variables and helps to reduce higher-dimension data into lower-dimension data to explore the hidden pattern in a dataset.

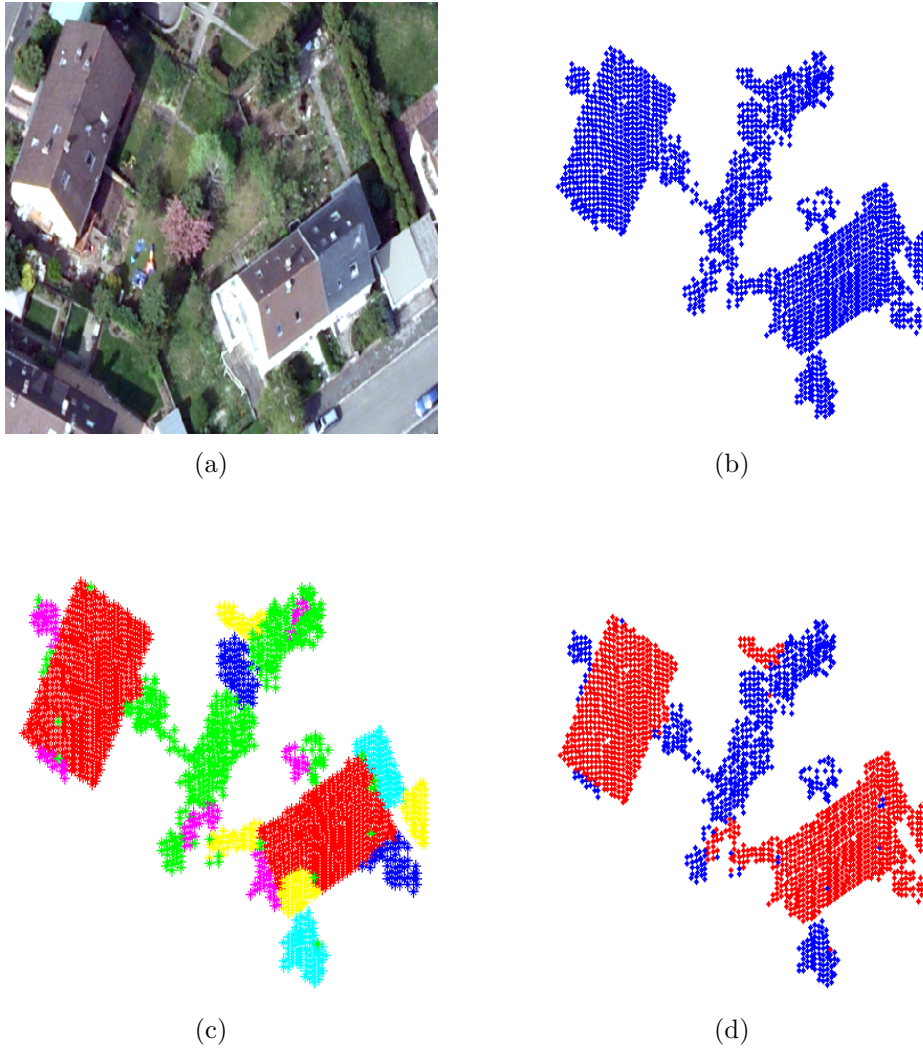


Figure 5.10: From point cloud to classified object.

A principal component analysis of a given set of points in 3D point cloud shows the direction of mutually orthogonal vectors (eigenvectors) and their relative strength (eigenvalues) (Shan and Sampath [116]). If a set of points has two dominant eigenvalues and the third value is nearly zero, those points are said to be on a plane. The nature and magnitude of eigenvalues and eigenvectors can be computed from a covariance matrix. In statistics, variance is a measure to determine the dispersion or spread of a one-dimensional dataset, i.e. a dataset with a single variable. For a dataset having more than one variable, sometimes it is important to check whether

any relationships exist among the variables. In statistical analysis, covariance is a measure that explores the meaningful relationship between two variables. If x and y are two variables in a dataset representing some arbitrary physical properties, then the covariance between the variables can be calculated as

$$\text{covar}(x, y) = \frac{1}{n-1} \sum_{i=1}^n (x_i - \bar{x})(y_i - \bar{y}) \quad (5.8)$$

where, n = Number of samples in variables x and y . A set of LiDAR 3D point data has three variables, namely x (latitude), y (longitude) and elevation (z). The measurement of covariance among the variables (x , y and z) calculates the relationships between (x, y) , (y, z) and (z, x) respectively. Thus the measurement of covariance values for all the variables can be put together in a matrix known as a covariance matrix. Each element of a covariance matrix having 3×3 dimensions can be arranged as

$$CM = \begin{bmatrix} \text{covar}(x, x) & \text{covar}(x, y) & \text{covar}(x, z) \\ \text{covar}(y, x) & \text{covar}(y, y) & \text{covar}(y, z) \\ \text{covar}(z, x) & \text{covar}(z, y) & \text{covar}(z, z) \end{bmatrix} \quad (5.9)$$

Where, $\text{covar}(x, x)$, $\text{covar}(y, y)$ and $\text{covar}(z, z)$ represent the variance of x , y and z respectively. Diagonal entries of a covariance matrix are in fact the variance measures of the respective variables. If $x = \{X_1, X_2, \dots, X_p\}$ is a random vector with the mean vector $\mu = \{\mu_1, \mu_2, \dots, \mu_p\}$, then the formal definition of a covariance matrix is given by,

$$\Sigma = E[(x - \mu)(x - \mu)'] \quad (5.10)$$

Where, Σ denotes the covariance matrix. Let a set of points be denoted by X_i ($i = 1, 2, \dots, m$) and let \bar{X} be their mean vector. The covariance matrix is calculated as:

$$\Sigma_{XX} = \sum_{i=1}^m (X - \bar{X})(X - \bar{X})^T \quad (5.11)$$

Let the covariance matrix Σ_{XX} in equation 5.11 have the eigenvalues $\lambda_1, \lambda_2, \lambda_3$ and their corresponding eigenvectors Λ_1, Λ_2 and Λ_3 . The analysis of these eigenvalues and their mutual relationship reveals the inherent surface information of a set of

points partitioned by the region-growing segmentation. A surface can be planar points or scatter points. The conventional point classification takes into account three structural types, spherical, cylindrical and planar, to assign a class label to a point. Let $N(p)$ be a neighbourhood of N points with p in the centre. This neighbourhood can be formed by placing a sphere at point p with radius r . This can also be a predefined set of points resulting from segmentation or a clustering algorithm. Let CM be the covariance matrix of the neighbourhood $N(p)$ and λ_1, λ_2 and λ_3 be the eigenvalues of CM . In Keller [74], the neighbourhood $N(p)$ is a spherical shape if

$$\lambda_1 \approx \lambda_2 \approx \lambda_3 \quad (5.12)$$

$N(p)$ is a planar shape if

$$\lambda_1 \leq \lambda_2 \quad \text{and} \quad \lambda_2 \approx \lambda_3 \quad (5.13)$$

$N(p)$ is a cylindrical shape if

$$\lambda_1 \approx \lambda_2 \quad \text{and} \quad \lambda_2 \leq \lambda_3 \quad (5.14)$$

However, the scope of this study is limited to distinguish planar and scatter surfaces featuring buildings and trees respectively. Shan and Shampath [116] distinguish between planar points and breaklines by using the following relationship of the eigenvalues of a covariance matrix,

$$[\lambda_1/(\lambda_1 + \lambda_2 + \lambda_3)] < \xi \quad (5.15)$$

5.4.2.3 Training the datasets/Developing the rule-sets

In this study surface planarity is used as a measure/criterion to distinguish between buildings and trees. The simple hypothesis is that buildings have planar surfaces while trees have non-planar or scatter surfaces. Equation 5.15 as suggested by Shan and Shampath [116] is used to determine the surface planarity. However, Shan and Shampath [116] use equation 5.15 in order to separate roof planes only. The detection of trees is beyond their study scope and they test surface planarity only on the pre-classified building point data. Carlberg et al. [19] describe a set of equations

to determine whether a LiDAR point within a spherical neighbourhood is ‘planar’ or ‘scatter’. They propose three user-defined parameters, namely t_{planar} , t_{scatter1} and t_{scatter2} , in order to separate buildings and trees.

The choice of a suitable ξ (equation 5.15) depends on a number of characteristics: the types of building structures, the amount of forested areas in a study scene and the spatial distribution of trees i.e., whether a tree is attached to a building or standing alone. A suitable value of ξ is set after learning from the two datasets. Out of the two datasets, four objects from the Alcatraz dataset and six objects from the Casimirring dataset are selected. First, the ξ values for four sample objects are calculated and the results suggest that a building object has $\xi < 0.05$ while a tree object has $\xi > 0.05$. Now the ξ values for six samples objects are calculated from the Casimirring dataset. This time the results suggest that two buildings have $\xi > 0.05$, one building has $\xi < 0.05$ and two trees have $\xi > 0.05$. Table 5.3 shows the calculation of ξ values for sample objects of both the study areas. The reasons behind larger ξ values for buildings in Casimirring and relatively small in Alcatraz can be summed as follows:

1. Alcatraz dataset has relatively smooth roof surfaces i.e., clean roof surfaces without large chimneys and antennas. The degree of slope between two roof planes is also low.
2. Casimirring dataset has relatively rough roof surfaces with the presence of chimneys. The slopes between roof planes are very steep.

In order to choose a representative value of ξ that satisfies the definition of buildings at both the study areas, two possible solutions can be proposed:

1. To increase the value of ξ . But while increasing the value of ξ for classifying a rough roof surface as a building, many tree segments having less surface roughness would be classified as buildings too.
2. To subdivide the roof surface into individual planes. The region-growing segmentation algorithm (described in Section 5.4.2.1) can capture discontinuities only when there is a crisp edge. The junction line of several roof planes is a soft edge and the roof plane shows height variations smoothly.

Sample object	Alcatraz	Casimirring	Calculated ξ value	Relative value	Detected class	Reference class
1	Object1		0.008	<0.05	Building	Building
2	Object2		0.057	>0.05	Tree	Tree
3	Object3		0.046	<0.05	Building	Building
4	Object4		0.061	>0.05	Tree	Tree
5		Object5	0.085	>0.05	Tree	Tree
6		Object6	0.02	<0.05	Building	Building
7		Object7	0.066	>0.05	Tree	Building
8		Object8	0.094	>0.05	Tree	Tree
9		Object9	0.12	>0.05	Tree	Tree
10		Object10	0.072	>0.05	Tree	Building

Table 5.3: Calculation of ξ values for sample objects.

Figure 5.11 illustrates the separation of a roof surface into planes. Figure 5.11(a) shows a building object with segmented roof patches and **A** is the largest segment featuring the roof surface. Figure 5.11(b) presents an imaginary line passing through the middle of the largest roof patch **A**. The imaginary line divides **A** into **A1** and **A2**. The junction line is searched by calculating the maximum height of a segmented patch followed by sorting the neighbouring points within a threshold height limit of 1m (Figure 5.11(c)). The 2D Euclidean distances with signs are computed for all the points in the patch. The negative and positive distances are sorted out and they are assigned as two different planes (Figure 5.11(d)). The roof plane segmentation algorithm works on a test roof where the largest segmented patch contains around 200 LiDAR points. This study opts for the second solution and includes an additional module in the region-growing segmentation algorithm. This module subdivides a roof surface into two roof planes only if the roof surface is not flat. The basic steps of the algorithm are outlined in Figure 5.12.

5.4.2.4 Results and discussions

The planar surface analysis algorithm is applied to both the datasets D1 and D2. The classified results of D1 dataset look more visually impressive than the results obtained by the pseudo-gridding approach. Figure 5.13(a) again serves as a reference map for the Alcatraz area. Figure 5.13(b) shows the classified map of the

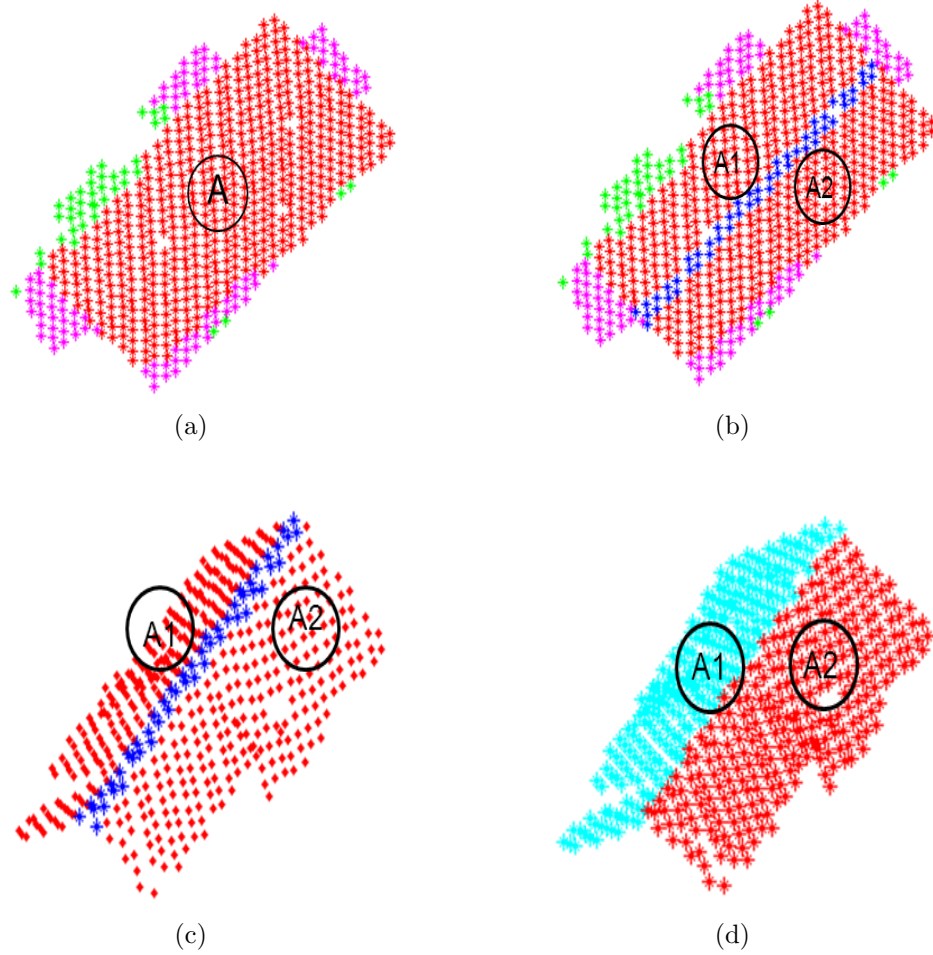


Figure 5.11: Segmentation and separation of roof planes.

Alcatraz area (D1 dataset) using planar surface analysis algorithm. The edges of the buildings and trees are smoothly classified by applying this classification technique. Almost all the object clusters show unique class label without the presence of misclassified points inside them. However, two medium-sized bushes attached to buildings are mistakenly classified as buildings. The reason behind this misclassification can be related to the fact that the bushes are pruned and having almost flat surfaces. Table 5.4 shows the computed error matrix for the Alcatraz area. The overall accuracy computed from the error matrix is reported to be 97%. Building objects have errors of omission of 2.46% and errors of commission of 5.26% while tree objects have errors of omission of 5.26% and errors of commission of 10.00%.

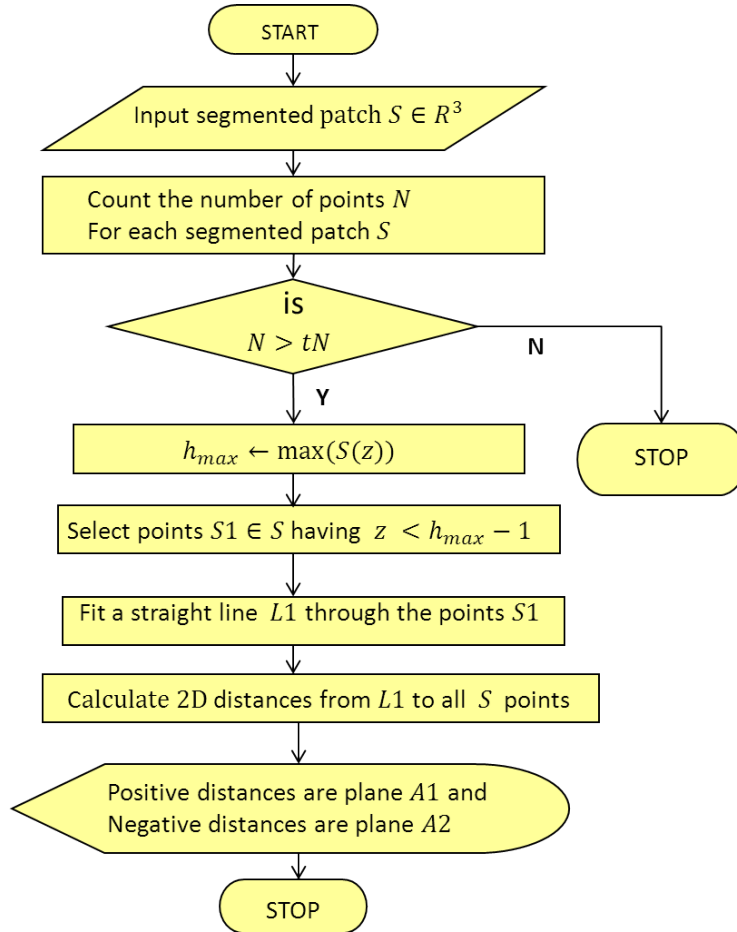


Figure 5.12: Flowchart of plane separating algorithm.

Classified map	Reference map		
		Building	Tree
	Building	79	1
	Tree	2	18

Table 5.4: Error matrix of D1 dataset for planar surface analysis.

Figure 5.14(a) presents the aerial image of the Casimirring area as a reference map and Figure 5.14(b) shows the classified map of the Casimirring dataset using planar surface analysis algorithm. Table 5.5 shows the computed error matrix for the Casimirring area. The overall accuracy computed from the error matrix is reported to be 95%. Building objects have errors of omission 4.72% and errors of commission

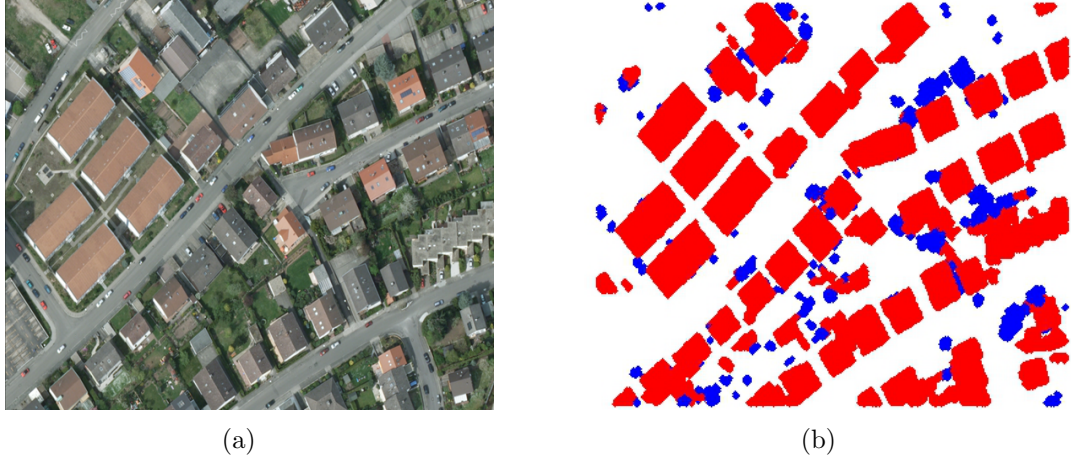


Figure 5.13: Classified map of Alcatraz dataset by applying planar surface analysis.

5.47% while tree objects have errors of omission 3.2% and errors of commission 8.0%.

The classified map produced by planar surface analysis algorithm shows much im-

Classified map	Reference map		
		Building	Tree
	Building	121	4
	Tree	6	69

Table 5.5: Error matrix of D2 dataset for planar surface analysis.

proved results compared to pseudo-gridding approach applied to Casimirring area. Out of one hundred and forty four buildings, three of them are misclassified as trees. Two buildings having roofs with four equal planar surfaces are treated as trees. Figure 5.15(a) shows a roof with four equal planes which is known as a pyramid roof. Although the planar surface algorithm can detect the buildings with four unequal planes (i.e. hipped roof), it performs poorly when treating a pyramid roof. Figure 5.15(b) presents an example of a hipped roof. When dealing with a pyramid roof, the algorithm finds it difficult to segment it into two planar surfaces as shown in Figure 5.11. Figure 5.15(c) presents a building mostly covered by trees. The algorithm detects the object cluster as a tree resulting in misclassification.

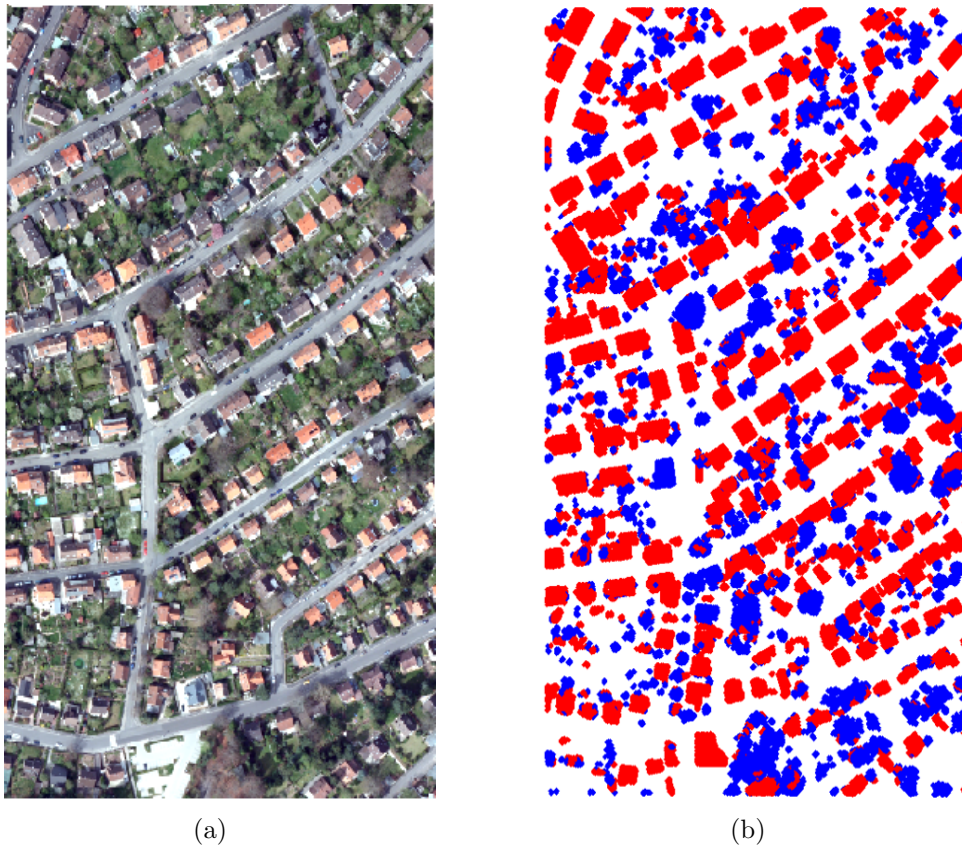


Figure 5.14: Aerial image of Casimirring study area (a) and classified map of Casimirring dataset by applying planar surface analysis (b).

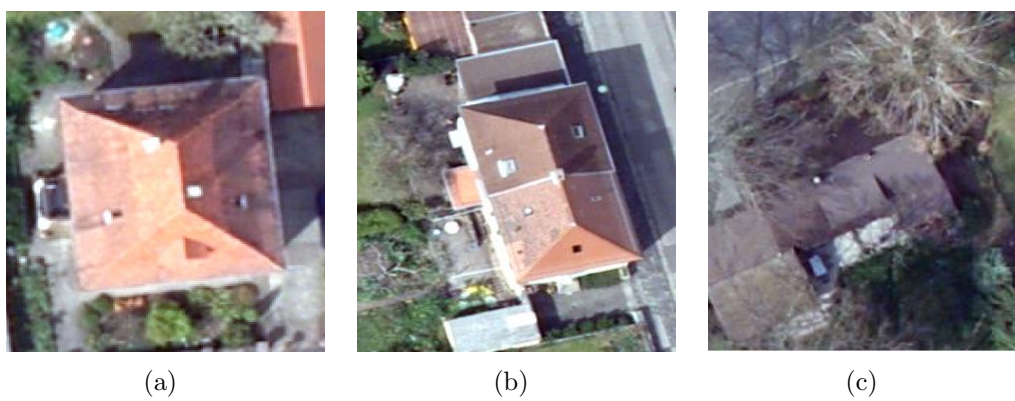


Figure 5.15: Roofs under different conditions: a pyramid roof (a), a hipped roof (b) and a roof covered by trees (c).

5.5 Detection of building outlines

After applying the classification algorithms followed by the generation of classified maps, the classified datasets need to be pruned and fine tuned in an automatic way. This section presents techniques pertaining to automatic detection of building outlines. The detection of building outlines is important in order to produce accurate polygon maps of the building objects. The approximation of building outlines is important for the following reasons:

- The building topographic maps supplied from City municipal office usually covers only the floor plan instead of the entire roof surfaces.
- The OBIA (Object-based Image Analysis) approach described in Chapter 7 requires masking out the buildings and streets in the aerial images in order to reduce spectral confusion and achieve better surface classifications. If the building polygon maps from the City municipal office were used in this case, it would cause underestimation of the building areas.

In order to delineate the boundary lines accurately, the following steps are implemented:

5.5.1 Separation of building points

The classified dataset of the Alcatraz study area using planar surface analysis algorithm is used as an example case for the reconstruction of building boundaries. Figure 5.16(a) shows the classified point dataset of Alcatraz area featuring building(red) and tree(blue). Figure 5.16(b) shows the building points only after removing the tree points.

5.5.2 Cleaning the small clusters

The classified building points contain some small object clusters which are actually bushes and other objects such as part of a boundary wall. A simple knowledge-based analysis in terms of number of points is implemented to clean out those

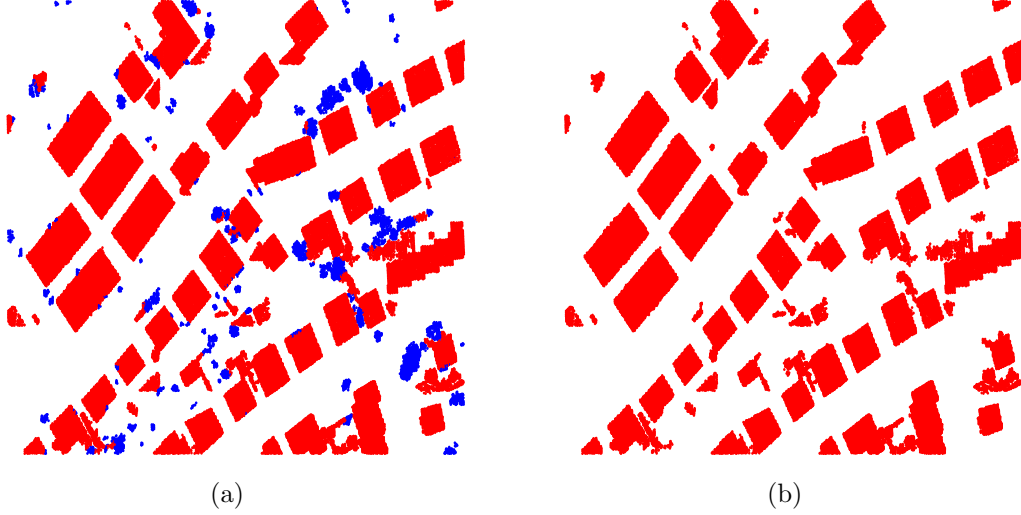


Figure 5.16: Classified dataset featuring buildings and trees (a) and only building (b).

small objects. Generally a building object should contain more than 150 points. A number of manually extracted object clusters, which are visually identified as buildings, supports this assumption. Figure 5.17 illustrates the classified building objects after removing the small object clusters.

5.5.3 Approximating boundary outlines

The delineation of a boundary outline is based on the assumption that Convex hull can roughly delineate the outline of a given point dataset. In Wang and Shan [130], the delineation of a building outline is implemented by: 1) sub-dividing a point dataset into several subsets and 2) implementation of Convex hull for each subset. In this study, a similar approach is proposed for the approximation of building outlines. The proposed approach defines a circular neighborhood N centering a point of interest p as a first step. In the second step, a Convex hull is constructed for each neighborhood point. In the third step, the position of point p is searched for whether it resides on or inside the Convex hull boundary. In case the point p resides on the boundary, it is labelled as a boundary point. Figure 5.18(a) shows the



Figure 5.17: Classified building objects only after removing small objects.

building objects (red) and the approximated building outlines (blue). Figure 5.18(b) shows only the building outlines.

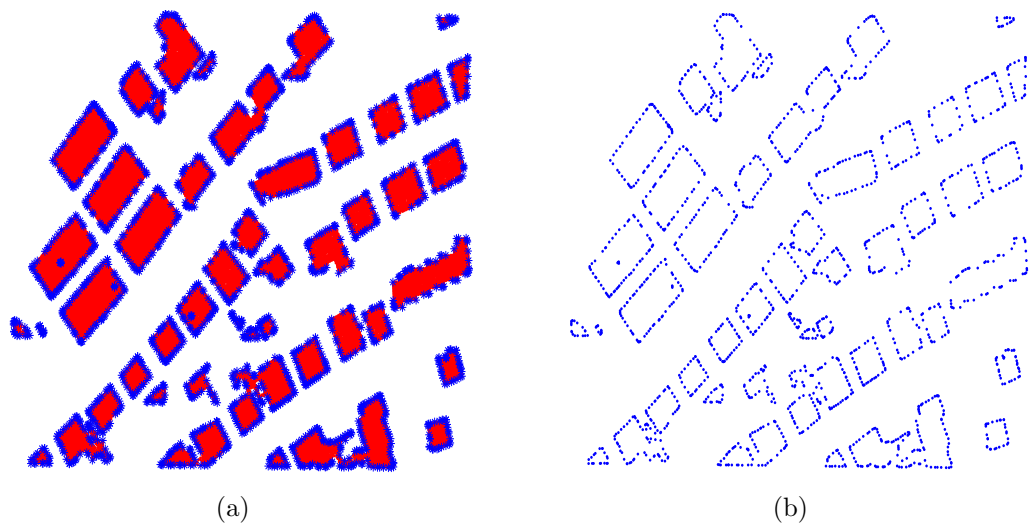


Figure 5.18: Approximation of building outline.

The approximated building outlines are overlaid on the aerial image and visual comparison is made against polygon maps supplied from the City municipal office.

Figure 5.19(a) presents a situation when a building polygon map from the City office is overlaid on the aerial image. Figure 5.19(b) shows the improved approximated building outlines.

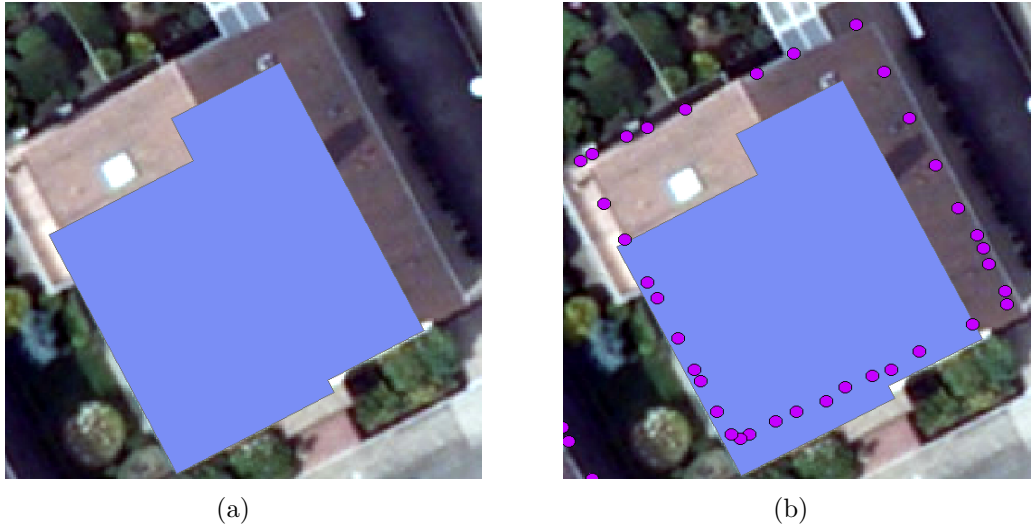


Figure 5.19: Validation of approximated building outlines.

5.6 Conclusion

A classified map featuring topographic objects such as buildings and trees is an important input for a detailed urban drainage simulation model aiming at improving the database for dual drainage modelling. An accurate and robust algorithm is needed to detect objects on the digital surface model and thereby to produce an accurate classified map. In this chapter, two algorithms are proposed: i) Pseudo-gridding and ii) Planar surface analysis to classify objects automatically in an urban scene. The pseudo-gridding algorithm takes LiDAR data and aerial images as input while the planar surface analysis algorithm takes only LiDAR data as input to produce a classified map with a higher degree of accuracy. Both the algorithms are applied to two datasets: i) Alcatraz dataset D1 and ii) Casimirring dataset D2. An error matrix is computed for each dataset against each type of algorithm. D1 dataset has overall accuracy of 95% and 97% for the pseudo-gridding and planar

surface analysis algorithms respectively. D2 dataset has overall accuracy of 86.5% and 95% for the pseudo-gridding and planar surface analysis algorithms respectively. The pseudo-gridding is an easy to implement algorithm and performs well till to the point when urban scene complexity is moderate (e.g. Alcatraz area). However, the presence of dense trees and roofs with occlusions can deteriorate the performance of pseudo-gridding algorithm which is the case with Casimirring study area. Apart from the consideration of height texture within a grid, other descriptors such as local surface fitting and measurement of point density can be incorporated into each grid during the implementation of the algorithm. Calculation of multiple descriptors will allow this algorithm to handle more complex urban scene. The planar surface analysis algorithm has proved to be efficient for both study areas. The presence of roofs with more than two planes causes the algorithm to perform poorly. The idea of implementing an additional module to detect multiple roof planes in the existing algorithm can improve the efficiency of this algorithm. The classified point clouds need to be post-processed in order to make them readily available as input to an urban drainage simulation model. Thus the building datasets can be separated from tree datasets and subsequently be attached to ground points resulting in the production of an urban DSM. Also the realistic delineation of boundary outlines provides exact estimation of the roof areas and help better model rainfall runoff process.

Chapter 6

Street extraction and 3D modelling

6.1 Introduction

This chapter presents an approach to extracting street candidate points from LiDAR point cloud and subsequently modelling it by inserting kerbs, smoothening the street surfaces, reconstructing street topology and modelling the junctions. The extraction of street candidate points is achieved by employing a point-in-polygon algorithm where 2D topographic maps of the streets are supplied as polygons. Later, the street modelling phase undergoes a variety of data processing techniques for modelling a detailed street network.

6.2 Street as an open channel

An open channel is an unconfined waterway or canal conveying fluids with an open surface and under the condition of atmospheric pressure. In most cases the fluid is water. The flow of water through an unconfined channel while exposed to the atmosphere is known as open channel flow. Open channels can be both natural, e.g. rivers, or man-made, e.g. channels to supply water for irrigation, culverts

and storm pathways (Chanson [21]). The geometric shape of a street cross-section with clear presence of kerbs and sidewalks presents a similarity with an open channel. Figure 6.1 presents an ideal cross-section of a street surface represented by a rectangular open channel.

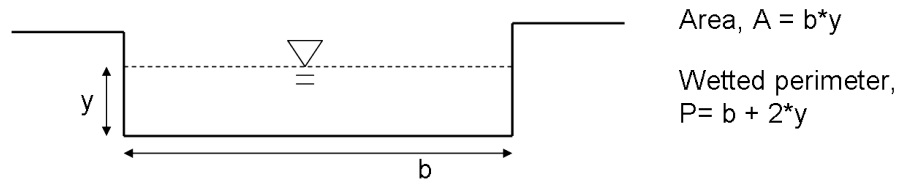


Figure 6.1: Cross-section of a rectangular open channel.

Boonya-Aroonnet et al. [17] describe the streets as ‘primary preferential paths’ where the surface flow occurs first and the water runs later into other surface ponds and storm waterways, which are the secondary preferential paths. Neelz and Pender, [94] present an experimental study illustrating the clear influence of errors in a digital terrain model on the flood flow routes. They concentrate on the modelling of overland flow by using a benchmark DEM and a LiDAR-derived DEM. The benchmark DEM is the product of Ordnance Survey, the national mapping agency of Great Britain, representing high-resolution topographic features including street cambers and kerbs. In contrast, the LiDAR-derived DEM is not sufficiently post-processed and smoothened to represent the reality. The findings of the study revealed slower flow velocity and inaccurate inundation level for the LiDAR-derived DEM compared to the benchmark DEM. A similar study has been reported by Vivienne K. Dell et al. [123].

Thus, treating streets as open channels during the modelling of overland flow can significantly improve the accuracy of the modelled flow velocity and flood inundation level. This study attempts to reconstruct a single-layer street network by combining LiDAR data, topographic map and aerial image. The main motivation is to generate a realistic street network with detailed modelling of the street elements such as pavements, kerbs, traffic lanes and intersections. Special attention is paid to modelling each street element in such a way that it retains hydraulic properties

that eventually make the street surface operate like an open channel in case of heavy rainfall events and sewer surcharge.

6.3 Data types and sources

Three types of data sources are used for the modelling of single-layer street networks. They are: 1) 2D topographic map of the streets; 2) LiDAR data; and 3) aerial images. Figure 6.2 presents two different datasets, namely street topographic map (a) and aerial image (b). The use of the first two data sources is responsible for

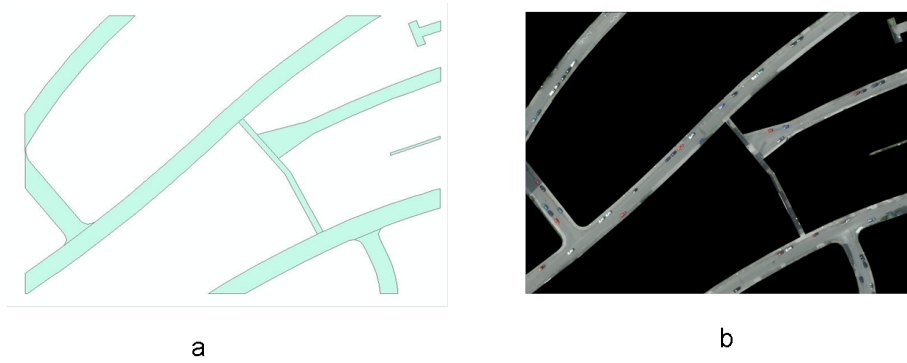


Figure 6.2: 2D topographic map (a) and aerial photograph with clipped street network (b) of the study site.

extracting street networks and construction of street connectivity. The last data type, i.e. the aerial images contributes meaningful information to the delineation of street kerbs. However, a pre-processing step is necessary before using the images for street modelling purposes. An image clipping technique is applied to the aerial images in order to extract the region of interests for further analysis. The 2D street topographic maps act as clip elements for this purpose.

6.4 Methodology

The current state-of-the-art 3D street modelling combines the topographic maps and LiDAR data in order to overcome the shortcomings of each individual data

source. The proposed street modelling methodology has some similarities with the work of Chen and Lo [26] and Oude Elberink and Vosselman [41] in terms of street point extraction and assignment of height to street surfaces. However, the automatic detection of kerbs and modelling of junctions targeted at characterizing hydraulic properties of the streets are the contributions embedded in this street modelling methodology. Figure 6.3 shows the workflow of 3D street modelling. The proposed street extraction and modelling methodology can be split into six modules as follows:

- Street candidate points extraction by point-in-polygon method
- Street connectivity (topology) construction
- Detection of centrelines
- Delineation of kerb line
- Street surface reconstruction
- Modelling of the junction.

The details of each module are discussed sequentially from Section 6.5 to 6.10. Thus, the methodology described in this study is independent of any specific location and can be applied to any study area where a single-layer street network exists within an urban scene.

6.5 Street points extraction

6.5.1 Point-in-polygon algorithm

The Point-in-polygon (PIP) is an algorithm that checks whether a point resides on, outside or inside of a given polygon (Haines [55]). The PIP algorithm is extensively used in the field of computational geometry. This algorithm implements an easy strategy to determine the position of a point in reference to a given polygon. A straight line is drawn from infinity to the point of interest and extended in order to calculate how many times it intersects the edges of a given polygon. If the

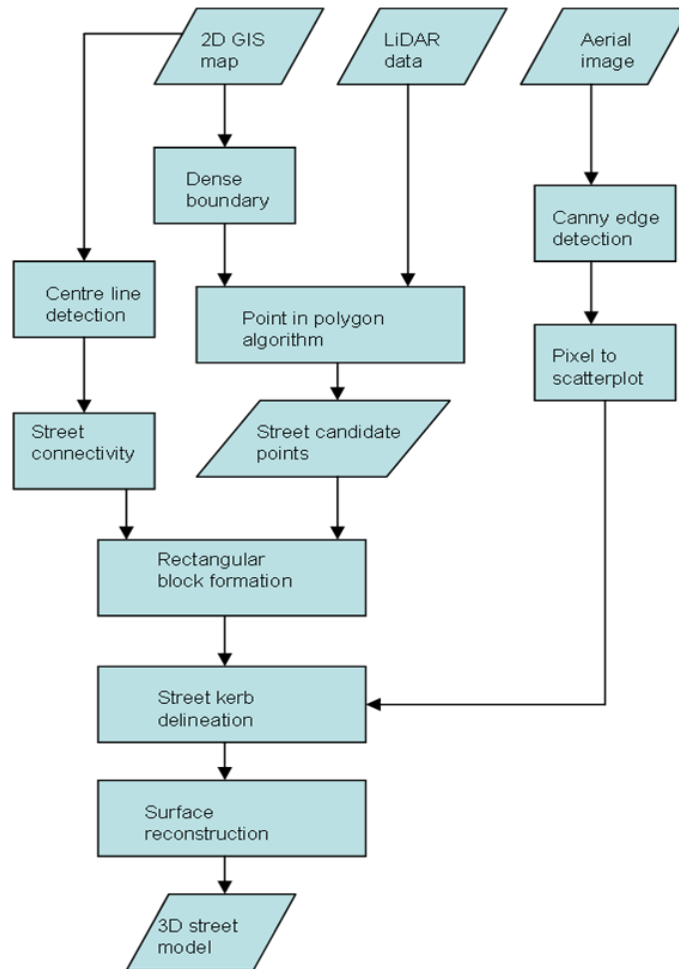


Figure 6.3: Workflow of 3D street network modelling.

number of intersections is an even number, the point resides outside the polygon ([145]). Otherwise, the point is inside the polygon when the count is an odd number. Figure 6.4 illustrates the implementation of the PIP algorithm. The randomly generated scattered points are separated by the polygon $P_1P_2P_3P_4P_5$. The points marked as ‘+’ denote the points lying inside the polygon whereas the points marked as ‘o’ reside either on the boundary or outside the polygon. The PIP algorithm finds its applicability for the extraction of street candidate points bounded by 2D street topographic maps. A topographic map featuring a street network consists of many individual street segments. Each of the street segments acts as an input boundary for the implementation of the PIP algorithm. The collective contribution of all the

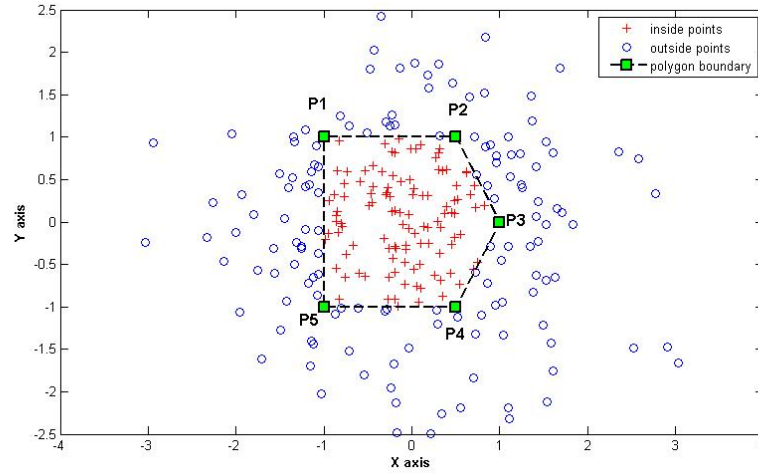


Figure 6.4: Implementation of the Point-in-polygon (PIP) algorithm.

street segments results in the complete extraction of a given street network from the LiDAR point cloud. The entire process of importing polygon boundaries and application of the PIP algorithm to extract street candidate points is achieved in an automatic way by using a standard programming environment. In this study, the MATLAB software package is used to read the ESRI shape files (*.shp) of a street network and subsequently street candidate points are extracted by using the MATLAB built-in routine 'inpolygon'. Figure 6.5 shows the extracted street candidate points for the entire street network after the application of the PIP algorithm. A close view highlighted with a circle illustrates the extracted LiDAR points.

6.5.2 Dense polygon boundary points generation

The 2D topographic maps of buildings, parcels and streets are stored as closed polygons and often supplied as ESRI shape file formats (*.shp). Generally these polygons contain very coarse boundary points which are recorded from the field survey. Sometimes the interval between two points can be up to 5 or 6 meters or more. Figure 6.6(a) illustrates a street network consisting of eight polygonal segments with coarse boundary points. Generation of a fine resolution street model requires very dense spatial information on the street surfaces. The proposed street modelling ap-

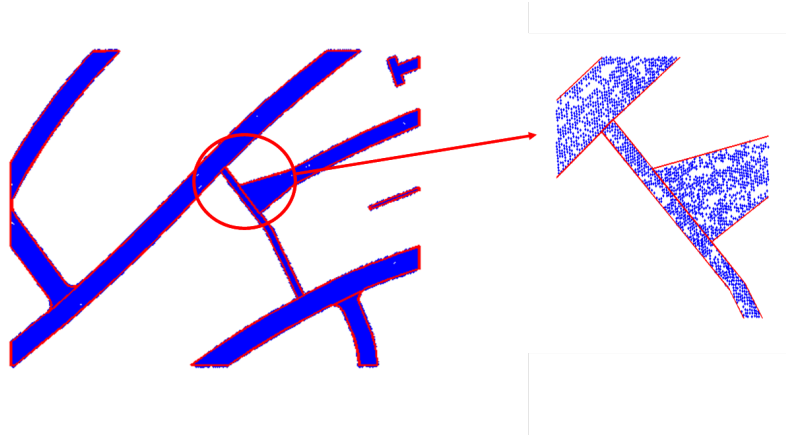


Figure 6.5: Application of PIP algorithm.

proach resorts exclusively to the formation of rectangular blocks running throughout the street networks. The street modelling phases such as delineation of kerbs, surface reconstruction and modelling of junctions require high resolution rectangular blocks ($<0.5\text{m}$). The four vertices of a rectangular block are taken from both sides of a polygon boundary, the centreline being in the middle. Figure 6.6(b) presents the appearance of the street boundary points after they have been densified using a linear interpolation approach. The densification process of the boundary points pro-

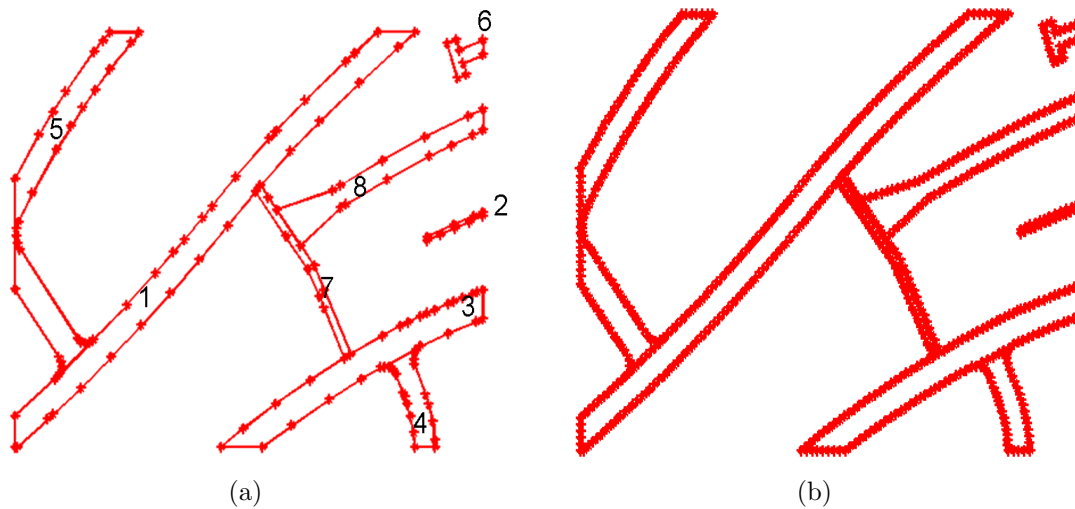


Figure 6.6: Topographic map of a street network with coarse boundary points (a); Dense boundary point generation with linear interpolation (b).

duces fine resolution intervals between any two consecutive boundary points. The details of the formation of rectangular blocks are discussed in Section 6.9.

6.6 Street connectivity (topology) construction

6.6.1 Detection of centreline

The detection of the centrelines is accomplished by applying the skeletonization algorithm. The skeletonization is a technique of extracting the ‘skeleton’ of an object from a binary image. In a nutshell, this technique reduces the thickness of an object to a single line by preserving the original shape of the object. During the application of the skeletonization technique, the topological and geometrical information on the object must be preserved. More details on the skeletonization algorithm can be found in Serra [114] and Gonzalez et al. [52]. In this study, the MATLAB built-in ‘skeletonization’ function is used to extract the centreline of the given street network. It should be mentioned that the skeletonization algorithm can only be applied to a binary image. Figure 6.7 shows a street network with centrelines overlaid on it. In

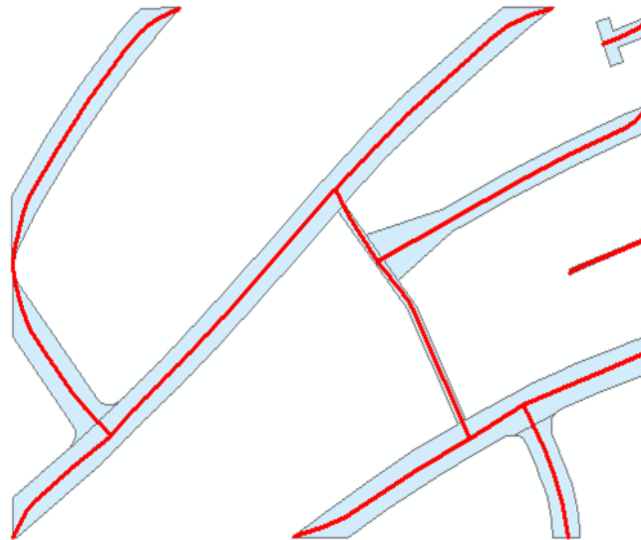


Figure 6.7: Detection of centreline in the street network.

order to serve this purpose, the shape file of the given street network is converted to raster format. Afterwards, the raster image is reclassified as a binary image where each street pixel has a value of 1 and the remaining background pixels have a value of 0. The proposed street extraction algorithm and the subsequent 3D modelling of the streets work on the point data. Once the application of the skeletonization algorithm is completed and the desired centreline output is visible in the binary image, the pixel information is transformed into 2D feature space as a plain text file with appropriate geographic coordinate information.

6.6.2 Construction of street connectivity

In a given street network, the individual street segments are interconnected with one another. The topological information of a street network, i.e. the spatial arrangement among the segment polygons provides information on the position of the street junctions. Automatic modelling of street cross-sections will benefit from the detection of automatic street junction points. In order to achieve this goal, the concept of a connectivity matrix is introduced in this study (Figure 6.8). A connectivity matrix is a 2×2 matrix whose first column stores binary values for both the

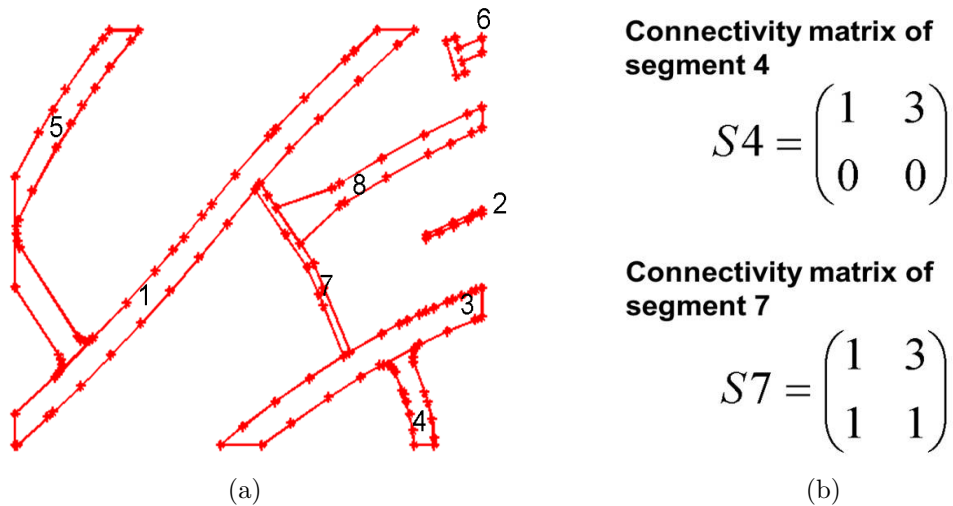


Figure 6.8: Representation of the connectivity matrix.

ends of a street segment where the value 1 shows a connected end and the value 0

represents no connection with any other segment. The second column of the connectivity matrix stores information to which the reference segment is connected to. Figure 6.8(a) shows the street network of the Alcatraz area with numeric numbering of each of its segments. Figure 6.8(b) presents the connectivity matrices of street segments 4 and 7 respectively. The street segment 4 is connected to segment 3 and street segment 7 is connected to both the segments 1 and 3 (Figure 6.8(a)). S4 and S7 represent connectivity matrices for segments 4 and 7 respectively. In matrix S4, the (1,1) element is assigned to 1 as segment 4 has its one end connected to another segment whereas the (2,1) element is set to 0 because the other end of segment 4 has no connection. Again in matrix S4, the element (1,2) is set to 3 because segment 3 is connected to the reference segment (i.e. segment 4). Similarly, the matrix S7 is constructed (Figure 6.8(b)). However, the detection of a junction point has not yet been discussed and this will follow in this paragraph. The centreline information on each street segment is sorted out and the two endpoints of a given centreline are marked as reference points.

A point-searching algorithm is implemented at both the reference points for each street segment. When an endpoint of a given street segment is connected to another segment, a circle of a threshold radius drawn at that end will intersect the centrelines of the connected street segment. It is assumed that the junction point is most likely to be in the middle of the intersected points. In Figure 6.9, A and B are the two street segments (polygon) where A is a reference segment. C is an endpoint lying on the centreline of A. When a circle is drawn at point C, the circumference of the circle intersects the centreline of the street segment B at P1 and P2. The bisected point of the straight line P1P2 is the junction point J. This procedure is repeated for each street segment in order to detect the junction points in the street network in an automatic way. When any street segment is connected to the neighbouring segment, this information is stored for each segment in the connectivity matrix. Thus, complete information can be readily available on the pattern of the connectivity among the street segments. So the implementation of the street-connectivity network provides information on: 1) location of street junctions; and 2) connectivity among the street segments.

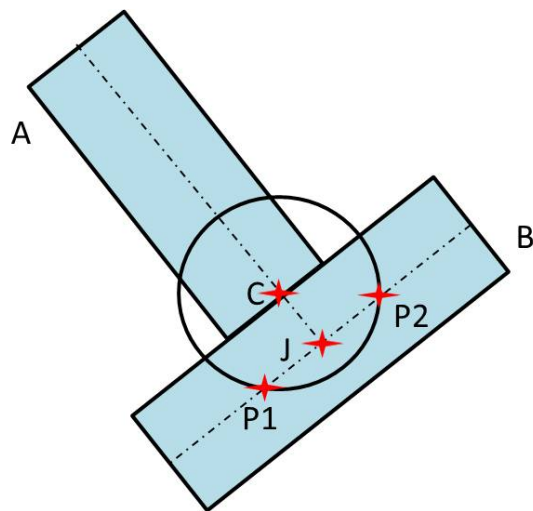


Figure 6.9: Detection of junction point at the intersection.

6.7 Distinguishing the boundary points

This section describes the methodology of separating boundary points of a street segment into two groups: left-side and right-side boundary points with respect to the centreline. The arrangement of the boundary points of a street polygon unit (segment) is completely random, meaning they do not maintain any serial number. The starting point can begin from any point on the boundary lines. When the coarse boundary points are interpolated and the dense points generated, there are no clues about the position of the starting point for each street polygon segment. Without the prior information about the separated boundary points, it would be difficult to implement the formation of the proposed rectangular block.

The separation of the boundary points with respect to the centreline is achieved through a series of steps. At first, the both end points of the centreline of a street segment are determined. In Figure 6.10, ‘End-1’ and ‘End-2’ are the end points of the centreline of a given street segment.

A perpendicular line is drawn at both ends and a thin-patched area centring the perpendicular line is chosen at both the ends. These areas are highlighted in dark brown (Figure 6.10). For each area, the maximum and minimum serial numbers of the boundary points are calculated. For End-1, the maximum and minimum index

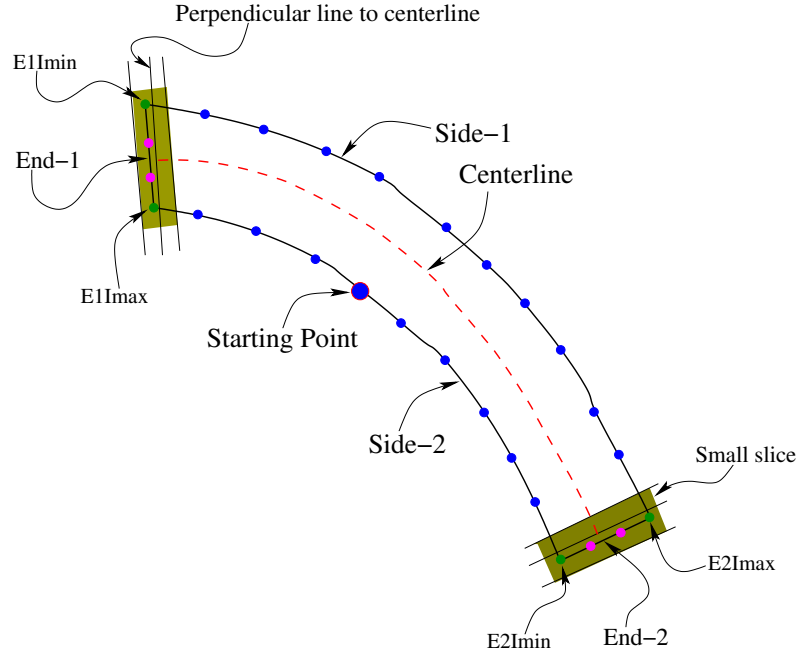


Figure 6.10: Distinguishing left-side and right-side boundary points.

numbers are $E1Imax$ and $E1Imin$ respectively. Similarly, $E2Imax$ and $E2Imin$ represent the maximum and minimum index numbers for the second end. The starting point of the serial number may lie either on a side or on the thin-patched area. Here, it is assumed that the starting point rests on any of the boundary sides. When the starting point lies on any of the boundary sides, the following algorithm separates the boundary points into two groups,

```

if  $E1Imin > E2Imax$  then
     $Side - 1 = X1([E1Imin : -1 : E2Imax])$ 
     $Side - 2 = X1([E1Imax : Tp, 1 : E2Imin])$ 
else
     $Side - 1 = X1([E2Imax : E1Imin])$ 
     $Side - 2 = X1([E2Imin : -1 : 1, Tp : -1 : E1Imax])$ 
end if

```

Here, $Side - 1$ and $Side - 2$ are the two boundary sides, $X1$ is an array containing the serial numbers of the boundary points of the street, Tp is the total number of

points. The approach is applied to each street segment resulting in two distinct arrays for the entire street network.

6.8 Detection of inner boundary lines

6.8.1 Street kerb detection

A kerb (also curb) is an edge where an elevated pavement or a sidewalk meets the lowered street surface. The main function of a kerb is to guide the rainwater into the sewer system through the water inlets to prevent water puddles, thereby avoiding inconvenience to street users and maintaining safe traffic movement. A kerb is also a demarcation line between the street and the sidewalk, keeping vehicles on the street and pedestrians on the sidewalk. Generally the height of a kerb varies between 4 and 12cm. Vivienne K. Dell et al. [123] cast doubt on the assumption that kerbs can be detected from LiDAR, as these data have limited vertical accuracy. Ettrich [43] explicitly shows that there is a clear difference between the height profile of a sidewalk and that of a traffic lane (or street) at a specific location with the presence of kerbs. This fact can be associated with the relative height accuracy of the LiDAR sensor.

In this study, the kerb height from the LiDAR data is attempted to be detected by calculating the height difference between boundary and centrelines. LiDAR data themselves have some inherent noise which is believed to be responsible for their inability to capture a kerb height of less than 4cm. The kerb height is not uniform along the streets and it varies quite often at different location points. Generally, in front of a bus stop, a distinct kerb height of 5-7cm is noticed while the height starts to decline near the junction points. In both study areas, this kerb height is found to be as low as 2-5cm and in some places there are no clear height differences between the sidewalks and the streets. However, independent of the kerb height information, the material composition of the sidewalks differs from that of the streets. The sidewalks are often paved with stones while the street surfaces are mostly (with some exceptions) covered by asphalt. In the high resolution multispectral imagery, the spectral signature can provide meaningful information to distinguish between

sidewalks and streets. A change in the colour gradient can be noticed along the kerb line in the multispectral images. Figure 6.11(a) presents part of a street in the Alcatraz study area and the detected edges after the application of Canny edge detection technique (Figure 6.11(b)).

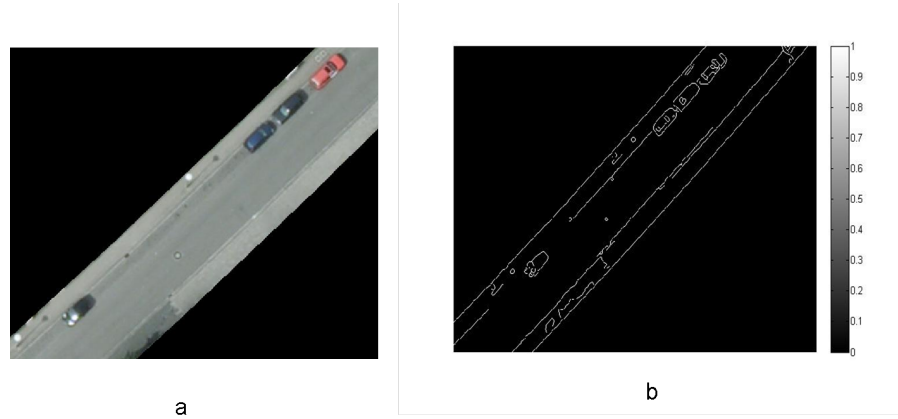


Figure 6.11: Clipped aerial image of a street segment (a) and detected edges (b).

This study proposes a method to detect the kerb line from the high-resolution (10 cm) aerial image using the Canny edge detection technique. The application of the Canny edge detection algorithm to the entire dataset of the aerial image will produce object outline boundaries for each object, both natural (trees) and man-made (buildings, streets, cars). These numerous edge lines will increase the complexity of the study scene and computational effort when the goal of the study is to focus on the street areas and kerbs. An image-clipping technique is performed as a pre-processing step to extract only the street networks from the aerial image, making the search domain smaller and the computational effort faster. Later, the Canny edge detection algorithm is applied to the clipped aerial image.

6.8.2 Delineation of street kerb

The detected edges (pixels) in the binary image (Figure 6.11(b)) are mapped onto the feature space with an appropriate coordinate system which is shown in Figure 6.12(a). A close look at the mapped feature data reveals discontinuities and occlusions in the kerb line, caused, for example by parked cars. The distances be-

tween the centreline and the kerb line of both sides are measured at intervals of 5 metres along the street.

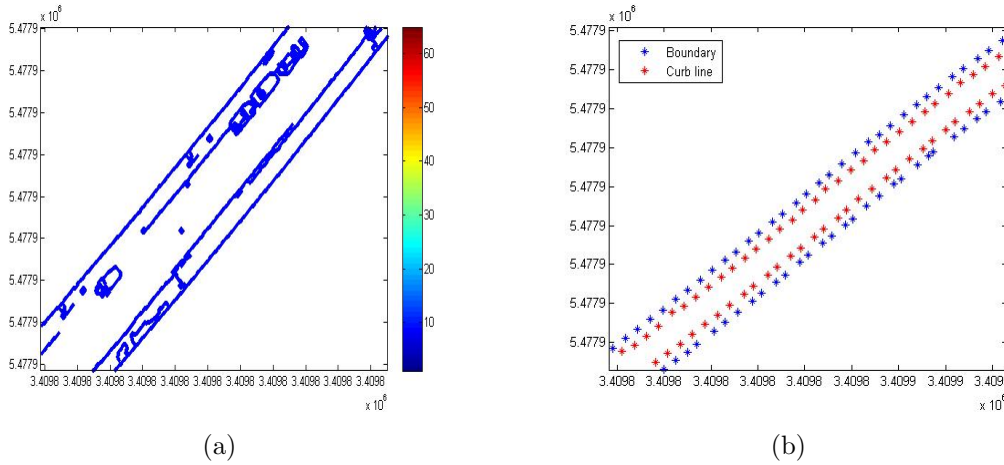


Figure 6.12: Mapping of detected edges from pixel domain to feature space (a) and interpolated boundary and kerb line (b).

Three assumptions are made during the distance calculation between centrelines and kerbs:

- If the distance between a centreline and a kerb line is equal to the distance between a centreline and a boundary line, an assumption is made that no detected kerb line is present.
- If the distances from a centreline to both kerb lines are not equal, then either of the kerb lines is occluded by the cars.
- The missing kerb lines are interpolated by the nearest kerb points and occlusion from cars is replaced by the distance from another side. Figure 6.12(b) shows the interpolated kerb points (red) and boundary points (blue).

6.9 Reconstruction of street surfaces

6.9.1 An ideal street model

The surface reconstruction process attempts to model the street network by transforming it from the planimetric to a realistic 3D model by representing the geometric properties of an ideal street cross-section (Figure 6.13).

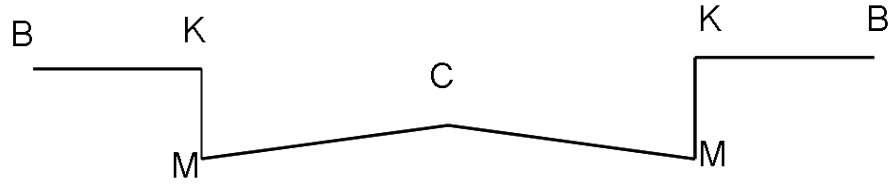


Figure 6.13: An ideal street cross-section.

In Figure 6.13, C is the centreline, CM represents the street surface (traffic lane), KM is the kerb height and BK is width of the sidewalk. In reality, the width of sidewalk of both sides may not be equal. K denotes the upper point of the kerb KM while M denotes the lower point. The implementation of rectangular blocks is a key characteristic of the proposed approach to street modelling. Figure 6.14 illustrates the formation of rectangular blocks for a given street segment. This mentioned street segment consists of five boundary points where L_1, L_2, \dots, L_5 represent left-side and R_1, R_2, \dots, R_5 represent the right-side boundary points (Figure 6.14(a)). Figure 6.14(b) illustrates the formation of rectangles by sharing four vertices at each time. For example, the points L_1, L_2, R_2 and R_1 form four vertices for the first rectangle $L_1L_2R_2R_1$. In the next step, the points L_2, L_3, R_3 and R_2 form the next rectangle $L_2L_3R_3R_2$ and the process continues $(N-1)$ times where N is the number of boundary points on a single side.

6.9.2 Assigning heights to centrelines and sidelines

Section 6.6, 6.7 and 6.8 describe the planimetric position of the centrelines, the boundary lines and the inner kerb lines respectively for each street segment (also

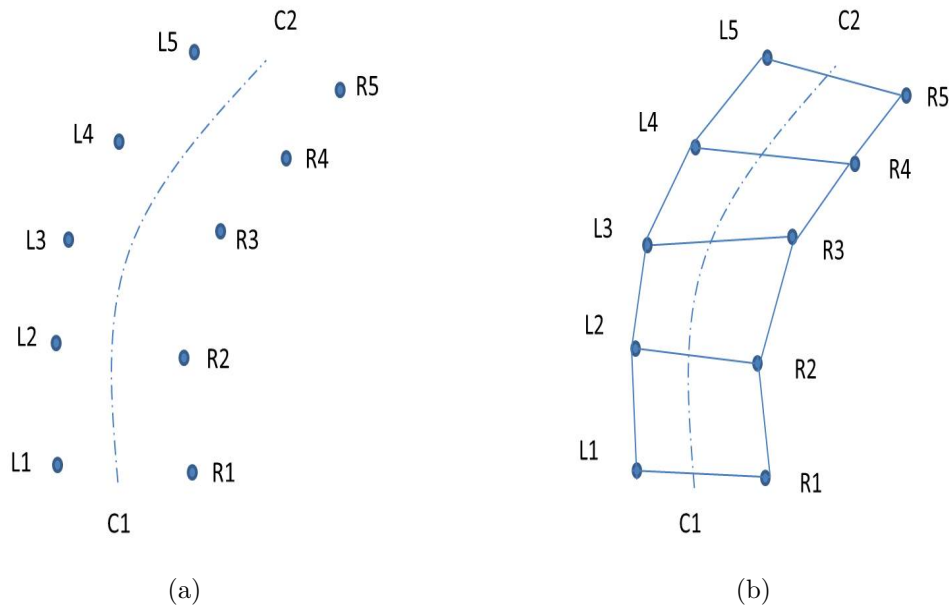


Figure 6.14: Formation of rectangular blocks.

polygon unit) within the entire street network. The process of surface reconstruction begins by removing outliers from the street scene caused by cars and trees. This step is followed by the assignment of height values as a third dimension to the planimetric boundary, kerb and centreline points. Figure 6.15 illustrates the planimetric view of a street segment with boundary (red), kerb (violet) and centreline (cyan) points.

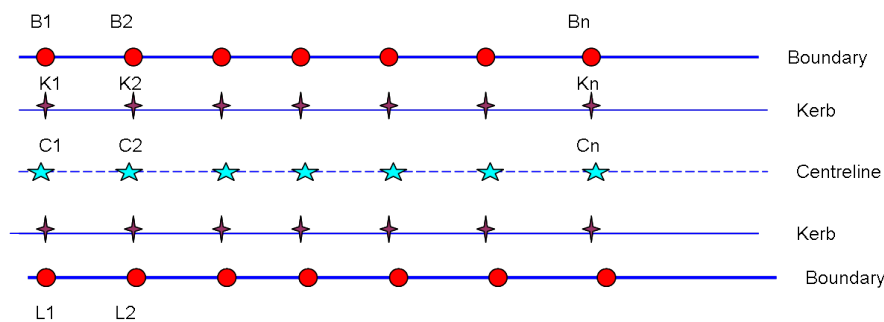


Figure 6.15: Planimetric view of a street segment with boundary, kerb and centreline points.

In a real-world scenario, cars are parked along the street boundary in a residential area. In a commercial or industrial area, both moving vehicles and parked vehicles are seen in a busy street. Thus, the first step towards street surface reconstruction is to remove the height anomalies from the street surface caused by the presence of cars and trees. A height threshold value Δh is chosen and any elevation information higher than that threshold is treated as an outlier. In the Alcatraz study area, the height of the street boundary walls in some places is higher than that of the cars. In order to retain the boundary walls during the filtering process (Chapter 4), many cars were left on the street surfaces. In this study, a height threshold value Δh is set for both the study sites, taking the standard height of a car ($\sim 1.3 - 1.5$) as base measurement for removing outliers. This threshold value is set automatically and locally for each rectangular block for a given street segment in order to avoid any artificial disturbance along the global height profile of that particular street segment. Sometimes, a given street polygon might have global height differences of up to a few metres. Thus, setting up a general threshold value for the entire street segment to remove vehicles might eventually result in the removal of some parts of the street surface points. Figure 6.16(a) presents LiDAR points extracted by a rectangular block with outliers, and Figure 6.16(b) shows the removal of the outliers and fill-up of the vacant spaces by linear interpolation. An example of a rectangular block can be referred to as either B1B2L2L1 (Figure 6.15) or L1L2R2R1 (Figure 6.14(b)).

In the second step, height values are assigned to boundary points (B_1, B_2, \dots, B_n) and (L_1, L_2, \dots, L_n) and centreline points (C_1, C_2, \dots, C_n) presented in Figure 6.15. For example, at the time of assigning height value to a centreline point C_1 , a circle with a radius of 0.5 metres is drawn at the point C_1 . The street points encapsulated by the circumference of the circle are averaged out to calculate the mean value for point C_1 . Figure 6.17 shows the arrangement of street points inside a circle and the calculated average value for point C_1 . In the same way, height values are assigned to all the boundary points of two sides, kerb and centreline points. The assumption is made that the boundary points (B_1, B_2, \dots, B_n) and the kerb points (K_1, K_2, \dots, K_n) in Figure 6.15 have the same height values. A cross-sectional profile of the planimetric view shown in Figure 6.14 would look like the one shown in Figure 6.13.

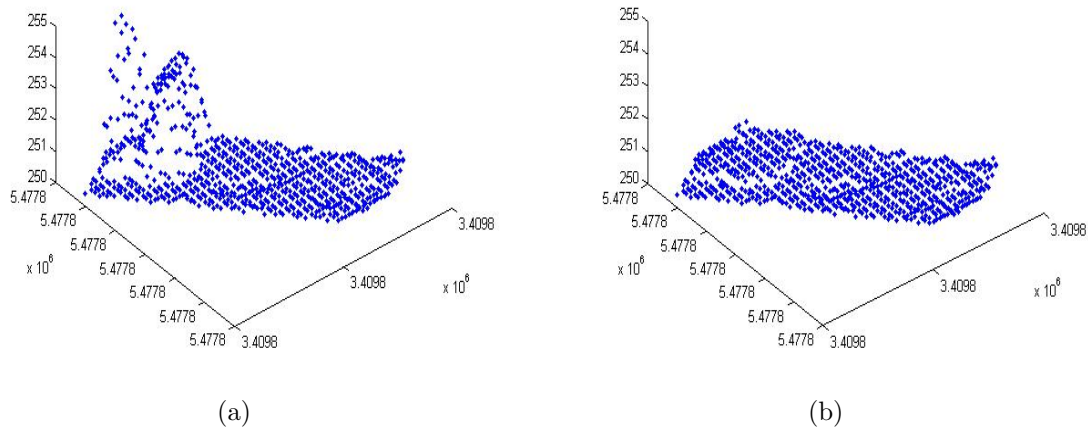


Figure 6.16: Threshold set up and removing of outliers.

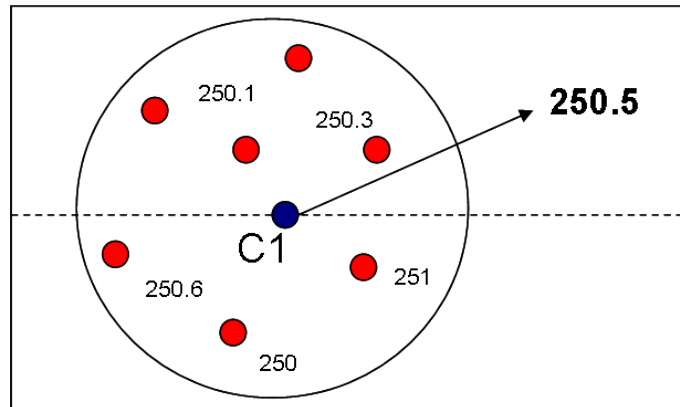


Figure 6.17: Assigning height value to the centreline point.

In the third step, a height value is assigned to the point M in Figure 6.13. The height of point M (h_m) is calculated in following equation,

$$h_m = h_c - 0.02 * \frac{w}{2}$$

where, h_c is the height at point C and w is the width of the street. A slope value of 2% is maintained between the points C and M in order to direct the water towards the inlets.

6.10 Modelling of street junctions

A street junction within an extracted and smoothened street network is a location where one or more street segments intersect. A street junction usually, if not always, spots a manhole location and requires detailed hydraulic information on the connected street segments. The interaction between pipe flow and surface flow at a street junction is complex in nature during the surcharged sewer conditions. Figure 6.18 illustrates the 3D modelling and visualization of a junction featuring kerbs, sidewalks and traffic lanes. A red circle covering the junction on the aerial image indicates the exact location of the junction in the aerial image (Figure 6.18). Every

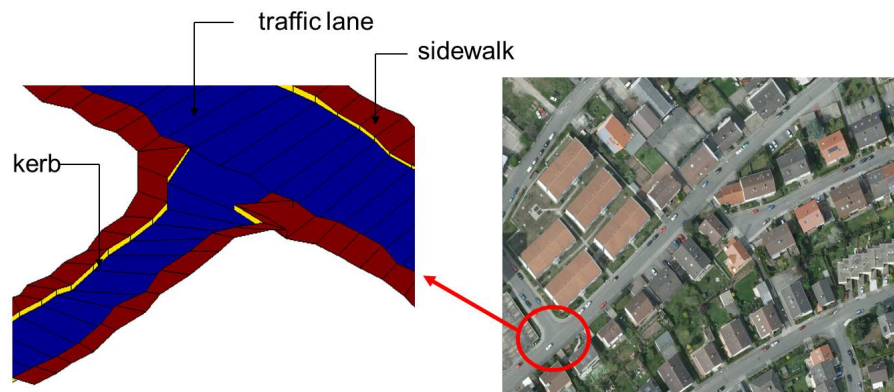


Figure 6.18: 3D visualization of a junction point with detailed sidewalks, kerbs and traffic lanes information.

phase (or module) of street modelling algorithm is implemented on each street segment (polygon) individually and in an automatic manner to cover the entire street network. When a street segment is connected to another segment, there is no street pavement and kerb at the junction points. Also the slope and height information of two connected segments might vary considerably depending on the terrain types. The modelling of a street junction is implemented in three stages:

- Detection of boundary line and kerb lines at the intersecting junction
- Deletion of the detected lines
- Reconnection of two segments

In Figure 6.19(a), two street segments A and B form a junction, where A is the horizontal segment and B is the vertical segment. C1 and C2 are the points on the boundary and kerb line respectively lying at the end of segment A. A circle centring on C1 is drawn in such a way so that it intersects both the boundary and the kerb line of segment B. The intersected boundary points (Figure 6.19(a)) and kerb points (Figure 6.19(b)) are highlighted in red. The middle point out of the highlighted boundary points is temporarily selected and its next neighbour point in the direction of and parallel to C1 is denoted as P1. Similarly, circles centring on points C2, C3 and C4 give rise to the points P2, P3 and P4 respectively (Figure 6.19(b) and (c)). The pairs of points (C1, P1), (C2, P2), (C3, P3) and (C4, P4) are connected linearly in order to retain the geometric properties of streets at the junction (Figure 6.19(d)). However, the boundary points between P1 and P2 and kerb points between P3 and P4 are set to redundant and subsequently deleted.

6.11 Application

The complete methodology described in Section 6.5 to 6.10 is applied to two different study areas: 1) Alcatraz and 2) Casimirring. Figure 6.20 illustrates the 2D view of the extracted and modelled street network of the Alcatraz area with detailed sidewalks, traffic lanes and junctions. In this output map, the modelling of two tiny street segments (Figure 6.6(a), segment numbers 2 and 6) is ignored. Those segments have barely any area, and detection of sidewalks and kerbs would not be of applicative interest. The detailed 3D visualization of a junction point with explicit detailing of street elements such as kerbs, sidewalks and traffic lanes has been shown in Figure 6.18. Also, in the modelled street network a clear height difference is noticed between sidewalks and centreline of the street. Figure 6.21(a) presents the aerial image of the Alcatraz area highlighting a boundary line (B1B2) and centreline (C1C2). Figure 6.21(b) illustrates the height profile of the boundary B1B2 and the centreline C1C2 marked by blue and red lines respectively. A clear height difference between the boundary and centreline is observed for a selected street segment. The range of the height difference varies from 2 to 4 cm in this case. Figure 6.22(a) presents the modelling of a relatively complex street network in the

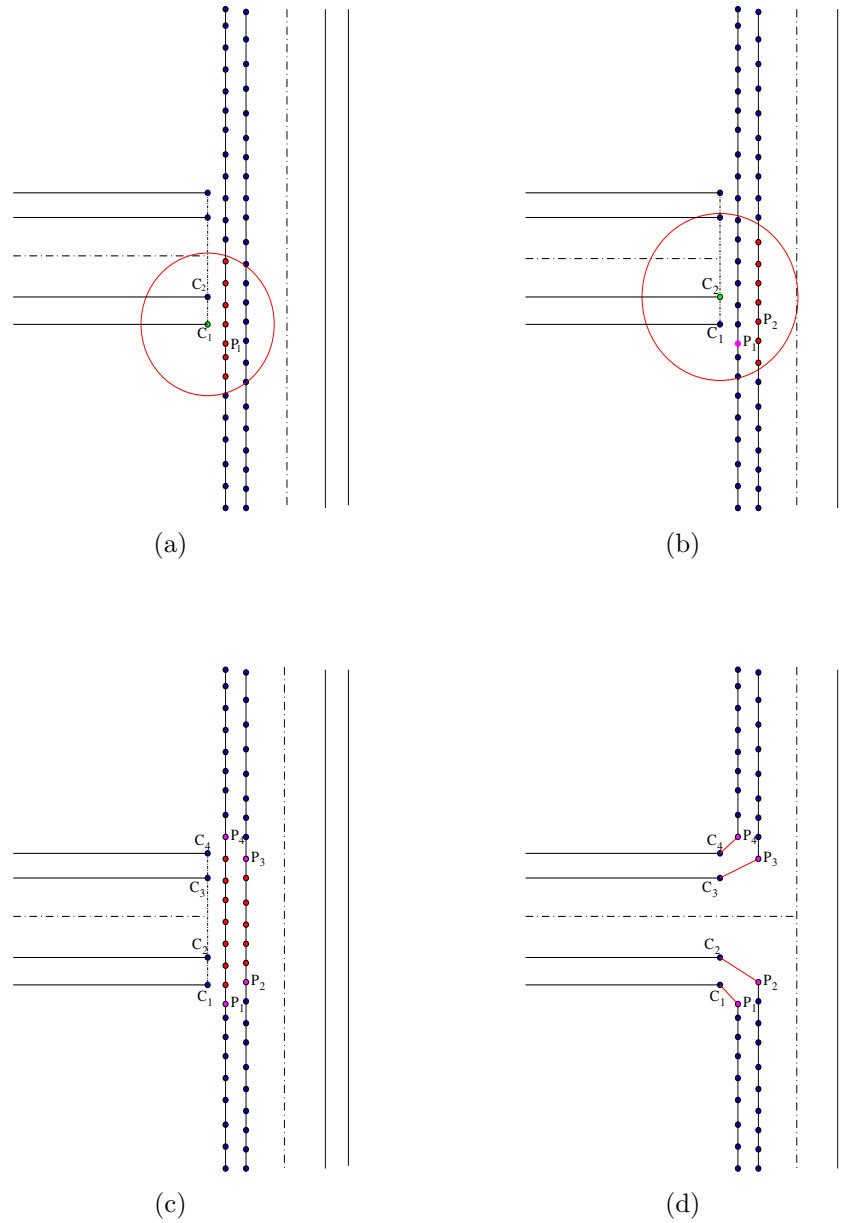


Figure 6.19: Modelling of the street junction.

Casimirring area. The study area near Casimirring has a complex arrangement of street networks with street polygons in a variety of shapes and sizes. Most of the junction points contain three or four street segments, making the scene complex, whereas all the street junctions near Alcatraz have only two street segments. The

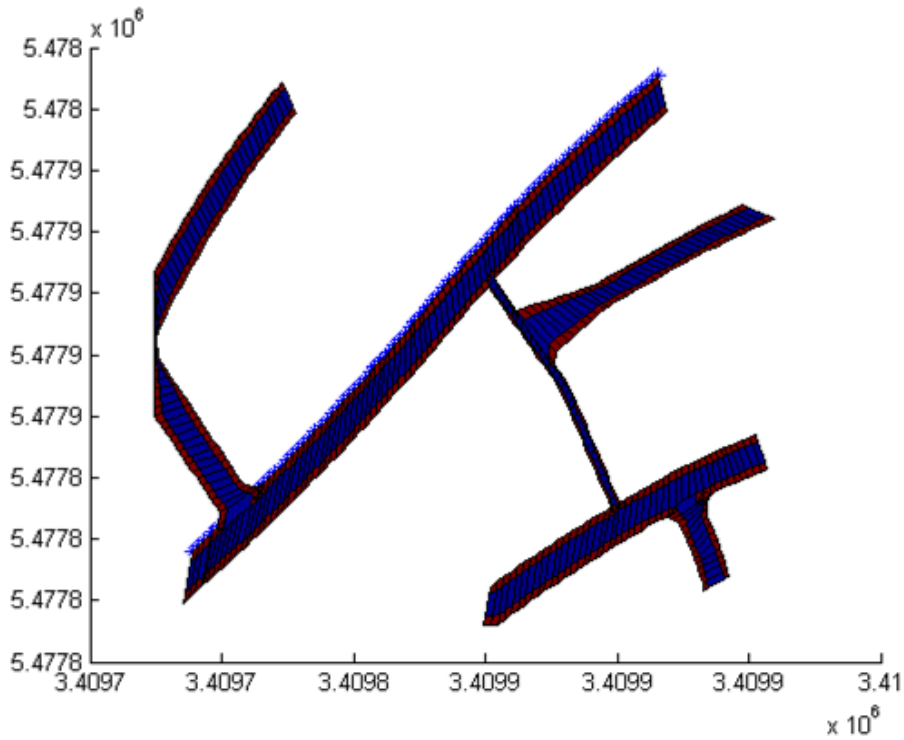
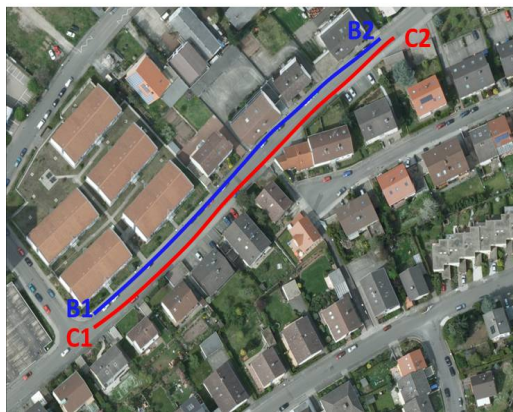
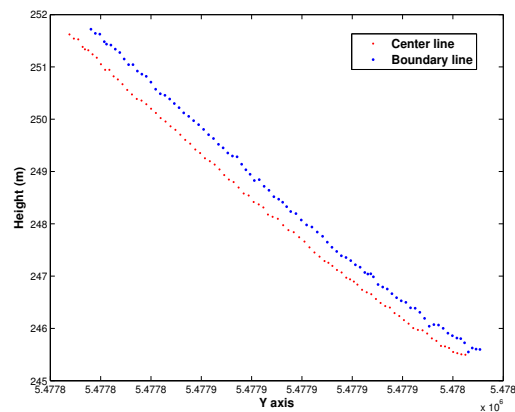


Figure 6.20: Planimetric view of the modelled street network at Alcatraz area.



(a)



(b)

Figure 6.21: Highlighting a boundary line and a centreline for generating height profile (a); Height profile of the highlighted street segment (b).

proposed street extraction and 3D reconstruction algorithm also perform well in generating a detailed street model of this area. Figure 6.22(b) illustrates the 3D

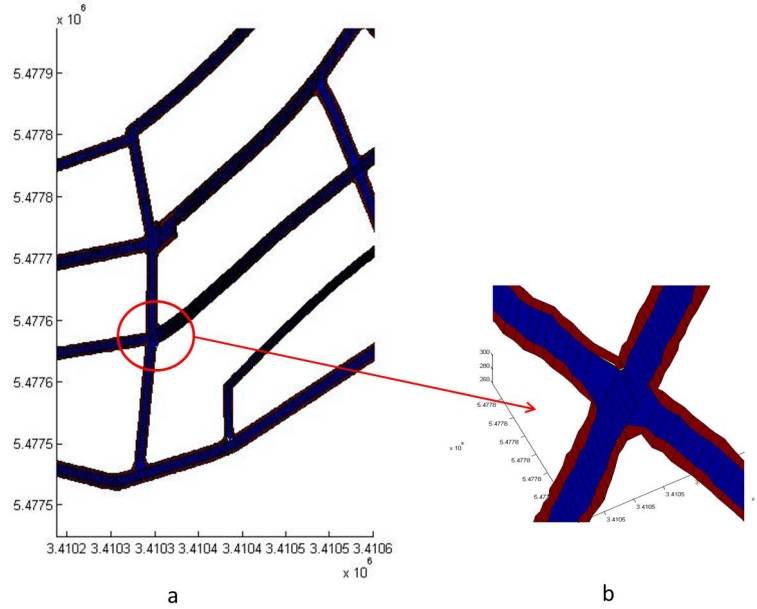


Figure 6.22: Planimetric view of a relatively complex street network near Casimirring after the application of the 3D reconstruction techniques.

view of a complex junction point containing four street segments. In this area, some street segments suffer from occlusions due to the presence of overhanging trees from both sides of the streets. The coarse point density (sometimes no points at all) within an occluded street scene causes difficulty for the the implementation of rectangular block formation technique (Figure 6.14). When a rectangular block does not find enough LiDAR points inside it, the assignment of height for boundary lines, kerbs and centrelines is achieved by taking information from the neighbour rectangular blocks where the point density is high. Thus the estimated elevation data in the occluded area might represent some deviation from the reality.

6.12 Validation

In order to validate the reconstructed 3D street network, eleven ground truth points are selected manually for both study areas. These ground truth points are collected from the field survey data supplied by the Kaiserslautern municipal office.

Figure 6.23 shows the plot of ground truth height vs. calculated height of the Alcatraz street network and Figure 6.24 shows the same plot of the Casimirring street network. Abdullah et al. [1] describe a quantitative test in order to compare the

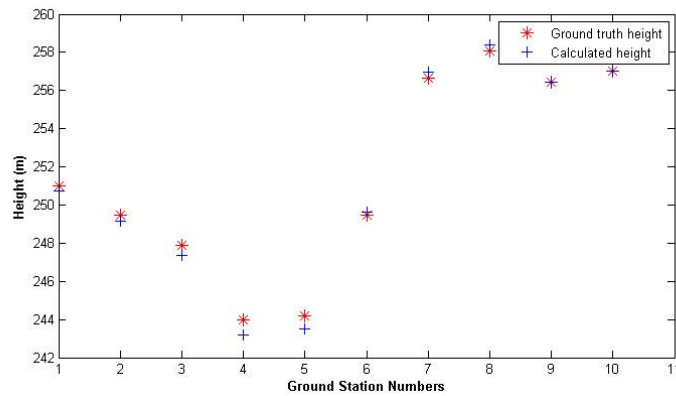


Figure 6.23: Differences in ground truth height and calculated height of Alcatraz street model.

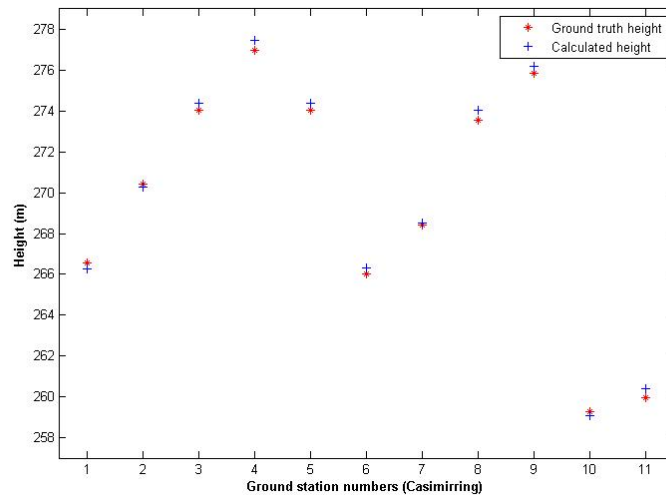


Figure 6.24: Differences in ground truth height and calculated height of Casimirring street model.

filtered elevation to the actual ground data by calculating the Root Mean Square Error (*RMSE*) with the following formula,

$$RMSE = \sqrt{\frac{1}{N} \sum_{i=1}^N (Y_i - G_i)^2} \quad (6.1)$$

Where, Y_i is the calculated height from the model and G_i is the ground truth height. Using the above equation, the calculated *RMSE* of the Alcatraz and Casimirring areas are found to be 0.13 and 0.18 respectively. The lower *RMSE* values (< 0.2) for both the areas suggest a close correspondence between the calculated elevation and the actual elevation.

6.13 Limitations

The street extraction and the 3D reconstruction techniques have the following limitations:

- At present, this algorithm can be applied only to a single-layer street network
- The algorithm does not work in a situation where a parking place is located next to the street boundary. In this specific case, the boundary lines and kerbs are shifted at the end of the parking lot's boundary (Figure 6.25). Actually, this information does not come with the 2D topographic maps.
- The implementation of Canny edge detection technique requires choice of a threshold value. An appropriate threshold value can be found by repetitive application of the edge detection algorithm till to the point the edge lines look continuous and with moderate thickness.

6.14 Summary

Detailed street modelling can ensure improved geometric properties of the streets, characterizing them as open channels. Geometric properties such as area, wetted

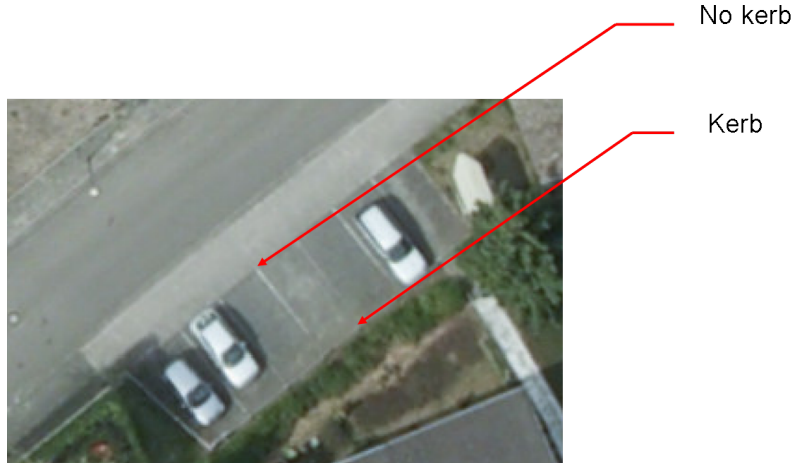


Figure 6.25: Shift in kerb line to accommodate the parking place next to the street.

perimeter and hydraulic radius of a street cross-section are believed to play an important role in the overall flow dynamics while conveying overland flow on the street surface, assuming shallow flood depths (Neelz and Pender [95]). Also, the value of Manning's coefficient can be influenced by the surface roughness if the surfaces are not properly smoothed. This chapter has proposed a framework for the extraction and reconstruction of a single-layer 3D street network aiming at improving the understanding of the urban surface drainage systems. The detailed modelling of sidewalks, kerbs, traffic lanes and junctions is implemented in an automatic way by integrating airborne LiDAR data, topographic maps and aerial images. In order to assess the accuracy, the surface elevations of the modelled street networks are validated against the field data. The calculated *RMSEs* (root mean square error) are found to be 0.13 and 0.18 for Alcatraz and Casimirring area respectively, describing the validation as close to the reality. Further insight is needed into the validation of the Casimirring street network. Some street segments at this area are partly covered by trees from both sides of the streets. The absent of street manholes at this occluded parts makes the validation task difficult because the ground truth data are taken from manhole elevations for this purpose. The application of Canny edge detection technique and subsequent kerb lines reconstruction are implemented in a separate module and needs to be integrated with the main modelling module in the future. The methodology proposed in this study is repeatable and can be applied

to different urban scenes as long as it is concerned with single-layer street networks. The street modelling framework does not work in a situation where a parking place is located next to the street boundary.

Chapter 7

Impervious(paved) and pervious(unpaved) surface detection

7.1 Introduction

This chapter describes the detection of different surface types by adopting an Object-based Image Analysis (OBIA) approach. The detection of buildings and streets has been described in Chapter 5 and Chapter 6 respectively and hence this chapter pays attention to the classification of rest of the terrain (e.g., grassland, bare soil, impervious areas covered by parking lots, home yards etc.) by using LiDAR intensity data and aerial images. The number of surface types is restricted to two (pervious and impervious) for the study sites of Alcatraz and Casimirring. An additional investigation is carried out in a third study area Harzhübel featuring predominantly bare soil, grassland and other impervious surfaces.

7.2 Overall approach

The detection of different types of urban surface is an important task for estimating the volume of stormwater runoff contributing to the storm sewer system. In this

research work, an OBIA approach has been adopted to first segment the image and afterwards to apply the knowledge-based rule-set approach in order to classify pervious and impervious areas of both study areas. The segmentation algorithms operate on all the available image layers. In Definiens software (Definiens [156]), users can upload several image layers in the view window as long as all the layers correspond to the same geographical coordinates and projection system. Application of any segmentation algorithm will segment all the available image layers simultaneously. Chessboard and multiresolution segmentation have been utilized sequentially. Figure 7.1 illustrates the complete workflow of the surface classification approach. The main steps of the impervious and pervious surface detection are as follows:

- Layer stacking/waveband fusion: Red, green and blue bands of the aerial image and LiDAR intensity band.
- Chessboard segmentation: the wavebands and the thematic map containing buildings and streets.
- Region of interest (ROI) selection in the image by masking streets and buildings.
- Multiresolution segmentation
- Rule-set development
- Classification results

The details of each step are presented in the following subsections.

7.2.1 Image layer stacking

An aerial multispectral image usually comprises three colour channels, namely red, green and blue. Conversely, a spaceborne multispectral image has additional colour channels in the Near Infrared (NIR) zone. Each channel of a multispectral image is known as an image layer or waveband. The term ‘waveband’ is also known simply as ‘band’. A user can also import additional bands such as LiDAR elevation or

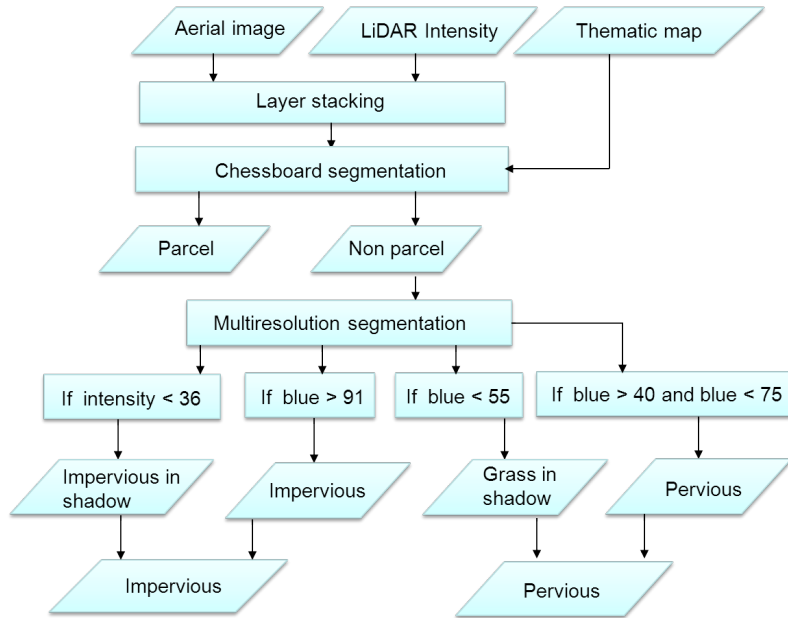


Figure 7.1: The work flow of pervious and impervious surface detection.

LiDAR intensity band in Definiens. Figure 7.2 presents the datasets used for the identification of surfaces in the Alcatraz area. Stacking of several image layers can be



Figure 7.2: Stacking of image layers: Aerial image of the Alcatraz study area with RGB layers (a) and LiDAR-derived intensity layer (b).

achieved by using a commercial software packages such as Definiens. In this study,

Definiens has been used to load both the aerial image and the LiDAR intensity image in the view window.

7.2.2 Chessboard segmentation

The primary step in any OBIA approach is to segment an image by choosing an appropriate segmentation algorithm. Definiens software offers a number of segmentation algorithms such as multiresolution, chessboard and quadtree, to name a few. Although multiresolution segmentation is the most commonly-used algorithm for assigning a class label to the segmented objects, other segmentation algorithms such as chessboard segmentation are also useful, particularly when a user wants to segment an image by an external input such as a thematic map. The Chessboard Segmentation algorithm splits the pixel domain or an image object domain into square image objects (Definiens [156]). Figure 7.3 illustrates the functioning of chessboard segmentation.

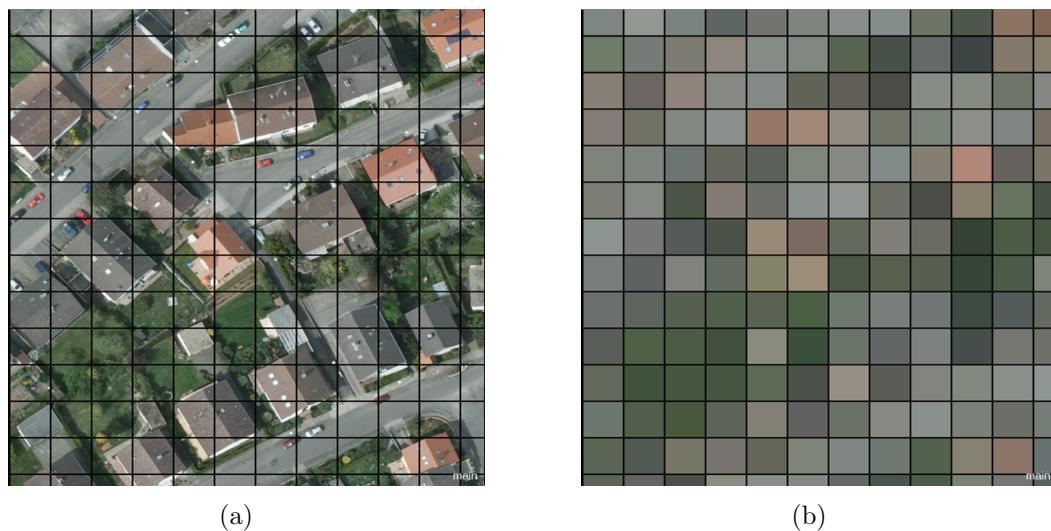


Figure 7.3: Example of chessboard segmentation.

The chessboard segmentation algorithm in Definiens environment offers the option of importing external thematic maps and subsequently segmenting the image according to the shape of the thematic map. Thus the users have the flexibility of using both

the default square-grid segmented image as well as the user-controlled segmentation by a thematic map input. In this study, the user-controlled chessboard segmentation has been used in order to mask out the buildings and streets in the aerial image. The employment of the chessboard segmentation with the help of a thematic map splits the whole image domain into two parts: 1) image pixels inside the thematic map; 2) image pixels outside the thematic map. A user has the flexibility to choose any of the parts and perform the next level of analysis. As this study is only concerned with classifying image pixels outside the thematic map, a simple rule-set is developed by choosing the algorithm ‘assign class’ and setting the target class as ‘parcels’ in order to mask out the buildings and trees. Figure 7.4(a) shows the thematic map with buildings and street polygons. This thematic map is used to mask out the aerial image shown in yellow (Figure 7.4(b)).

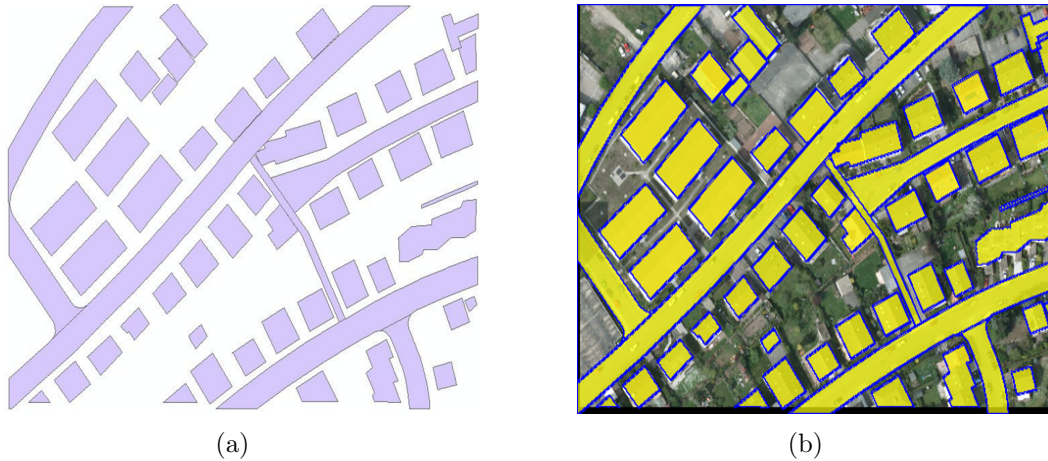


Figure 7.4: Masking out the buildings and streets in the aerial image of the Alcatraz study area. Topographic map of buildings and streets (a). Masked area highlighted in yellow (b).

7.2.3 Selection of region of interest (ROI)

After masking out the aerial image (including intensity band) with the thematic map, the rest of the image domains remain for further processing. Figure 7.5(a) illustrates the ROI in maroon after masking the image. In order to develop knowledge-based rule-sets, multiresolution segmentation is only applied to the ROI (Figure 7.5(b)).

The masking of the aerial image with the help of the thematic map is important in two ways:

- Chapter 5 and 6 of this study present the automatic detection of buildings (also trees) and streets respectively. At this point, their detection is redundant.
- Masking out buildings and streets reduces the spectral confusion among the urban surfaces. For example, buildings, streets and other impervious surfaces have similar spectral reflectance. The less the spectral confusion, the greater is the efficiency of the knowledge-based expert system in classifying different surfaces with accuracy.

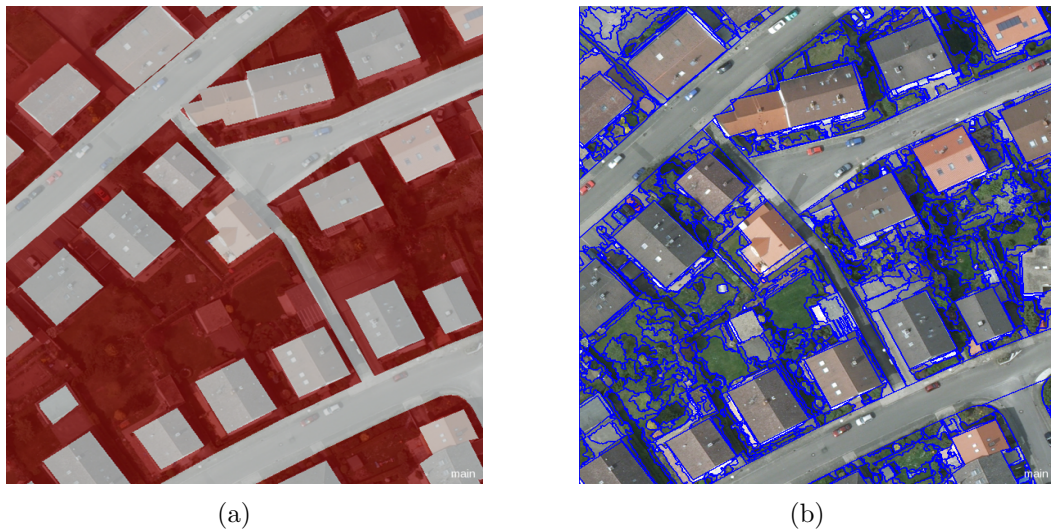


Figure 7.5: Detection of region of interest: a subset of the study area featuring region of interest (ROI) in maroon (a). Multiresolution segmentation applied only in the ROI, excluding areas covered by buildings and streets (b).

7.2.4 Multiresolution segmentation

Multiresolution segmentation is one of the powerful modules embedded in Definiens software offering the foundation of OBIA approach. A segmentation algorithm attempts to subdivide an image by creating a number of homogeneous image objects.

The criterion of ‘homogeneity’ is usually achieved by analysing spectral and spatial information of an image. Thus an image object serves as a basis to assign a set of homogeneous pixels to a class label. The commercial software package Definiens uses the fractal net evolution approach (FNEA) for image segmentation purposes (Li et al. [81]). The FNEA-based image segmentation technique embedded in Definiens is also known as multiresolution segmentation (Baatz and Schape [11]; Martha and Kerle [87]). Multiresolution segmentation is a bottom-up region-growing approach which takes into account spectral, shape and scale factors for segmenting an image scene (Li et al. [81]). An image object is a collection of pixels having similar spectral and textural properties (Navulur [93]). The size of an image object depends mainly on the choice of the scale factor in Definiens. A larger scale factor (e.g., ≥ 50) generates larger image objects while the choice of smaller scale factor (e.g., < 20) generates smaller image objects (Myint and Stow [91]). In this study, four different scale factors (20, 50, 70 and 100) are tested in order to obtain first-hand information about the size of the image objects and the level of details associated with each scale factor. Figure 7.6 illustrates the implementation of multiresolution segmentation algorithm by choosing four different scale factors.

The scale factor 20 produces the smallest objects with a high level of detail while scale factor 50 generates relatively larger objects. Conversely, the scale factors 70 and 100 produce larger objects than the previous two scale factors by merging the neighbouring objects that have less contrasting spatial and spectral information. Figure 7.6 illustrates the effect of choosing a particular scale factor on image segmentation. Figure 7.6(a) shows a subset of the Alcatraz study scene after applying the multiresolution segmentation algorithm with a scale factor of 20. A grassland patch highlighted by a red circle shows many segmented small objects. The same grassland patch shows only one segmented object if a scale factor of 70 is chosen (Figure 7.6(b)). Although the choice of scale factor directly influences the level of detail of an image scene, the users have flexibility to choose the desired level of detail depending on their requirements, scene complexity and the number of classes in the output map. By visual inspection, scale factors 70 and 100 produce relatively large image objects with a reduced level of detail. However, the desired ‘level of detail’ mainly depends on the user’s perspective, scene complexity and the number

of classes in the output map. Scale factor 70 has been found to feature a sufficient level of detail to categorize the ROI into two land cover classes: 1) pervious and 2) impervious areas. In this study, multiresolution segmentation with a scale parameter of 70 has been performed while maintaining the shape and compactness factors 0.1 and 0.5 respectively.

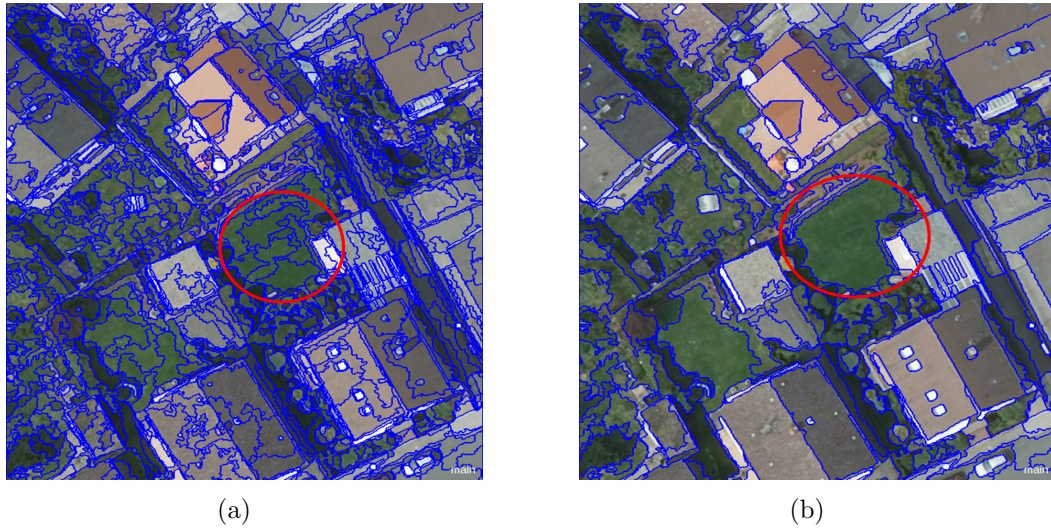


Figure 7.6: Multiresolution segmentation at different scale parameters: scale parameter 20 (a); Scale parameter 70 (b).

7.2.5 Rule-set development

The development of a rule-set starts with the visual inspection of the subset of a given image to be analysed. A representative part featuring almost all types of land classes should be chosen as a subset of the original image covering the whole study area. In this study, the preferred procedure has been to look at the different parts of the image to identify some common features. A feature is defined as an attribute which provides specific information regarding the segmented image objects (Myint and Stow [91]). An attribute can be an individual waveband value, geometric shape or texture in the Definiens environment.

The goal is to classify the ROI into two categories, namely pervious and impervious areas. There are four available wavebands (RGB bands from aerial image and

intensity band from LiDAR data). The first step is to visually analyse individual wavebands in order to observe whether a particular surface type stands out from the whole image scene. A blue band (B) layer value greater than 70 could capture most of the impervious areas. At the same time, this threshold value also includes some shadow areas. The study area features two types of shadow-covered areas: 1) grassland covered by shadows; and 2) impervious surface covered by shadows. Another observation reveals that a suitably chosen LiDAR intensity band could capture most of the pervious surfaces with the exception of some trees and some grassland covered by shadows. At this point, there is an attempt to classify the grassland under shadow by choosing an appropriate threshold value of a specific waveband. Visual analysis evaluates that the blue band (B) value of less than 55 can capture most of the grassland covered by the shadows. The second step is to attempt to detect all the impervious areas. It is observed that most of the impervious areas can be detected by choosing a threshold value in the blue band (B). Visual observation reveals that the blue band value greater than 91 is optimal in this case.

By setting this value, the impervious areas under the shadows cannot be detected. At this point, the shadow-covered impervious areas can be detected by choosing the appropriate image band with the correct threshold value. Visual observation again illustrates that the LiDAR intensity band, having a layer value of less than 36, could capture all the impervious areas under the shadows. Table 7.1 presents the summary of the expert system rule-sets developed in this study.

	Expert systems rule	Surface types
Rule 1	Blue band layer value < 55	Grassland under shadows
Rule 2	Blue band layer value > 91	Impervious areas
Rule 3	Intensity band layer value < 36	Impervious areas under shadows
Rule 4	Intensity > 36 and blue < 75	Pervious areas (grassland and bushes)

Table 7.1: Expert system rule-sets developed for the Alcatraz area.

7.2.6 Classification results

In this section, the application of each expert rule described in the previous section is illustrated. At this point, the Alcatraz dataset is chosen in order to classify

pervious and impervious areas. First, the rule-set 1 is applied in order to identify the grasslands under the shadow. Figure 7.7 illustrates the detection of grasslands under the shadow by using blue band value of less than 55. There is clear evidence of the juxtaposition of grassland and concrete surface under the shadow cast by the buildings (Figure 7.7(a)). An expert system rule-set can detect only the grassland under the shadow (Figure 7.7(b)). In the second step an attempt is made to detect the impervious areas in the study scene. It should be recalled at this point that buildings and streets from the study area are excluded as they have already been detected and modelled in Chapter 5 and 6. Rule-set 2 is applied as discussed in Section 7.2.5.

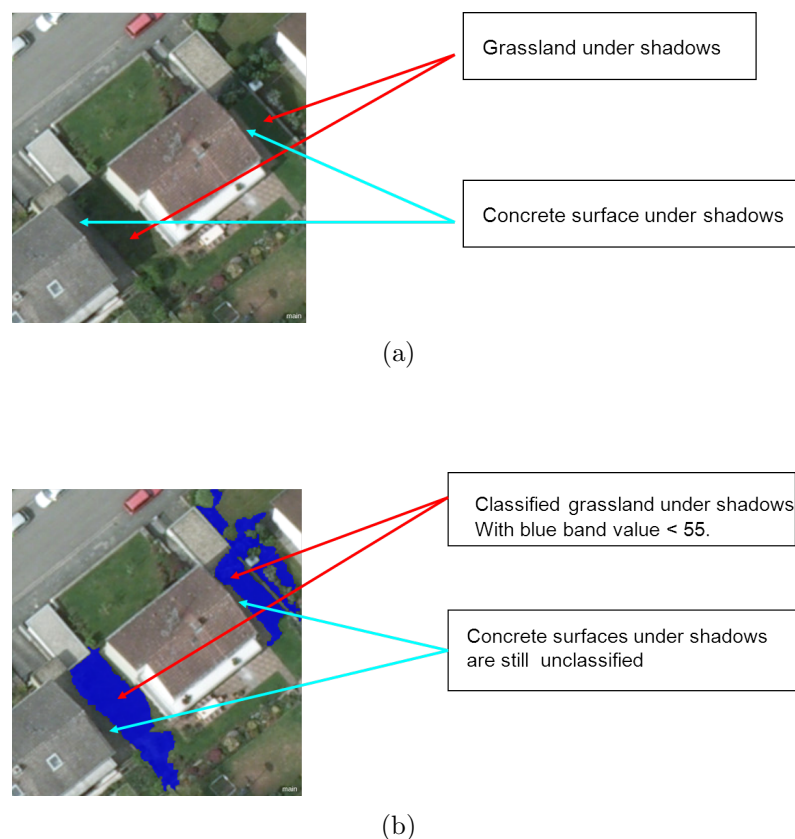


Figure 7.7: Detection of grasslands under the shadow: two types of surfaces, e.g. concrete and grassland under the shadow cast by the buildings (a); a threshold of the blue band value can separate the grassland from the concrete under the shadow (b).

The rule-set 2 in the Definiens environment is implemented and the output map captures all the impervious areas excluding those under the shadow. Figure 7.8(a) shows a subset of the study area featuring grasslands, impervious areas, cars and soft soils. It should be pointed out that cars are considered as impervious objects. Implementation of rule-set 2 classifies the cars and other concrete and asphalt surfaces exposed to the sun as impervious areas (Figure 7.8(b)). The employment of rule-set 2 cannot capture the impervious surface information under the shadow which is highlighted in Figure 7.8(b). In the third step, there is an attempt to classify the impervious areas under the shadow by using rule-set 3. Table 7.1 shows that rule-set 3 is designed to exploit the LiDAR intensity data to characterize the impervious areas under the shadow. Figure 7.9(a) shows a subset image with impervious areas under the shadow cast by the cars. Implementation of an expert system (rule-set 3) detects the impervious areas under the shadow (Figure 7.9(b)). The application of rule-set 3 also mistakenly includes dark exposed soils and some dark vegetation as shadows in Figure 7.9(b). The successive application of rule-set 2 and rule-set 3 can detect impervious surfaces exposed to the sun and impervious surfaces under the shadow respectively (Figure 7.9(c)). Figure 7.9(d) shows the classification of grasslands and impervious surfaces in the subset of the image. Bright exposed soils with thin slices are also classified as paved surfaces because of the spectral homogeneity.

7.2.7 Accuracy of the final map

All the rule-sets listed in Table 7.1 are applied sequentially. Figure 7.10 shows the entire study area with classified pervious and impervious surfaces. An accuracy assessment test is performed in order to validate the credibility of the knowledge-based rule-sets.

An error matrix approach is performed to assess the accuracy of the classified image. Two hundred randomly distributed points over the entire Alcatraz study area are generated. An aerial photo is taken as reference map and only the points that fall within the ROI (i.e. outside the thematic map) are considered. In this case, one hundred and twenty three points are found to be located on the ground. The overall

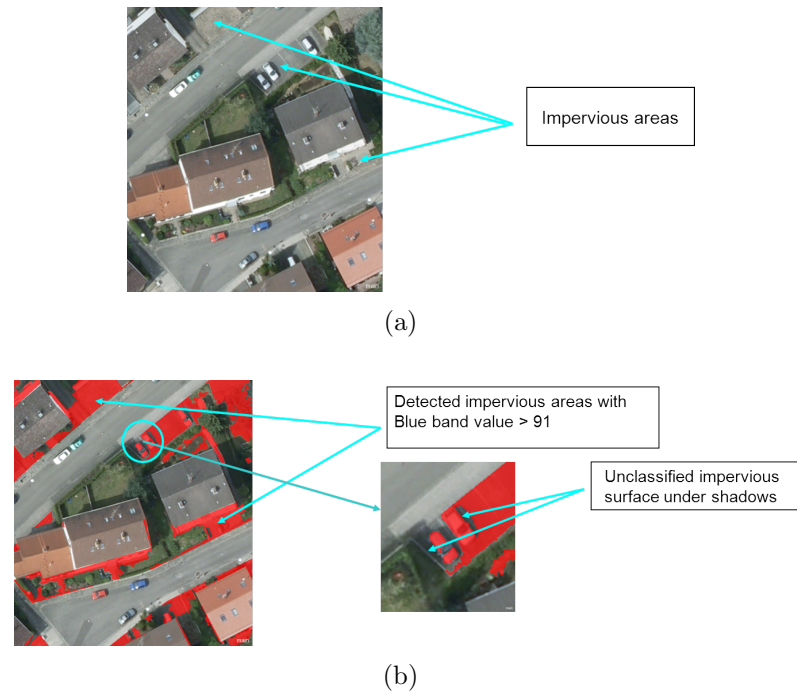


Figure 7.8: Detection of impervious areas: A subset of the study area featuring impervious areas and grasslands (a). Expert system rule-set 2 detects most of the impervious areas excluding shadow-covered impervious areas (highlighted by zooming in) (b).

accuracy computed from the error matrix is 94.3%. Table 7.2 shows the computed error matrix for the Alcatraz area. Pervious areas have errors of omission of 5.6% and errors of commission of 4.2% while impervious areas have errors of omission of 5.7% and errors of commission of 7.5%. Some areas of large trees with no leaves

Classified map	Reference map		
		Pervious	Impervious
	Pervious	67	3
	Impervious	4	49

Table 7.2: Error matrix calculation for verifying surface classification accuracy for Alcatraz area.

are visually found to have been classified as an impervious areas. A small patch of grassland with a partly yellow colour is also classified as a pervious area. This may result in misclassification in the classified map.

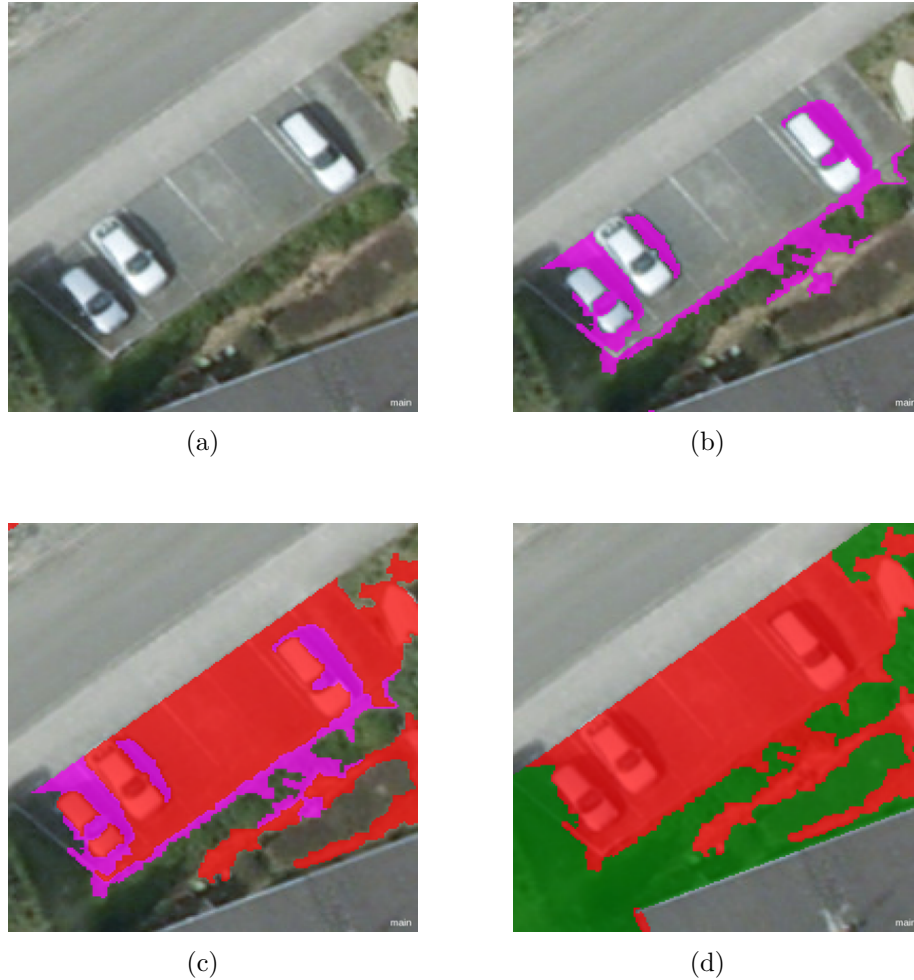


Figure 7.9: Classified maps after integrating different rule-sets: A subset image of the study area (a); detection of impervious areas under the shadows (b). Detection of impervious areas exposed to sun (in red) (c); resultant classification (d).

7.3 Application to Casimirring study area

This section describes the detection of pervious and impervious surfaces in the Casimirring area. This area has a higher scene complexity featuring a variety of roofs and dense trees compared to the Alcatraz area. An image masking technique using chessboard segmentation is applied in a similar way to that applied to the Alcatraz area (Section 7.2.2). The expert system rules which have been designed for the Alcatraz area are also applied to the Casimirring area. Table 7.1 in Section 7.2.5

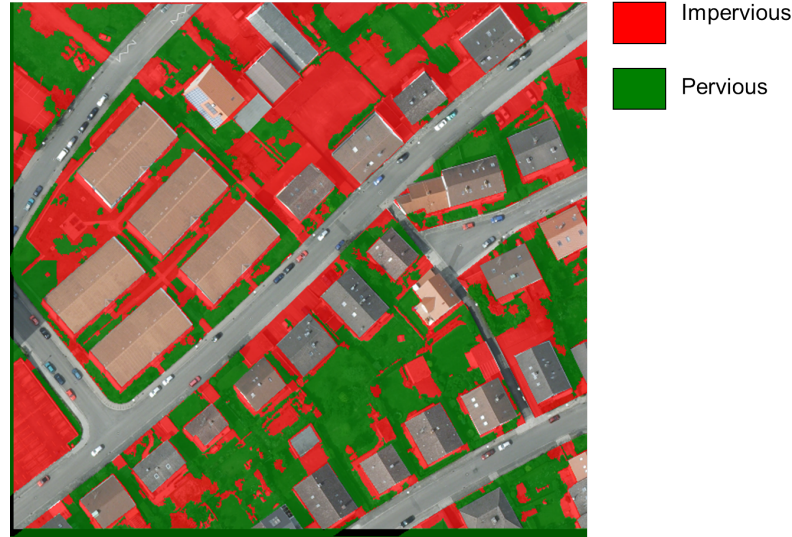


Figure 7.10: Detection of pervious and impervious areas in the Alcatraz dataset after masking out buildings and streets.

illustrates the expert system rules that have been designed for the Alcatraz area and which perform almost equally well for the Casimirring area. Figure 7.11(a) presents the aerial image of the Casimirring area (covering 50%) and Figure 7.11(b) shows the detected pervious (green) and impervious (red) surfaces of the same area using OBIA approach. The overall accuracy computed from the error matrix is reported to be 93.78%. Table 7.3 shows the computed error matrix of the Casimirring study area. Pervious areas have errors of omission of 6.7% and errors of commission of 4% while impervious areas have errors of omission of 5.4% and errors of commission of 9%. Some trees with reddish leaves are found to have been classified as imper-

Classified map	Reference map		
		Pervious	Impervious
	Pervious	96	4
	Impervious	7	70

Table 7.3: Error matrix calculation for verifying surface classification accuracy for Casimirring area.

vous surface. This misclassification deteriorates the expected level of accuracy in the Casimirring area to some extent when comparing to the Alcatraz area. Fig-

Figure 7.12(a) illustrates a small part of the Casimirring study area featuring a tree with reddish leaves. Because of the spectral similarity, the tree is classified as impervious surface when using the expert system rule 2 in Table 7.1 (Figure 7.12 (b)).



Figure 7.11: Pervious and impervious surface detection in the Casimirring area.



Figure 7.12: Trees with reddish leaves (a) are classified as impervious (b) surface.

7.4 Differentiating grassland and bare soil

This section presents the development of knowledge-based rule-sets capable of distinguishing grassland and bare soil as well as detecting impervious (paved) surfaces. The two study areas being investigated in this research do not have predominantly bare soil with the exception of soils partly covered by grass. However, the task of distinguishing between bare soil and grassland is important in order to describe the rainfall-runoff process more precisely. A newly built residential area at Harzhübel in the neighbourhood of the University of Kaiserslautern is chosen for this purpose. The Harzhübel study area has a large amount of exposed soils while the existence of grasses and other impervious surfaces are also noticeable. The OBIA techniques start with masking out the buildings and streets in the Harzhübel area by adopting the chessboard segmentation algorithm with the help of thematic maps. Afterwards, the rest of the ground and trees are taken as region of interest for further analysis. The first expert rule is developed by choosing a threshold value for the mean brightness of all the bands. With this threshold, most of the exposed bare soils and impervious areas near the houses can be separated out. An arithmetic formula calculating the difference between Red and Green bands is designed as a second expert rule in order to separate the impervious surfaces from the bare soils calculated by rule-set 1. The third expert rule detects the grassland by setting a threshold for the mean brightness band. Table 7.4 shows the expert system rules for the Harzhübel area. Figure 7.13 illustrates the implementation of rule-set 1. A small part of the study area with bare soils, grassland and other impervious surfaces is highlighted for the implementation of rule set 1 (Figure 7.13(a)).

	Expert systems rule	Surface types
Rule 1	Mean brightness value > 110	Bare soil + impervious surfaces
Rule 2	Red band - Green band < 0	Impervious surfaces
Rule 3	Mean brightness value < 90	Grass

Table 7.4: Expert systems rule-sets for Harzhübel study area.

A mean brightness value greater than 110 can separate the grassland from rest of the land cover types, mainly the bare soils and the impervious surfaces (Figure 7.13(b)). Although the application of rule-set 1 can distinguish the grassland from rest of

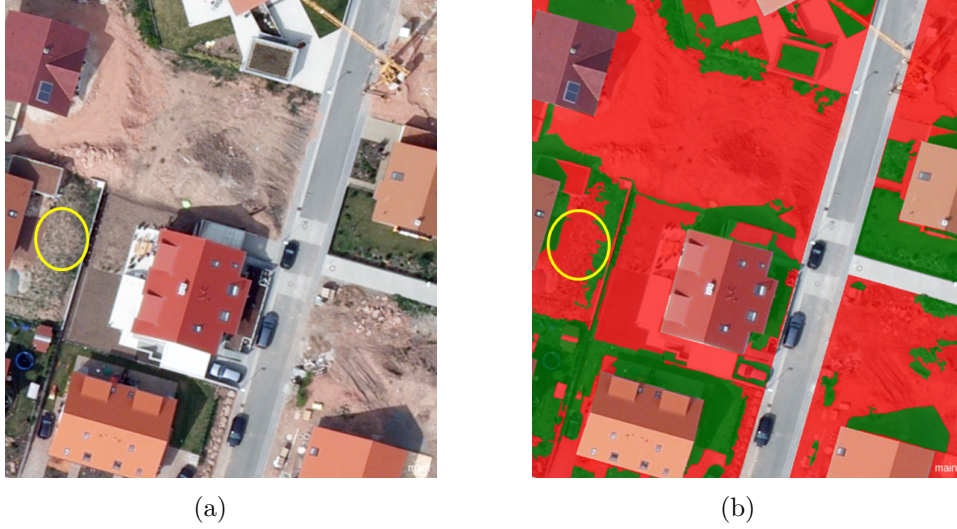


Figure 7.13: Aerial image with exposed soils (a) and classified image with soils + impervious surfaces (red) and grasses (green) (b).

the scene, a mix class of soil and grass with the later dominant is classified as bare soils. This mix class is highlighted by a yellow circle in Figure 7.13(a) and the resultant classification in Figure 7.13(b). In order to separate bare soils and impervious surfaces, rule-set 2 is implemented. Figure 7.14 shows the improvement in the classification after the application of second rule set. Figure 7.15 shows the classification of the entire Harzhübel study area after applying all the expert rules. In order to assess the quality of the classified image, an error matrix approach is taken as in the the previous examples. Table 7.5 illustrates the error matrix computation of the Harzhübel area. The overall accuracy is reported to be 94.4%. The errors of omission for the land classes grass, bare soil and impervious are found to be 4.76%, 3.57% and 11.11% respectively. The errors of commission of grass, bare soil and impervious surfaces are found to be 4.76%, 5.26% and 7.69% respectively.

7.5 Conclusion

The OBIA approach described in this chapter performs well for three different study areas with varied surface characteristics. The computed overall accuracy of the Al-



Figure 7.14: Aerial image with exposed soils, impervious surfaces and grasses (a) and classified image with soils (red), impervious (yellow) and grasses (b).

Classified map	Reference map			
		Grass	Bare soil	Impervious
Grass		40	1	1
Bare soil		1	54	2
Impervious		1	1	24

Table 7.5: Error matrix calculation for verifying surface classification accuracy for Harzhübel area.

catraz study area is 94.3%. Some trees partly covered with gray leaves are found to be classified as impervious areas which results in misclassifications in the output map. In the Casimirring study area, trees covered with reddish leaves are misclassified as impervious surfaces in the outputmap resulting in an overall accuracy of 93.78%. The accuracy of both areas can be increased significantly if the knowledge of the classified tree points (described in Chapter 5) can be linked to the OBIA approach. The computed accuracy of the Harzhübel area is reported to be 94.4% as some of the areas with bare soils under the shadow are classified as grassland. The incorporation of an additional expert rule by utilizing existing image wavebands is necessary to improve the accuracy for this site.

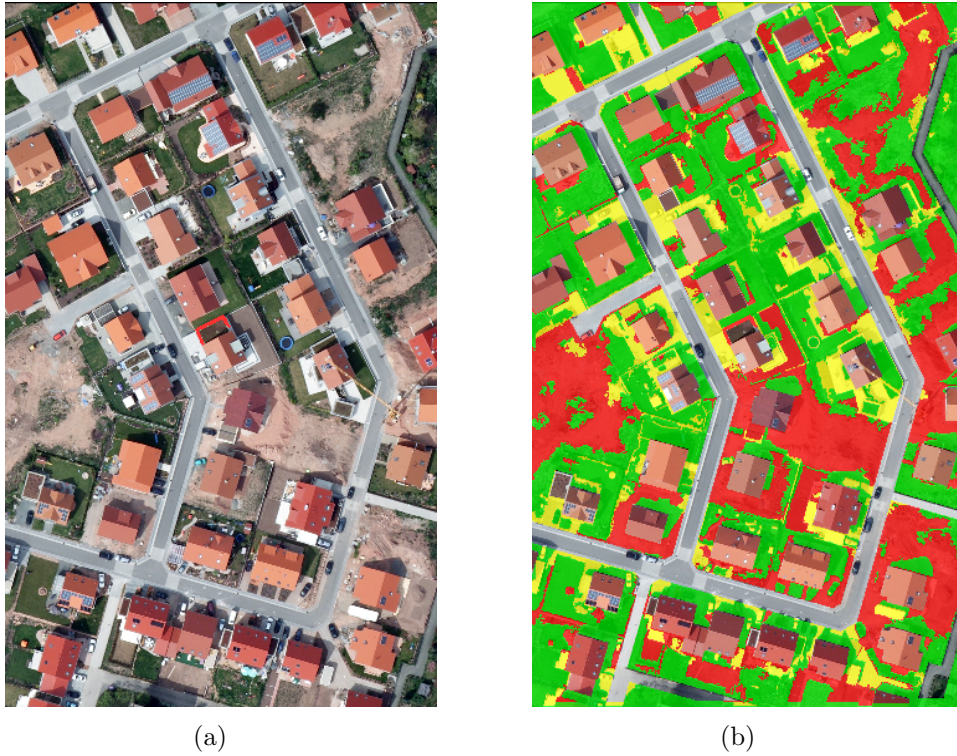


Figure 7.15: Aerial photo of the Harzhübel area (a) and the classified image after the application of OBIA approach (b).

The OBIA approach followed by the knowledge-based expert system is an effective way to classify high resolution aerial image in association with other ancillary data. The procedure of rule-set development is not completely automatic; rather, it is a semi-automatic system. The choice of a subset of an image to be analysed and the development of an expert system based on a user's visual observation may be attributed as 'human interaction', which will reduce the degree of automation. However, when classifying a masked image with the goal of detecting a few land classes from the whole study scene, this semi-automatic expert system is still a good choice to handle and classify very high resolution imagery in order to produce a highly accurate classified map.

Chapter 8

Resulting data model

8.1 Introduction

This section describes the integration of different topographic data layers. An integrated data model representing the topographic features such as buildings, streets and paved and unpaved surfaces is obligatory in order to run flood simulation. The topographic data layers provide the hydraulic and hydrologic input to a standard urban flood simulation model such as MIKE FLOOD. The resulting data model consists of two main components: DSM of the study area with elevation data and the land use and land cover (LULC) map of that area. The DSM of the urban catchment has three topographic layers in the form of point data:

- The classified buildings
- The extracted and modelled street network
- The rest of the ground (pervious and impervious)

The LULC map of any study site provides the information on the surface cover types of that area. In this study the LULC map contains the following information:

- The building polygon maps
- The street polygon maps

- Polygon maps of paved and unpaved surfaces

8.2 DSM generation

The integrated topographic model can be generated in raster grid format as well as triangulated format. However, most of the flood simulation models widely accept the raster format where the topographic information is provided as a fine-resolution grid. This study supplies the resulting topographic data model in raster (or grid) data format. Figure 8.1 illustrates the overall workflow of the DSM generation from LiDAR point data. The Alcatraz study area is taken as an example case in order to describe the step-by-step techniques for generating a complete DSM. The main goal of generating a DSM involves bringing together all three layers- the buildings, the street networks and the rest of the ground points into a single layer by merging them.

The first step is to single out the buildings from the classified non-ground points. Chapter 5 describes the detailed building and tree classification algorithm. The building points are stored and supplied as irregular point data with geographic coordinates x , y and z . In the second step, the modelled street network points with 3D geographic coordinates are merged with the building points. The merging operation is achieved through an array concatenating operation where each of x , y and z coordinates are considered as an array. Chapter 6 describes in great detail the extraction and modelling of a single-layer street network. In a similar way as a next step, the rest of the ground points are merged with the already combined building and street layers. Figure 8.2 illustrates the perspective view of the Alcatraz study area with buildings (red points), streets (blue points) and ground points (green).

However, the simulation of 2D overland flow using a standard software package such as MIKE 21 requires grid/raster representation of the topography. That is why, it is important to convert the irregular classified points into grid data. The conversion technique requires a specified rectangular grid size and the choice of an interpolation algorithm. The purpose of employing an interpolation algorithm in point cloud is to predict the elevation value at unsampled locations. A GIS software package such

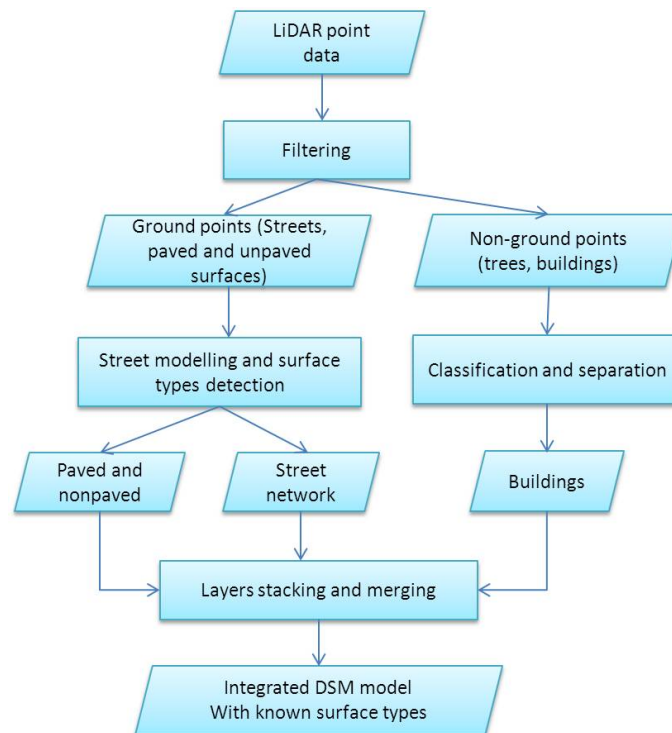


Figure 8.1: Workflow of DSM generation from LiDAR points.

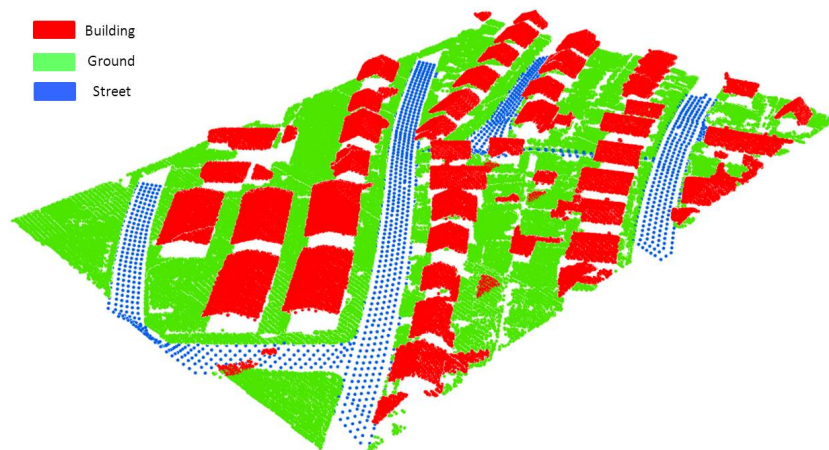


Figure 8.2: Perspective view of different topographic layers.

as ArcGIS offers a number of data conversion tools and interpolation algorithms. Although there are many algorithms available, the choice of an appropriate one is always application-oriented and requires the users to make trade-offs between

the desired accuracy and the computational efficiency. The basic principle of any interpolation algorithm is to assign a value to an unsampled location by looking at the neighbourhood information. The neighbourhood information may consider only the Euclidean distance (e.g., nearest-neighbour method) or other information such as spatial arrangement of the neighbouring points in addition to Euclidian distance (e.g., kriging, natural neighbour methods).

The application of a relatively simple method such as nearest-neighbour interpolation would be particularly attractive within the context of processing large point data acquired by LiDAR sensors. The arrangement of urban topography is highly heterogeneous with varying height profiles. Approximation of elevation data at the unsampled locations using a simple interpolation method may result in inconsistent values, especially along the edges of buildings and other man-made structures (Harman and Johns [58]). In this study, an advanced interpolation method such as natural-neighbour is used in order to exploit both the spatial and distance information for a point of interpolation. Sibson [117] first describes the idea of natural-neighbour interpolation. This method has a close association with Delaunay triangulation and Voronoi diagram. This is a piecewise method and takes into account the neighbouring point having a border with the Voronoi cell. The natural neighbour interpolation can be written as,

$$f(x) = \sum_{i=1}^n w_i(x) a_i \quad (8.1)$$

where $f(x)$ is the value of the interpolation at point x , n is the number of neighbouring points, $a_i (i = 1, 2, \dots, n)$ are the values of the neighbouring points, $w_i(x)$ are the weights for each neighbourhood point. Figure 8.3 illustrates the natural neighbour interpolation method by inserting a point x in the neighbourhood of P_i .

In this study, the spatial analysis toolbox of ArcGIS software package is used in order to convert the merged point cloud with three topographic layers into grid/raster data using the natural neighbour-interpolation method. A grid size of 0.25 m is specified for this purpose. Figure 8.4 illustrates the grid/raster representation of the Alcatraz study area where the dark pixels indicate lower elevation and the bright pixels indicate the higher elevation. In fact, this is the resultant data model in

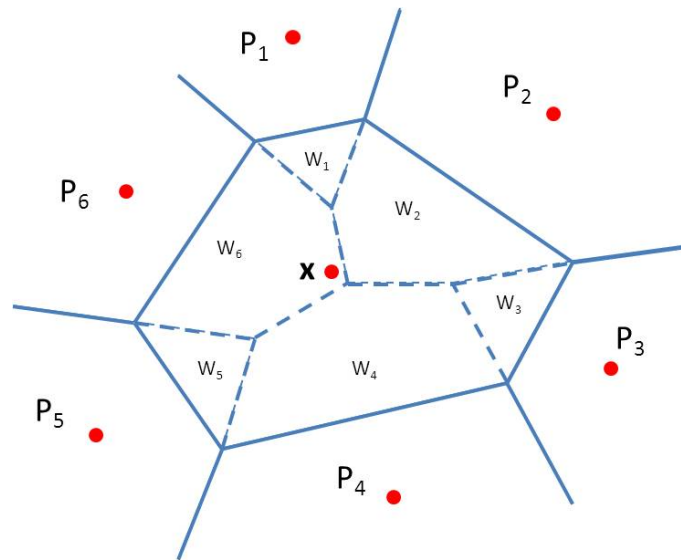


Figure 8.3: Schematic diagram of natural neighbour interpolation.

terms of describing the elevation data which MIKE 21 can take as input for the simulation of overland flow. This is the high resolution digital surface model which is capable of supporting modelling of urban flooding by providing detailed hydraulic representation of the urban topography.

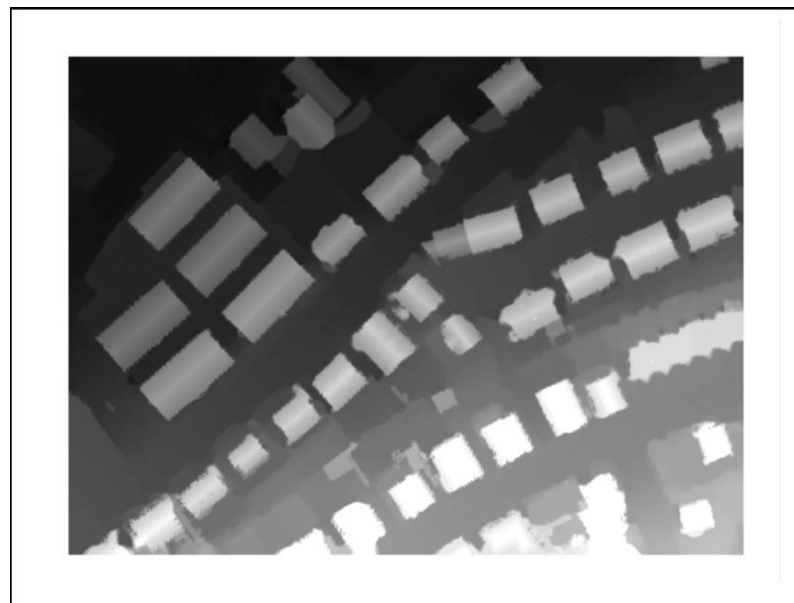


Figure 8.4: Grid/raster representation of the Alcatraz study area.

8.3 Qualitative assessment

The assessment of the overall quality of the resultant data model is important in order to achieve a higher degree of accuracy of the simulation results. In a built urban area, the spatial arrangement of the dense buildings often create narrow passages and alleys through and around them. Buildings next to the street sides and lying relatively lower than the street elevation are vulnerable to flood inundation. A realistic urban DSM should retain all these surface properties in order transfer the flood water into the private ground according to hydraulic conditions. As already described in Chapter 3 and 4, the topography of the Alcatraz area has a very steep slope running from S-W to N-E direction. A number of buildings are found to be lying lower than the street elevation and along the streets. In order to perform the qualitative assessment of the generated DSM of the Alcatraz area, a complex part of the study area featuring a narrow passage running between the buildings and connected to the streets is chosen. Figure 8.5 presents a small part within the Alcatraz area where a narrow roadway with steep slope runs down to private property from the main street. Figure 8.5(a) shows a yellow line drawn from the middle of the passage to the other end of the main street. The yellow line is spotted with points 1, 2, 3, 4, 5 and 6. Figure 8.5(b) shows the perspective view of the narrow passage looking up the streets. Figure 8.5(c) shows the DSM of the same part of the area shown in Figure 8.5(a). A cross-sectional profile is drawn on the DSM (Figure 8.5(c)) and along the highlighted yellow line (Figure 8.5(a)). Figure 8.5(d) illustrates the height profile indicating the location of the points (1, 2, 3, 4, 5 and 6) mentioned in Figure 8.5(a). From this example, it can be said that the quality of the interpolated DSM generated from the LiDAR point data closely correspond with the reality.

8.4 Preparing the land use and land cover (LULC) map

The LULC maps of different surface types in the Alcatraz study site are supplied in vector format which is also the meaningful input format for simulating the rainfall-

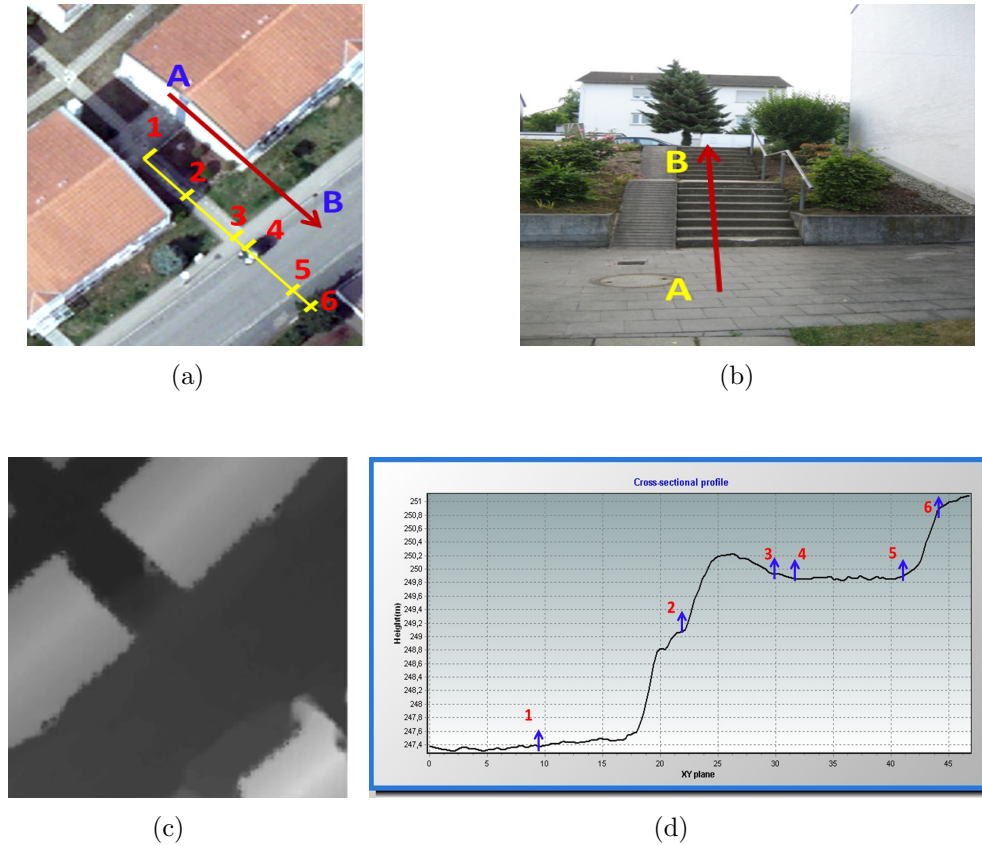


Figure 8.5: Qualitative assessment of the generated DSM.

runoff process using the MOUSE software package. At this stage, it is important to convert all types of surface data into vector/polygon format and merging among the layers is redundant as MOUSE offers the flexibility to import different surface types individually. Four types of urban surfaces are identified in this study for the Alcatraz study area. The street polygon maps are already available from the Stadt Kaiserslautern (city municipal office). The building polygon maps are produced from the classified building points described in Chapter 5. Chapter 7 discusses the methods of identifying pervious(paved) and impervious(unpaved) surfaces using Definiens software. The paved and unpaved surface types are exported as vector polygons from Definiens. Finally, the collection of four types of urban surfaces in vector formats is ready to be used in the runoff simulation software (Figure 8.6).

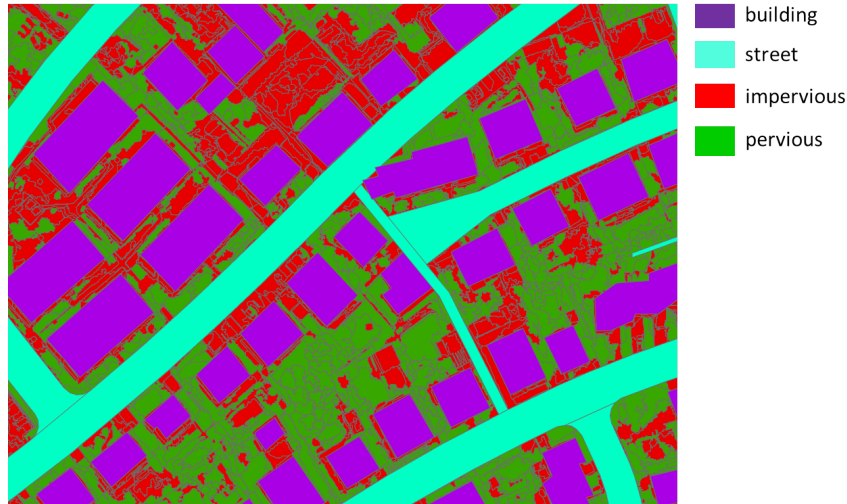


Figure 8.6: LULC map in vector format: buildings (maroon), streets (cyan), paved (red) and unpaved (green) surface.

8.5 Running the simulation

Flood modelling software MIKE FLOOD 2009, which is developed by DHI water, Environment & Health, Denmark, is taken as an established and recognized modelling platform in order to test the performance of the geospatial database of the two study sites in Kaiserslautern, Germany. The geospatial database mainly consists of fine resolution DSM processed from LiDAR data, modelled street network attached to the DSM and information about different urban surface types namely paved and unpaved. Modelling of urban flooding requires both the surface data for simulating overland flow and the sewer network data for pipe flow simulation. The context of urban flooding usually includes the urban topography and the underground sewer networks. An urban catchment can also be located on a river bank and can thus be vulnerable to river flooding. In this research work attention is paid only to pluvial flooding i.e. the urban flooding phenomena arising from the interaction between sewer flow and surface flow during torrential rainfall events. That is why, modelling of urban flooding takes full advantage of the modules MOUSE and MIKE 21 and their coupling.

8.5.1 MOUSE module

The MOUSE module of the MIKE FLOOD family offers the simulation of pipe flows of an urban storm drainage network. This section is devoted to the building of a simple MOUSE model using MIKE URBAN (MOUSE) interface. The complete model- building and simulation process can be grouped into the following steps:

1. Definition of the urban storm drainage network data
2. Delineation of the urban catchments
3. Declaration of the boundary conditions
4. Rainfall-runoff modelling
5. Sewer network flow simulation
6. Results and analysis

8.5.1.1 Sewer network data

The sewer network data are supplied in the form of nodes and links. The nodes represent the manholes whereas the links are the closed conduits/pipes connecting the manholes. MOUSE has a menu option for importing an Excel sheet with storm drainage network data. Figure 8.7 shows the layout of the drainage network with nodes and links in the Alcatraz study area.

Each manhole has a geographic location with X and Y coordinates, a ground level height and a bottom level height (i.e. inverted level). Each closed pipe/conduit connecting two manholes has a specified diameter and material property. Another important piece of information for a given pipe is its connectivity with the neighbouring two manholes which is supplied in the form of ‘From node’ and ‘To node’.

8.5.1.2 Delineation of the catchments

In rainfall-runoff modelling, the catchments act as a hydrological unit where the runoff and infiltration processes occur. The area of interest can be delineated as



Figure 8.7: Setup of MOUSE nodes and links of Alcatraz study area.

a single catchment in the first step. This catchment can be further divided into several sub-catchments depending on the definition of local valleys and ridges. One rule of thumb is to discretize the whole catchment in such a way that each sub-catchment contains at least one manhole node. The delineation of the catchment unit followed by its sub-division can be achieved either manually or automatically using the MOUSE module. Figure 8.8 illustrates the delineation of the catchment and sub-catchments of the Alcatraz study area. Each sub-catchment is connected to the manholes in order to transfer the runoff volume as inflow to the drainage network.

8.5.1.3 Declaration of the boundary conditions

In any numerical simulation, boundary conditions influence the result of the simulation. The choice of proper sets of boundary conditions can ensure consistency between the simulated results and the real-world physical processes. Boundary con-

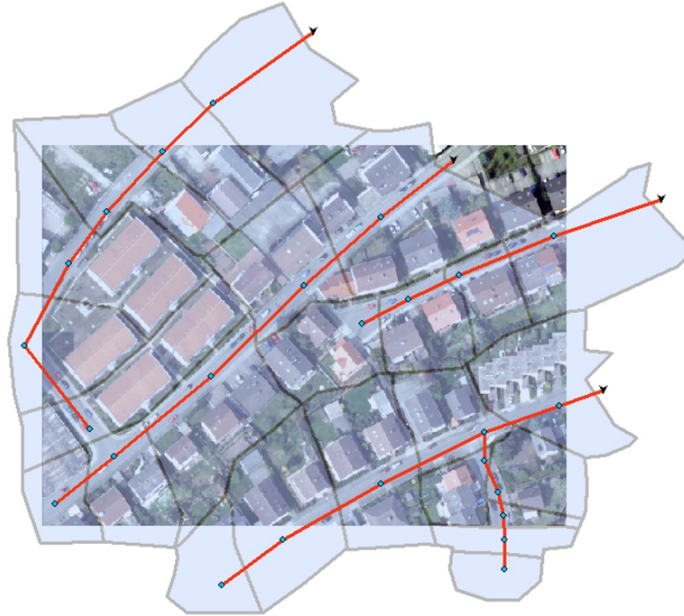


Figure 8.8: Delineation of catchment and sub-catchments of the region of interest.

ditions are also important in order to solve the flow equations for a given pipe connected to two manholes for each time step (MOUSE reference manual [149]). The MOUSE module offers three types of boundary conditions: rainfall, network loads and external water level. In this study, only the rainfall boundary condition is applied as a storm event over the catchment. Figure 8.9 shows the rainfall data used for computing the rainfall-runoff model for both study areas.

8.5.1.4 Surface runoff (hydrological) modelling

The amount of runoff for a given rainfall data can be modeled using an appropriate hydrological model. The main function of a hydrological model is to improve the understanding of surface runoff behaviour in a complex watershed. A surface runoff model is influenced by soil types, topography and rainfall data. The conversion of precipitation into effective runoff for a given urban catchment is necessary for computing the network loads of the urban storm drainage networks. MOUSE offers a number of surface runoff models for this purpose. The following surface runoff models are included in MOUSE:

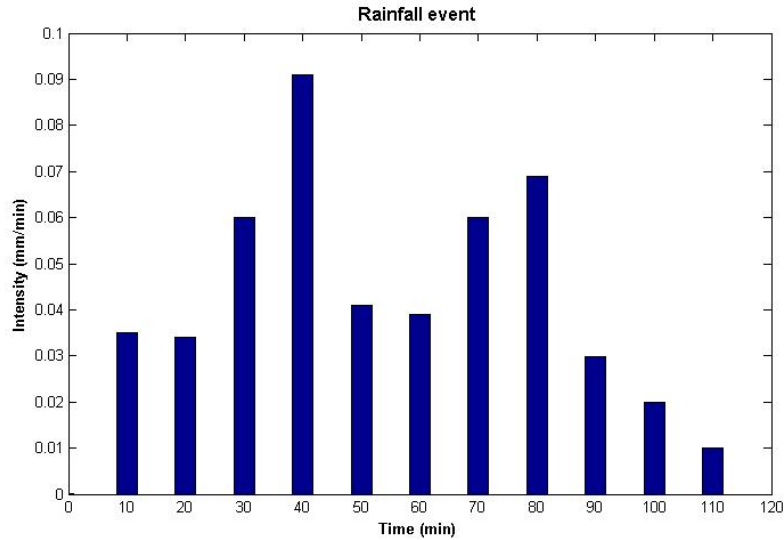


Figure 8.9: The rainfall data used for the flood simulation.

1. Time-Area method (A)
2. Kinematic Wave (B)
3. Linear reservoir (C1 and C2)
4. Unit hydrograph method (UHM)

In this study the Time-Area method (A) is used for the purpose of surface runoff modelling. This is a simple method and the runoff computation is performed by considering the hydrological losses and the runoff routing with the help of a time-area curve (MOUSE reference manual [149]). A time-area curve is actually a graph indicating the parts of a watershed responsible for generating direct runoff at a specific point of interest (Her [62]). This curve is generally constructed by calculating the cumulative travel time map and used to convert precipitation into a runoff hydrograph. This conversion of precipitation into runoff is often dominated by the physical characteristics of the watershed such as roughness, shape and slope (Her [62]). The runoff simulation can be initiated from the MOUSE simulation menu. The surface runoff model generates the catchment loads for storm drainage networks that are saved as *.CRF file in MOUSE environment.

8.5.1.5 Network flow simulation

The catchment load calculated from rainfall-runoff modelling acts as input to the MOUSE pipe flow model. The network parameters such as simulation mode and model type are set to normal mode and dynamic wave type respectively. Users have the flexibility to select the desired output results after running the network simulation. The depth and discharge at nodes, links and grids can be selected from the dialog ‘computation’ and under the tab ‘network summary’.

8.5.2 MIKE 21 module

The MIKE 21 module offers the advantage of modelling 2D overland flow thus making it feasible to visualize the realistic flood water propagation. The main input of the MIKE 21 module is a DSM/DTM describing the elevation data of a given topography. In Section 8.2 of this chapter, the steps for generating fine resolution DSM of the Alcatraz study area have been described. In fact, this grid format DSM is the ideal basement for running the 2D simulation. MIKE URBAN interface provides access to both MOUSE and MIKE 21 modules and interaction between these modules can also be implemented through this interface. Figure 8.10 presents a dialog box designed to facilitate the import of DSM and definition of the model domain.

After importing the DSM, it is important to define the 2D model parameters such as land value, flooding and drying depth and bed resistance. The land value is set to the maximum DSM value plus 10m above which no flood occurs. In MIKE 21 2D flow simulation, the flooding and drying depths influence the interplay of the DSM grid cells in the computation. Flooding and drying depth of 0.003 and 0.002 respectively are chosen for this study.

8.5.3 Coupling 1D and 2D flow

The coupling of 1D pipe flow and 2D overland flow can be achieved using MIKE URBAN interface. The user has options to choose a list of nodes to be coupled with

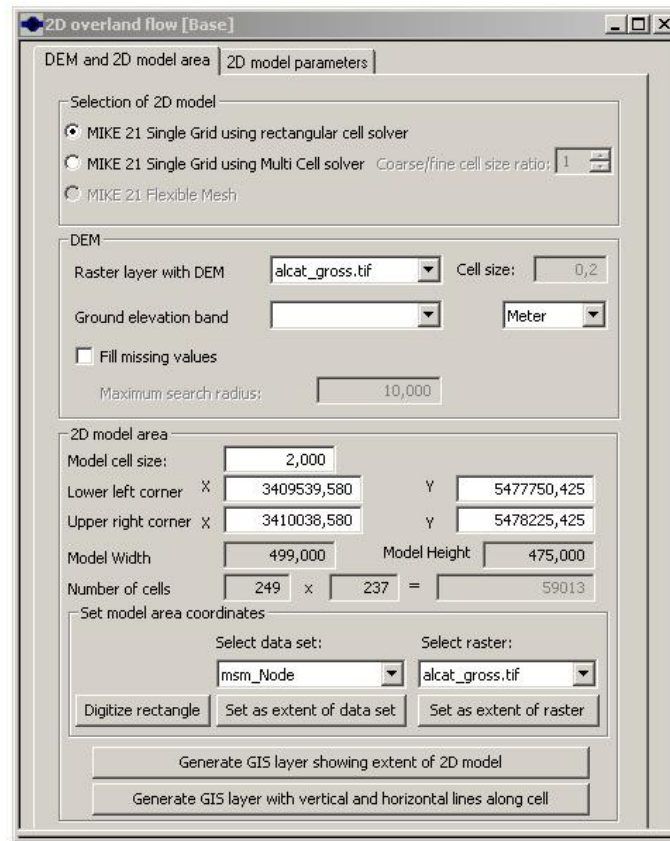


Figure 8.10: Importing DSM and selection of model domain.

the DSM. However, in this study, all the manhole nodes are considered to be coupled with the fine resolution DSM of the Alcatraz study area. Thus the implementation of the coupling between MOUSE and MIKE 21 modules facilitates the simulation of bi-directional flow which has its roots in adopting the dual-drainage modelling concept (Djordjević et al. [35]). Figure 8.11 illustrates a list of three nodes N1, N2 and N3 highlighted by square grids after being coupled with the DSM.

8.5.4 Simulation and results

After the declaration of the coupling between the nodes and the surface model, it is necessary to define the simulation type and the 2D overland flow parameters. At first the simulation type is specified as 'Network + 2D overland' from the general tab

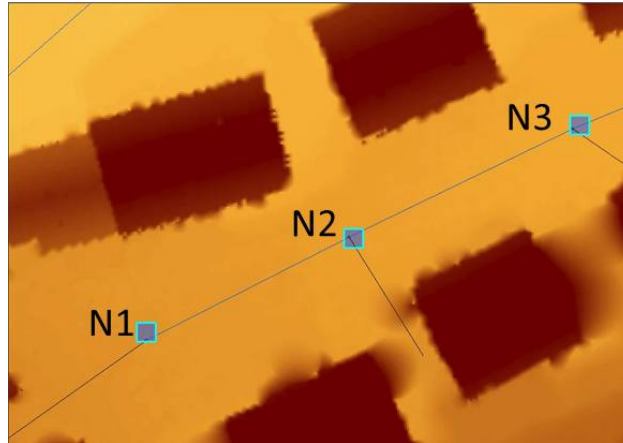


Figure 8.11: Coupling between the nodes and the surface model.

under the computation dialog. Under the tab ‘2D overland parameters’, the time step is set to 1.00 second and a desired output file name is specified. The results of the coupled 1D-2D flow simulations are generated as raster files with the extension *.dfs2 by MIKE URBAN. The *.dfs2 files are actually equivalent to the ESRI raster file. At the end of the simulation, there are two raster files: one with single time step characterizing maximum flood depths and the other containing information on flood depths for multiple time-steps. Figure 8.12 presents the flood simulation results for four different time periods. Figure 8.12(a) shows the flood inundation situation before the simulation starts. At the 5th time step, flood water comes out of the sewer system through the outlets (Figure 8.12(b)). The depth of flood water keeps increasing in the downstream and flood water starts to travel upstream in the 22th time step (Figure 8.12(c)). At the end of the simulation, flood water inundates part of the streets (Figure 8.12(d)).

The incident of street flooding can be seen downstream of the catchment. No localized street flooding can be seen because of the steep terrain characteristics of the area. The building highlighted by a red circle is vulnerable to urban flooding as water escapes from the street and runs into the private ground (Figure 8.12(d)). Figure 8.13 illustrates the close view of the flood affected building. This figure also explains the reason why the water enters into private ground by referring to a narrow passage next to the building in the aerial image.

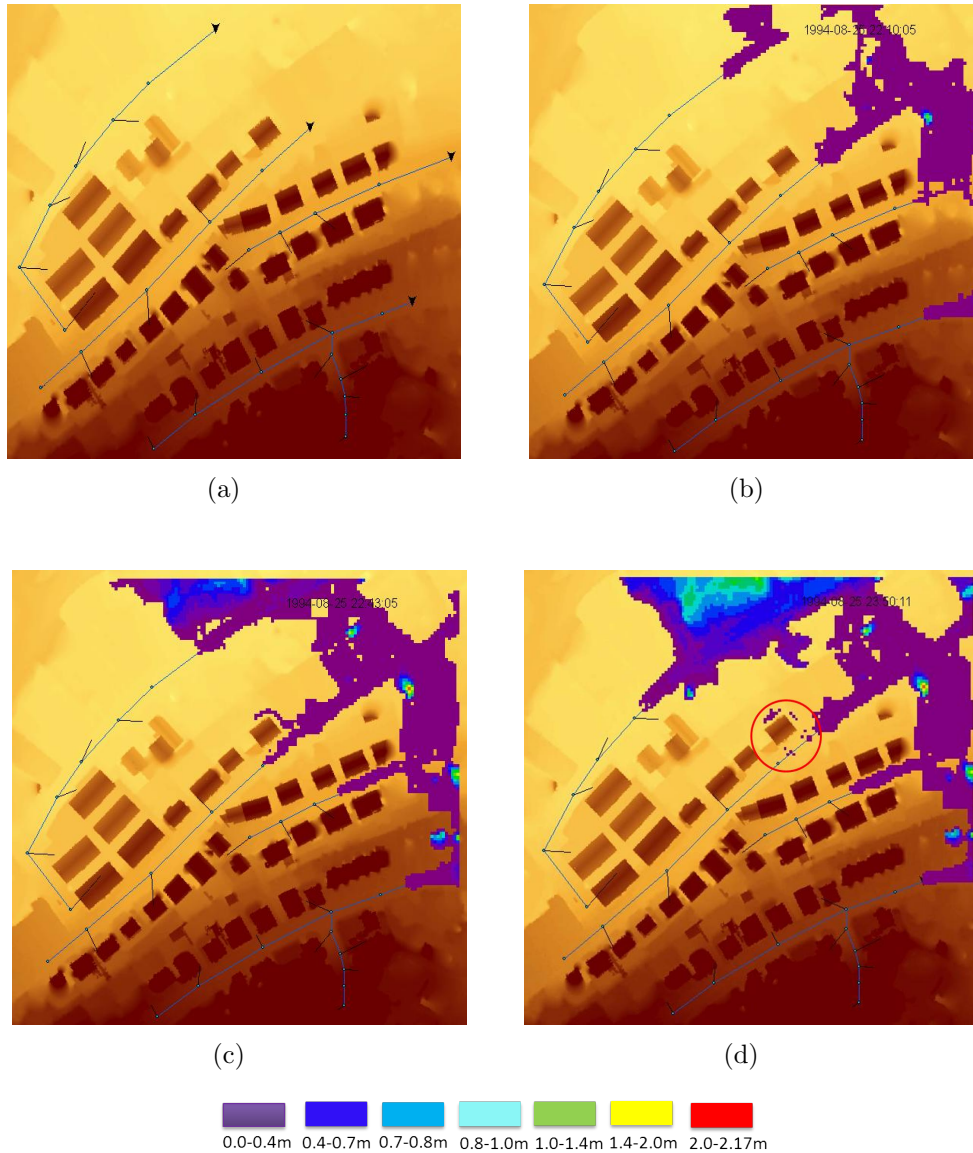


Figure 8.12: Extent of flood inundation at four different simulation stages (Alcatraz study area).

8.6 Application to Casimirring study area

The flood simulation model is also run for the Casimirring study area. The preparation of fine resolution DSM and LULC maps for Casimirring is similar to that of Alcatraz area as described in Section 8.2 and 8.4 respectively. Figure 8.14(a)



Figure 8.13: Flood water escaping into private ground from the street.

presents the fine resolution DSM (0.25 m) of the Casimirring area and the main input for the hydraulic simulation module MIKE 21. Figure 8.14(b) shows the LULC maps of the same area as vector/polygon format with four distinct classes namely, building (yellow), street (cyan), pervious (green) and impervious (red) surfaces. The LULC maps are used as hydrologic input to the MOUSE module in order to run the rainfall-runoff simulation. In the next step, the setup of the sewer network is constructed in the Casimirring area and discretization of the catchment is performed in order to divide the whole catchment into smaller sub-catchments. Figure 8.15 shows the setup of sewer networks and discretization of the catchment in the Casimirring study area. Each of the sub-catchment is connected to a manhole enabling the computation of the network load.

The coupling between MOUSE and MIKE21 modules is achieved by following the steps described in Section 8.5.3 of this chapter for the Alcatraz area. At this point the model setup is ready and the simulation is run for the complete duration of the rainfall event i.e. one hour and fifty minutes. Figure 8.16 illustrates the results of the simulation at four different time steps. Figure 8.16(a) illustrates the flood inundation situation before the simulation starts. At the 10th time step, flood water comes out of the sewer system through the outlets and also from the manhole at the center of the study area (Figure 8.16(b)). The depth of flood water keeps increasing on the streets and in the neighbourhood of the outlets in the 30th time step (Figure 8.16(c)).

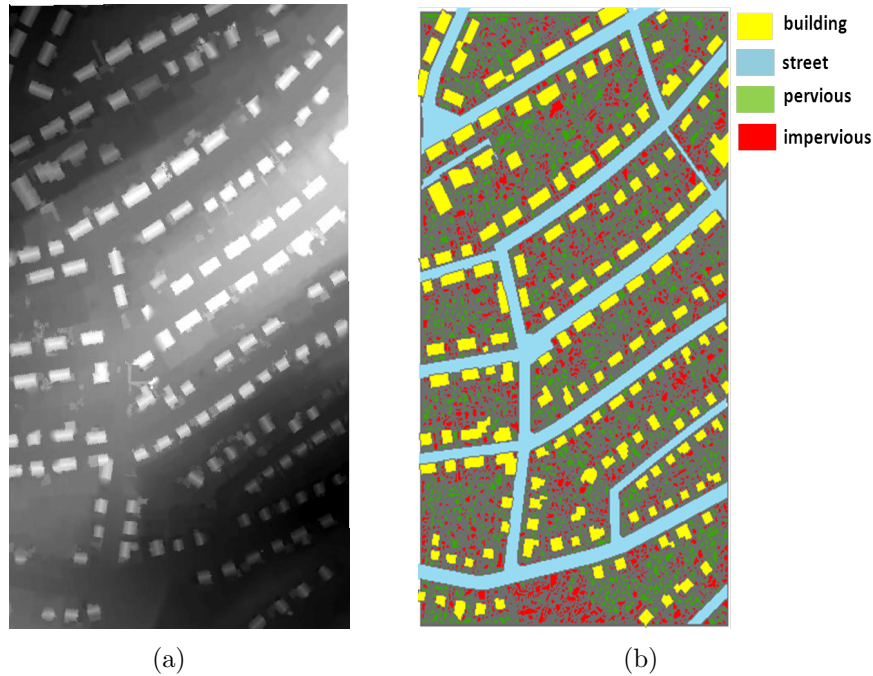


Figure 8.14: The interpolated DSM (a) and land cover maps of the Casimirring area.

At the end of the simulation, flood water inundates many parts of the Casimirring study area including streets and private grounds (Figure 8.16(d)).

A street segment chosen from the North-Western part of the flood inundation map (Figure 8.16(d)) shows clear evidence of street flooding. Figure 8.17(a) presents the enlarged view of the flood affected street AB and S is a location on the street. Figure 8.17(b) shows the perspective view of the street segment AB in the real-world highlighting the location of S with red arrow. The street running from point A to B bears a clear evidence of steep slope.

8.7 Summary

The resultant data model derived from LiDAR and other ancillary datasets could effectively be fed into the MIKE FLOOD software. The high resolution DSMs for both the study areas provide realistic hydraulic capacity of the urban drainage systems



Figure 8.15: Setup of sewer networks and discretization of catchment of the Casimir-ring area.

leading to the successful implementation of 1D-2D flow simulation. The qualitative assessment of the interpolated DSMs is performed by drawing cross-sectional profiles at locations where the topography is complex. Although the cross-sectional profiles show good agreement with the real-world topography, further investigation in terms quantitative measures should be performed in order to estimate the uncertainties pertaining to height profiles of the interpolated DSMs. The results of the flood inundation map for both the study areas show good correspondence with the respective topographic profiles. Different rainfall data and other boundary conditions should be considered in order to visualize multiple flood inundation scenarios for both the study areas.

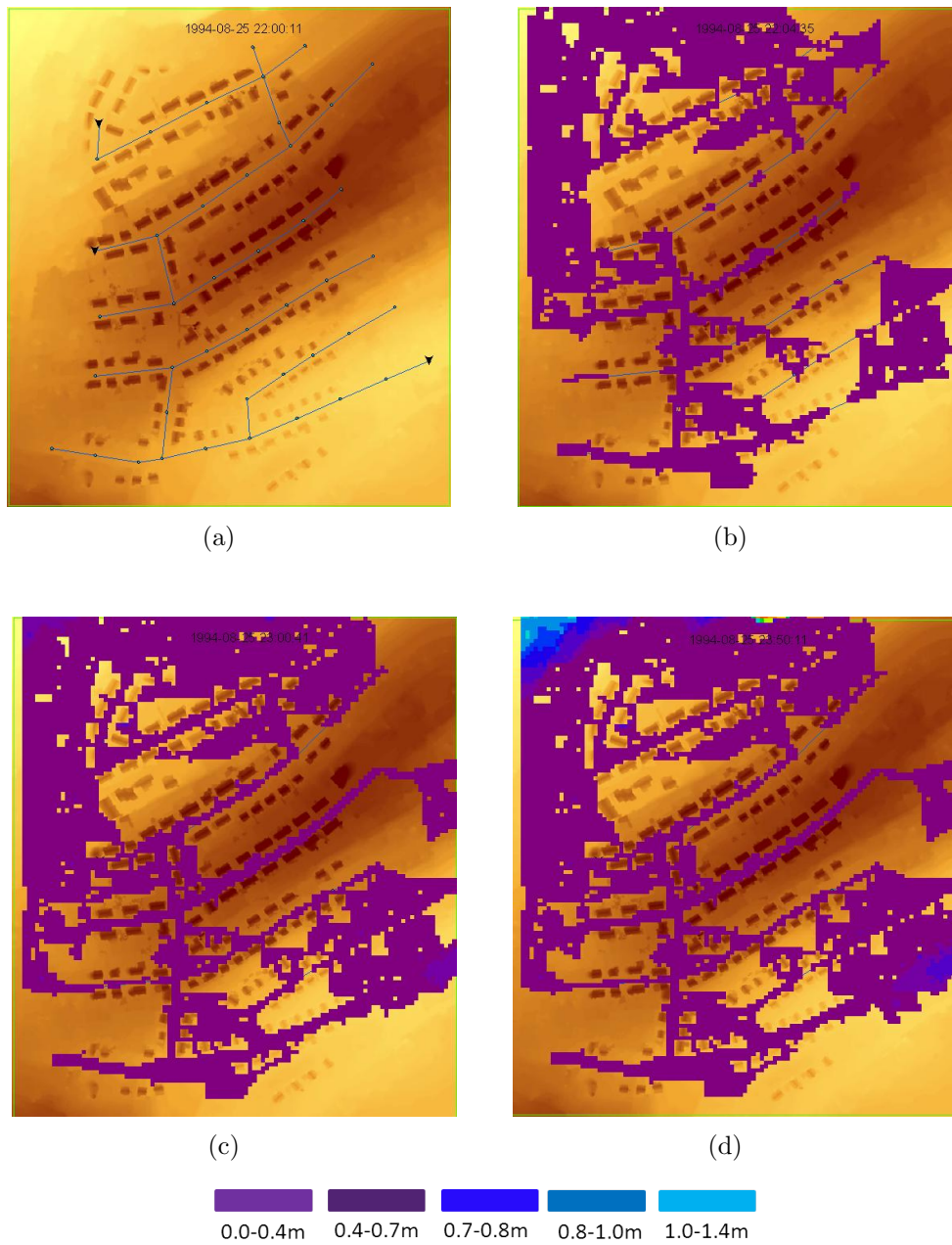


Figure 8.16: Results of the flood simulation in the Casimirring area at four different stages.

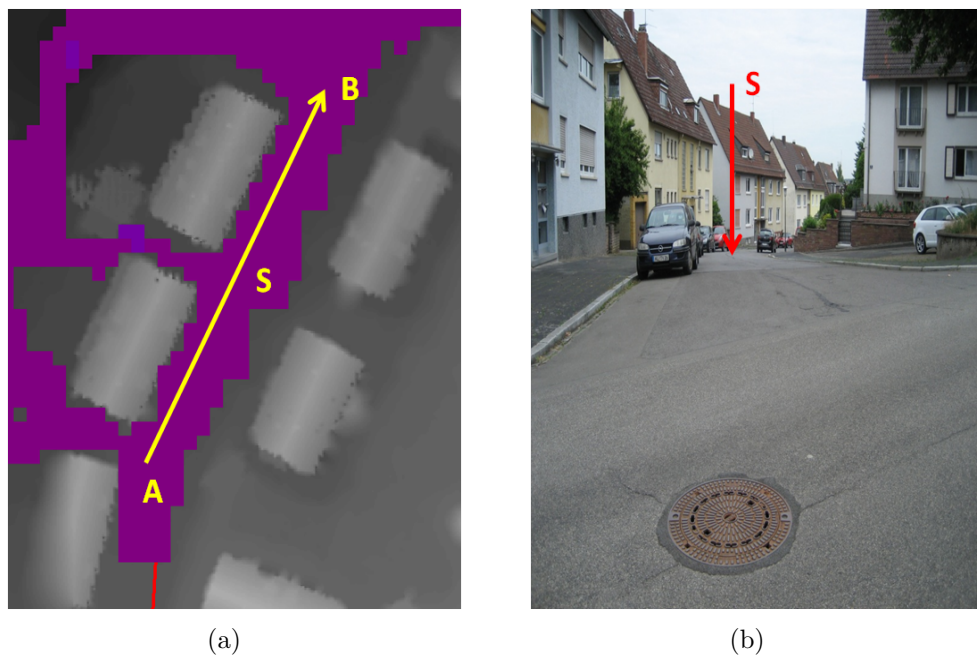


Figure 8.17: Event of flooding in one of the streets in Casimirring area (a) and the aerial image of that street (b).

Chapter 9

Summary and recommendations

9.1 Summary

The main objectives of this research are: 1) to provide a suitable database for 2D surface flow modelling using 1D-2D dual drainage approach, 2) to achieve higher degree of automation in terms of unstructured LiDAR data processing, 3) to explore the suitability of using aerial images and topographic maps for improving the overall performance of urban drainage modelling and simulation and 4) to use the integrated database in a simulation model to assess the hydraulic performance of urban drainage systems. In the recent years, the choice of LiDAR derived DEM with varying spatial resolution has been well accepted in the urban flood modelling community. In order to achieve the first research objective, the use and processing of high-density and unstructured LiDAR point data have been documented in this research work. Pertaining to the second research objective, a number of LiDAR point data processing techniques have been proposed to extract, detect and model the complex urban surface characteristics. In order to achieve the third research objective, other ancillary data such as aerial images and topographic maps in combination with LiDAR data have been used to better model street networks and to detect various surface types. Pertaining to the last objective, an established flood model MIKE FLOOD has been used to visualize the flooding scenario using gen-

erated high resolution topographic database. The following subsections present the summary of the research work:

9.1.1 LiDAR data processing

This study presents an automatic filtering algorithm for separating LiDAR point data into ground and non-ground points. Filtering is the first step of LiDAR data processing. The proposed filtering algorithm works in the raw LiDAR point data in opposite to many existing morphological filtering algorithms working on the range image. One major problem of morphological filtering is the selection of an appropriate length of the structuring element. Morphological filtering involves the repetitive application of erosion, dilation, opening and closing operations. Conversely, the proposed filtering algorithm needs only two input parameters: 1) the window size and 2) user defined height threshold value. The window size should be larger than the length of the largest building present in the scene. The choice of a threshold value depends on the expected level of details in object extraction.

9.1.2 Object classification

The main objective of object classification i.e., to distinguish building and tree is to remove the trees from the DEM. This study presents two algorithms for classifying non-ground LiDAR point data as building and tree. The first proposed algorithm known as ‘pseudo-gridding’ is a simple and easy to implement algorithm that measures height texture of an object cluster and assign a class label to each grid depending on a threshold. This algorithm performs well (overall accuracy 96%) in Alcatraz dataset where there is a smaller number of trees and the building roofs are planar and without any occlusions. However, this algorithm performs relatively poor (overall accuracy 86.5%) in the Casimirring dataset where the topography is dominated by a large number of trees and the building roofs are rough due to the presence of chimneys and overhanging trees. This study also presents a robust classification algorithm known as ‘planar surface analysis’. This algorithm has two levels of hierarchy: 1) segmentation and 2) planarity check. The segmentation technique

is a region growing approach based on the geometric descriptor calculation. The second part of the algorithm checks the calculated eigenvalues of each segmented patch obtained in the previous step. Any segment having two dominant eigenvalues are labeled as ‘planar surface’ and subsequently classified as building. The non-planar surfaces are classified as trees. The complete implementation of the algorithm is automatic and the classification results achieved by this algorithm for both the study area are highly satisfactory (e.g., 97% for Alcatraz and 95% for Casimirring area).

9.1.3 3D street modelling

In dual-drainage model, whether it is a 1D-1D or 1D-2D approach, the street surface plays an important role in many ways. For example, the interaction between sewer and surface flow occurs on the street surface and flood water is routed downstream while flowing over the street. This study describes a detailed framework to detect streets and subsequently modelling and reconstructing street surfaces in an automatic way. The street extraction and modelling algorithm has six stages :1) street candidate point extraction from LiDAR point data 2) establish the road connectivity 3) detection of centerlines 4) delineate street kerbs within street boundary polygons and 5) reconstruct street surfaces by preserving continuities in slope and height and 6) model the junctions.

The Point-in-polygon (PIP) algorithm is used for extracting LiDAR point data enclosed by street polygons. The centreline of the complete street network is calculated by applying a skeletonization technique. This is a technique used in computer vision and pattern recognition for thinning down the shape of an object. Establishing street connectivity is important in three ways: 1) automatic detection of street junctions 2) automatic implementation of proposed rectangular blocks and 3) automatic modelling of street junctions. Street kerbs are delineated inside the street polygon boundaries by applying a Canny edge detection technique in the aerial image. Both study areas investigated in this research work do not exhibit significant kerb height. The Alcatraz area has kerb height of less than 3cm and many parts of the street do not have a kerb height at all. The Casimirring area presents a kerb height of less than 5cm and thus making the situation difficult to detect kerb height from LiDAR-

derived street cross-sectional profile. To overcome this problem, the height of kerb lines has been assigned by calculating the difference between the height of boundary lines and that of centerlines. The final stage describes the reconstruction of street surfaces. LiDAR points enclosed by any 2D street polygons are discrete in nature. These discrete points represent the information on the street surfaces as long as the street surfaces are not occluded by any vehicle or tree. A LiDAR sensor records the height of vehicles or trees instead of street surfaces when they (vehicles/trees) cover street surfaces. Thus the presence of a vehicle or a tree creates discontinuity in longitudinal as well as transverse profiles of a street segment. Removing those discontinuities leaves the occluded place without any LiDAR point. To fill in the missing information within the occluded street surface, a linear interpolation technique is applied.

9.1.4 Pervious (unpaved) and impervious (paved) surface detection

The volume of the surface runoff is heavily dependent on the percentages of impervious and pervious areas in the urban catchment area. So the detection of different types of urban surface is an important task for estimating the volume of stormwater runoff contributing to the storm sewer system. This study presents an object based image analysis (OBIA) technique to segment the image first and afterwards to apply the knowledge-based rule-sets in order to classify pervious and impervious area. The detection of different surface types for three study areas shows good correspondence with the reference map.

9.1.5 Resulting/integrated data model

This chapter describes the integration of three topographic layers: 1) the buildings; 2) the streets and 3) the rest of the terrain points (i.e., pervious and impervious areas) in order to generate fine resolution DSM featuring detailed urban surface characteristics. At this point the integrated data model is in point data format and requires to convert the data into grid/raster format for the purpose of running the

simulation. A natural-neighbour interpolation technique is chosen for converting the integrated data model into raster data. MIKE FLOOD software is used as a standard platform for the implementation of 1D-2D dual drainage concepts in order to evaluate the performance of the resultant data model. For a given rainfall data, the simulation is run for both the areas. Both the study areas show realistic surface flooding processes in relation to their respective topographic properties.

9.2 Recommendations / Future needs

The methods developed in this study seek to process unstructured and heterogeneous topographic data towards generating a high resolution DSM for urban flood modelling. The developed methods also offer higher degree of automation in terms of data processing, feature extraction and surface characterization for producing classified maps. In spite of the demonstrated validation, the developed methods show some weakness and limitations which lead to recommendations and future needs for further research work.

The efficiency of the LiDAR filtering algorithm in terms of micro object (i.e. boundary walls, fences and hedges) detection should be assessed in future research. For example, more dense urban study area should be chosen in order to evaluate the performance of the proposed filtering algorithm.

The proposed building and tree classification algorithms can be extended for addressing the problem of detecting building roofs with more than two planes. The proposed planar surface analysis algorithm performs inaccurately when dealing with a building roof having four equal planes. An efficient roof segmentation technique can be incorporated in the present algorithm.

The proposed street extraction algorithm is designed for single-layer street network. A multi-layer approach can be incorporated in the present system in order to model bridges and flyover.

The present study describes the detection of different types of urban land covers. In the first example, this study develops rule-sets for detecting impervious (e.g. asphalt, concrete) and pervious (e.g. grassland, bare soil) surfaces. In the second

example, this study develops rule-sets to detect grassland and bare soil separately along with impervious surfaces. However, this study does not propose a strategy to detect different types of impervious surfaces, e.g. paved and partially paved surfaces. In future, knowledge-based rule-sets can be developed for discriminating various impervious surface types.

The present study utilizes the promising OBIA (Object-based Image Analysis) technique in order to classify pervious and impervious surface from high resolution aerial image. However, the use of Definiens commercial software package may prove financially expensive. As a future effort, the popular multi-resolution segmentation technique can be implemented in MATLAB environment in order to replace the exclusive use of Definiens.

The conversion of LiDAR-derived DSM into raster/grid format requires implementation of an interpolation algorithm. During this conversion process loss of information to some degree propagates to the output data model as an inherent limitation of the interpolation techniques. Although the qualitative assessment of the generated DSM shows good agreement with the real world terrain profile, further quantitative assessment is needed to be carried out in future in order to quantify the uncertainties related to the height variation and continuity in slope.

Finally, the different outputs of the flood simulation model such as inundation depth and flow velocity should be measured for different fine resolution DEMs in order to choose optimal size of the raster grid.

Bibliography

- [1] A. F Abdullah, A. A. Rahman, and Z. Vojinovic. LiDAR Filtering Algorithms for Urban Flood Application: Review on Current Algorithms and Filter Tests. In *ISPRS Working Group III/2, Point Cloud Processing*, Paris, France, 2009.
- [2] S. Airault, O. Jamet, and F. Leymarie. From manual to automatic stereoplotting: Evaluation of different road network capture processes. *International Archives of Photogrammetry and Remote Sensing*, 31(B3):14–18, 1996.
- [3] A. O. Akan. *Urban Stormwater Hydrology*. Technomic publishing company Inc., 1993.
- [4] M. Aktaruzzaman and T. G. Schmitt. LiDAR Data: Automatic Object Detection to Support Urban Flooding Simulation. In *Proceedings Canadian Geomatics Conference and ISPRS Symposium I*, Calgary, Canada, 2010.
- [5] M. Aktaruzzaman and T. G. Schmitt. Filtering of LiDAR data in order to support modelling of Urban Flooding. *Journal of Urban Technology*, Accepted, 2011.
- [6] A. Alharthy and J. Bethel. Heuristic filtering and 3D feature extraction from LiDAR data. In *The International Archives of the Photogrammetry, Remote Sensing and Spatial Information Sciences*, volume XXXIV, pages 29–34, Graz, Austria, 2002.
- [7] F. Ameri, A. M. Mobaraki, and M. J. Valadan Zoej. Semi-automatic extraction of different-shaped road centrelines from MS and Pan-sharpened IKONOS images. In *The International Archives of the Photogrammetry, Remote Sensing and Spatial Information Sciences*, volume XXXVII, Beijing, 2008.
- [8] D. E Anderson and P. N. Anderson. Population estimates by human and machines. *Photogrammetric Engineering*, 39:147–154, 1973.
- [9] J. R. Anderson, E. Hardy, J. Roach, and R. Winter. A land use and land cover classification system for use with remote sensor data. In *Geological*

- survey professional paper*, volume 964, Washington: US Government Printing office., 1976.
- [10] P. Axelsson. DEM Generation from Laser Scanner Data using adaptive TIN models. *IAPRS*, 33(B4/1):110–117, 2000.
 - [11] M. Baatz and A. Schape. Multiresolution segmentation: An optimization approach for high-quality multi-scale image segmentation. In *Strobl, L. J., Blaschke T. and Griesebener T. (Eds.), Angewandte geographische informationsverarbeitung, Beitrag zum AGIT Symposium Salzburg*, volume XII, pages 12–13, Herbert Wichmann Verlag, Heidelberg, 2000.
 - [12] E. Baltsavias. A comparison between photogrammetry and laser scanning. *ISPRS Journal of Photogrammetry & Remote Sensing*, 54(2-3):83–94, 1999.
 - [13] M. Bartels and H. Wei. DTM Generation from LiDAR data using Skewness Balancing. In *18th International Conference on Pattern Recognition*, 2006.
 - [14] M. Bartels and H. Wei. Threshold-free object and ground point separation in LiDAR data. *Pattern Recognition Letters*, 31:1089–1099, 2010.
 - [15] P. D. Bates, K. J. Marks, and M. S. Horitt. Optimal use of high-resolution topographic data in flood inundation models. *Hydrological Processes*, 17:537–557, 2003.
 - [16] W. A. Bishop, N. I. Collins, D. P. Callaghanand, and S. Q. Clark. Detailed Two Dimensional Flood Modelling of Urban Developments. In *Proceedings, 8th International Conference on Urban Storm Drainage*, Sydney, Australia, 1999.
 - [17] S. Boonya-Aroonnet, C. Maksimovic, D. Prodanovic, and S. Djordjevic. 2007. Urban pluvial flooding: Development of GIS based pathways model for surface flooding and interface with surcharged sewer model. , pp. 481-488, Lyon, France. In *Proceedings of the 6th NOVATECH international conference*, pages 481–488, Lyon, France, 2007.
 - [18] M. Brovelli, M. Cannata, and U. Longoni. Lidar data filtering and DTM interpolation within grass. *Transactions in GIS*, 8(2):155–174, 2004.
 - [19] M. Carlberg, P. Gao, G. Chen, and A. Zakhor. Classifying urban landscape in aerial lidar using 3d shape analysis. In *Image Processing (ICIP), 2009 16th IEEE International Conference on*, pages 1701 –1704, 2009.

- [20] R. S. Carr and G. P. Smith. Linking of 2D and pipe hydraulic models at fine spatial scales. In *7th International Conference on Urban Drainage Modelling and 4th International Conference on Water Sensitive Urban Design, Melbourne*, Melbourne, 2006.
- [21] H. Chanson. *Hydraulics of Open Channel Flow: An Introduction*. Second edition edition, 2004.
- [22] A. P. Charaniya, R. Manduchi, and S. K. Lodha. Supervised parametric classification of aerial LiDAR data. In *IEEE Conference on Computer vision and Pattern recognition Workshop*, 2004.
- [23] A. Chen, S. Djordjević, J. Leandro, and D. Savić. The Urban inundation model with bidirectional flow interaction between 2D overland surface and 1D sewer networks. In *NOVATECH 2007 - 6th International Conference on Sustainable Techniques and Strategies in Urban Water Management, 25th to 28th June*, Lyon, France, 2007.
- [24] A. S. Chen, M. H. Hsu, T. S. Chen, and T. J. Chang. An integrated Inundation model for highly developed urban areas. *Water Science and Technology*, 51(2):221–229, 2005.
- [25] G. Chen and A. Zakhor. 2D tree detection in large urban landscape using aerial LiDAR data. In *Proceeding ICIP'09 Proceedings of the 16th IEEE international conference on Image processing*, Cairo, Egypt, 2009.
- [26] L. C. Chen and C. Y. Lo. 3D Road Modeling Via the Integration of Large-Scale Topomaps and Airborne LIDAR Data. *Journal of the Chinese Institute of Engineers*, 32(6):811–823, 2009.
- [27] Q. Chen. Airborne LiDAR data processing and information extraction. *Photogrammetric Engineering and Remote Sensing*, 73:109–112, 2007.
- [28] W. Cho, Y. Jwa, H. Chang, and S. Lee. Pseudo-grid-based building extraction using airborne LiDAR data. In *20th ISPRS Congress*, Istanbul, 2004.
- [29] S. Clode, P. Kootsookos, and F. Rottensteiner. The Automatic Extraction of Roads from LiDAR Data. *IAPRSIS*, XXXV(B3):231–236, 2004.
- [30] A. M Dean and G. M Smith. An evaluation of per-parcel land cover mapping using maximum likelihood class probabilities. *International Journal of remote sensing*, 24:2905–2920, 2003.

- [31] A. Dehvari and R. J. Heck. Comparison of object-based and pixel-based infrared airborne image classification methods using DEM thematic layer. *Journal of geography and regional planning*, 2(4):86–96, 2009.
- [32] N. Demir and E. Battsavias. Combination of Image and LiDAR data for building and tree extraction. In *Paparoditis N., Pierrot-Deseilligny M., Tournaire O. (eds), IAPRS*, volume XXXVII, Saint-Mandé, France, 2010.
- [33] A. K. Dey and S. Kamioka. An integrated modeling approach to predict flooding on urban basin. *Water Science and Technology*, 55(4):19–29, 2007.
- [34] G. Dial, L. Gibson, and R. Poulsen. IKONOS imagery and its use in automated road extraction. In *Baltsavias, E.P., Gruen, A., Van Gool, L. (Eds.), Automatic Extraction of Man-Made Objects from Aerial and Space Images (III)*, Zurich, Dillabaugh, 2001.
- [35] S. Djordjević, D. Prodanović, and Ć. Maksimović. An approach to simulation of dual drainage. *Water Science and Technology*, 39(9):95–103, 1999.
- [36] S. Djordjević, D. Prodanović, Ć. Maksimović, M. Ivetić, and D. Savić. SIPSON – Simulation of Interaction between Pipe flow and Surface Overland flow in Networks. *Water Science and Technology*, 52(5):275–283, 2005.
- [37] P. Dorninger and C. Nothegger. 3D segmentation of unstructured point clouds for building modelling. In *PIA07-Photogrammetric Image Analysis*, Munich, Germany, 2007.
- [38] S. M. Easa, H. Dong, and J. Li. Use of Satellite Imagery for Establishing Road Horizontal Alignments. *Journal of Surveying Engineering*, 133(1):29–35, 2007.
- [39] S. Oude Elberink and H. G. Maas. The use of anisotropic height texture measures for the segmentation of airborne laser scanner data. In *International Archives of Photogrammetry and Remote Sensing*, volume XXXIII, pages 678–684, Amsterdam, The Netherlands, 2000.
- [40] S. Oude Elberink and G. Vosselman. Adding the third dimension to a Topographic Database Using Airborne Laser Scanner Data. *International Archives of Photogrammetry, Remote Sensing and Spatial Information Sciences*, 36(3):92–97, 2006.
- [41] S. Oude Elberink and G. Vosselman. 3D information extraction from laser point clouds covering complex road junctions. *The Photogrammetric record*, 24(125):23–36, 2009.

- [42] N. Ettrich. Generation of Surface Elevation Models for Urban Drainage Simulation, 2005. Bericht des Fraunhofer ITWM, Nr. 79.
- [43] N. Ettrich. Surface-sewer coupling and detailed elevation models for accurate urban drainage modelling. In *Proceedings Cost Session Aquaterra Conference 2007, Special Aspects of urban flood managements*, pages 183–196, 2007.
- [44] S. Filin. Surface Clustering from Airborne Laser Scanning Data. In *IAPRS*, volume 34, Graz, Austria, 2002.
- [45] S. Filin and N. Pfeifer. Neighborhood systems for airborne laser data. *Photogrammetric Engineering & Remote Sensing*, 71(6):743–755, 2005.
- [46] S. Filin and N. Pfeifer. Segmentation of airborne laser scanning data using a slope adaptive neighbourhood. *ISPRS Journal of Photogrammetry and Remote sensing*, 60(2):71–80, 2006.
- [47] G. Forlani and C. Nardinocchi. Adaptive filtering of aerial laser scanning data. *International Archives of Photogrammetry, Remote Sensing and Spatial Information Sciences*, 36(3/W52):130–135, 2007.
- [48] R. Frankhauser. Automatic detection of imperviousness in urban areas from digital orthophotos. *Water Science and technology*, 39(9):81–86, 1999.
- [49] M. A. Friedl and C. E. Brodley. Decision tree classification of land cover from remotely sensed data. *Remote Sensing of Environemnt*, 61:130–137, 1997.
- [50] Y. Gao and J. F. Mas. A comparison of the performance of pixel-based and object-based classifications over images with various spatial resolutions. In *Proceedings of GEOBIA, 2008 - Pixels, Objects, Intelligence: GEOgraphic Object Based Image Analysis for the 21st Century*, pages 64–69, University of Calgary, Calgary, Alberta, Canada, 2008.
- [51] R. Gecen and G. Sarp. Road detection from high and low resolution satellite images. In *The Interantional Archives of the Photogrammetry, Remote Sensing and Spatial Inforamtion Sciences*, volume XXXVII, Beijing, China, 2008.
- [52] R. C. Gonzalez and R. E. Woods. *Digital image processing*. Prentice-Hall, Englewood Cliffs, NJ, 2nd edition, 2002.
- [53] S. R. Ha, S. Y. Park, and D. H. Park. Estimation of urban runoff and water quality using remote sensing and artificial intelligence. *Water Science and Technology*, 47(7-9):319–325, 2003.

-
- [54] N. Haala and C. Brenner. Extraction of buildings and trees in urban environments. *ISPRS Journal of Photogrammetry and Remote Sensing*, 54:130–137, 1999.
- [55] E. Haines. *Point in Polygon Strategies*. Ed. Heckbert, Paul. Academic Press, 1994.
- [56] S. Han, J. Heo, H. G. Sohn, and K. Yu. Parallel Processing Method for Airborne Laser Scanning Data Using a PC Cluster and a Virtual Grid. *Sensors*, 9:2555–2573, 2009.
- [57] R. M. Haralick and L. G. Shapiro. Survey: Image segmentation techniques. *Computer Vision, Graphics and Image Processing*, 29(1):100–132, 1985.
- [58] C. Harmann and M. Johns. Voronoi natural neighbour interpolation. In *Senior conference computer geometry class*, Swarthmore college, 2008.
- [59] C. Hatger and C. Brenner. Extraction of Road geometry parameters from Laser scanning and existing databases. In *Proceedings of the ISPRS workshop Laser Scanning*, Dresden, Germany, 2003.
- [60] C. Heipke, H. Mayer, C. Wiedeman, and O. Jamet. Evaluation of automatic road extraction. *International archives of Photogrammetry and Remote Sensing*, XXXII(3/4W2):151–160, 1997.
- [61] J. Hénouin, B. Russo, D. S. Roqueta, R. Sanchez-Diezma, N. Domingo, F. Thomsen, and O. Mark. Urban flood real-time forecasting and modelling: a state-of-the-art review. In *MIKE by DHI Conference- Copenhagen*, September 2010.
- [62] Y. G. Her. *HYSTAR: Hydrology and Sediment transport simulation using Time-Area method*. PhD thesis, Virginia Polytechnique Institute and State University, 2011.
- [63] S. Hinz and A. Baumgartner. Automatic extraction of urban road networks from multi-view aerial imagery. *ISPRS Journal of Photogrammetry and Remote sensing*, 58(1-2):83–98, 2003.
- [64] M. E. Hodgson, J. R. Jensen, J. Tullis, K. D. Riordam, and C. M. Archer. Synergistic Use of LiDAR and Color Aerial Photography for Mapping Urban Parcel Imperviousness. *Photogrammetric Engineering and Remote Sensing*, 69(9):973–980, 2003.

- [65] T. Hofman and J. Boehner. Unsupervised texture segmentation in a deterministic annealing framework. *IEEE Transaction on Pattern Analysis and Machine Intelligence*, 20(8):803–818, 1998.
- [66] X. Hu, C. V. Tao, and Y. Hu. Automatic road extraction from dense urban areas by integrated processing of high resolution imagery and LiDAR data. In *Proceedings of the ISPRS XXth Congress, ISPRS Workshop Commission III*, Istanbul, Turkey, 2004.
- [67] X. Hu and V. Tao. Automatic Extraction of Main Road Centerlines from High Resolution Satellite Imagery Using Hierarchical Grouping. *Photogrammetric Engineering & Remote Sensing*, 73(9):1049–1056, 2007.
- [68] Y. Hu. *Automated Extraction of Digital Terrain Models, Roads and Buildings Using Airborne Lidar Data*. PhD thesis, Department of Geomatics Engineering, University of Calgary, 2003. URL: <http://www.geomatics.ucalgary.ca/links/GradTheses.html>.
- [69] N. M. Hunter, P. D. Bates, S. Neelz, G. Pender, I. Villanueva, N. G. Wright, D. Liang, R. A. Falconer, B. Lin, S. Waller, A. J. Crossley, and D. C. Mason. Benchmarking 2D Hydraulic models for urban flooding. *Water Management*, 161(WMI):13–30, 2008.
- [70] J. R. Jensen. Biophysical remote sensing. *Annals of the Association of the American Geographers*, 73:111–132, 1983.
- [71] J.R. Jensen. *Introductory Digital Image Processing: A Remote Sensing Perspective*. Prentice-Hall, New Jersey, USA, 2005.
- [72] M. Ji and J. R. Jensen. Effectiveness of subpixel analysis in detecting and quantifying urban imperviousness from Landsat Thematic Mapper Imagery. *Geocarto International*, 14(4):31–39, 1999.
- [73] M. Kada and N. Haala. Integration of Street Networks and LiDAR for modeling and visualization of terrain data. Proceedings of Asian Conference on Remote Sensing 25th. In *Proceedings of Asian Conference on Remote Sensing 25th*, pages 256–261, Chiang Mai, Thailand, 2004.
- [74] P. Keller. *Adaptive extraction and representation of geometric structures from unorganized 3D point sets*. PhD thesis, Department of Computer Science, University of Kaiserslautern, 2009. URL: <https://kluedo.ub.uni-kl.de/files/2158/diss-book.pdf>.

- [75] R. L. Kettig and D. A. Landgrebe. Classification of Multispectral Image Data by Extraction and Classification of Homogeneous Objects. *IEEE Transactions on Geoscience Electronics*, GE-14(1):19–26, 1976.
- [76] M. Knabenschuh and B. Petzold. Data post-processing of Laser Scan Data for countywide DTM production. In *D. Fritsch and R. Spiller (eds). Photogrammetric week 99*, Wichmann Verlag, Heidelberg, 1999.
- [77] A. Kobler and P. Ogrinc. Rein Algorithm and the influence of point cloud density on nDSM and DEM precision in a Submediterranean forest. In *ISPRS Workshop on Laser Scanning and SilviLaser 2007*, Espoo, Finland, 2007.
- [78] R. De koka, T. Schneider, and U. Ammer. Object-based classification and applications in the Alpine forest environment. In *Fusion of Sensors data, Knowledge sources and algorithms, Proceedings of the joint ISPRS/Earsel Workshop*, Valladolid , Spain, 1999.
- [79] K. Krauss and N. Pfeifer. Determination of terrain models in wooded areas with airborne laser scanner data. , 53:193–203. *ISPRS Journal of Photogrammetry and Remote Sensing*, 53:193–203, 1998.
- [80] R. Lawrence, A. Bunn, S. Powell, and M. Zambon. Classification of remote sensed imagery using stochastic gradient boosting as a refinement of classification tree analysis. *Remote sensing of Environment*, 90:331–336, 2004.
- [81] H. Li, H. Gu, Y. Han, and J. Yang. An Efficient Multiscale SRMMHR (Statistical Region Merging and Minimum Heterogeneity Rule) Segmentation Method for High-Resolution Remote Sensing Imagery. *IEEE Journal of selected topics in applied earth observations and remote sensing*, 2(2):67–73, 2009.
- [82] X. Liu. (Airborne LiDAR for DEM generation: Some critical issues. *Progress in Physical Geography*, 32(1):31–49, 2008.
- [83] S. K. Lodha, D. M Fitzpatrick, and D. P. Helmbold. Aerial LiDAR data classification using AdaBoost. In *Proceedings of the 6th Int. Conf. on 3D digital imaging and modeling, IEEE Computer Society*, pages 435–442, Washington, DC, USA, 2007.
- [84] Maas. The potential of height texture measures for the segmentation of airborne laser scanner data. In *Fourth International Airborne Remote Sensing Conference and Exhibition/ 21st Canadian Symposium on Remote Sensing*, pages 155–161, Ottawa, Ontario, Canada, 1999.

-
- [85] O. Mark, S. Weesakul, C. Apirumanekul, S. Boonya-Aroónet, and S. Djordjević. Potential and limitations of 1D modeling of urban flooding. *Journal of Hydrology*, 299:284–299, 2004.
- [86] K. Marks and P. Bates. Integration of high-resolution topographic data with floodplain flow models. *Hydrological processes*, 14:2109–2122, 2000.
- [87] T. R. Martha and N. Kerle. Segment optimisation for object-based landslide detection. In *Geographic Object-based image analysis*, Ghent, Belgium, 2010.
- [88] D. C. Mason, M. S. Horitt, N. M. Hunter, and P. D. Bates. Use of fused airborne scanning laser altimetry and digital map data for urban flood modelling. *Hydrological processes*, 21:1436–1447, 2007.
- [89] L. Matikainen, H. Kaartinen, and J. Hyypä. Classification tree based building detection from laser scanner and aerial image data. In *ISPRS Workshop on Laser Scanning 2007 and SilviLaser 2007*, Espoo, Finland, 2007.
- [90] J. B. Mena. State of the art on automatic road extraction for GIS update: a novel classification. *Pattern Recognition Letters*, 24:3037–3058, 2003.
- [91] S. W. Myint and D. Stow. An object-oriented pattern recognition approach for urban classification. In X. Yang (Editor), *Urban Remote Sensing, Monitoring, Synthesis and Modeling in the Urban Environment*, 2010. John Wiley & Sons (in press).
- [92] C. Nardinocchi, G. Forlani, and P. Zingaretti. Classification and filtering of laser data. *IAPRS*, 34(3/W13):79–86, 2003.
- [93] K. Navulur. *Multispectral image analysis using object-oriented paradigm*. Boca Raton, FL: CRC Press, Taylor and Frances Group, 2007.
- [94] S. Neelz and G. Pender. The Influence of errors in digital terrain models on flood flow routes. In *Proceedings of River Flow*, Lisbon, 2006.
- [95] S. Neelz, G. Pender, I. Villanueva, M. Wilson, N. G. Wright, P. Bates, D. Mason, and C. Whitlow. Using remotely sensed data to support flood modelling. *Proceedings of the Institution of the Civil Engineers, Water Management*, 159(1):79–86, 2006.
- [96] A. P. Nicholas and C. A. Mitchell. Numerical simulation of overbank processes in topologically complex floodplain environments. *Hydrological Processes*, 17(4):727–746, 2003.

- [97] J. S. Park and R. A. Saleh. A comprehensive survey of extracting techniques of linear features from remote sensing imagery Santa Barbara. <http://www.ncgia.ucsb.edu/ncrst/about/news/ncgia.html>, August 2001. Meeting on Road Centerline Extraction & Maintenance.
- [98] N. Pfeifer and C. Brieseab. Geometrical Aspects of Airborne Laser Scanning and Terrestrial Laser Scanning. *IAPRS*, XXXVI(3/W52), 2007.
- [99] N. Pfeifer, M. Rutzinger, F. Rottensteiner, W. Muecke, and M. Hollaus. Extraction of building footprints from airborne laser scanning: comparison and validation techniques. In *Urban Remote Sensing Joint Event*, Paris, 2007.
- [100] K. Price. Road grid extraction and verification. *International Archives of Photogrammetry, Remote Sensing*, 32:101–106, 1999.
- [101] F. Ravagnani, A. Pellegrinelli, and M. Franchini. Estimation of Urban Impervious Fraction from Satellite Images and Its Impact on Peak Discharge Entering a Storm Sewer System. *Water Resource management*, 23:1893–1915, 2009.
- [102] M. K. Ridd. Exploring a V-I-S (vegetation-impervious surface-soil) model for urban ecosystem analysis through remote sensing-comparative anatomy for cities. *International Journal of Remote Sensing*, 16(12):2165–2185, 1995.
- [103] M. Roggero. Airborne laser scanning: clustering in raw data. *International Archives of Photogrammetry and Remote sensing and Spatial Information Sciences*, 34(3/W4):227–232, 2001.
- [104] M. Roggero. Object segmentation with region growing and principal component analysis. In *International Archives of Photogrammetry and Remote Sensing*, volume XXXIV, pages 289–294, Graz, Austria, 2002.
- [105] R. Romanowicz and K. Beven. Estimation of flood inundation probabilities as conditioned on event inundation maps. *Water Resources Research*, 39(3):1073, 2003.
- [106] L. A. Rossman, R. E. Dickinson, T. Schade, C. Chan, E. H. Burgess, and W. C. Huber. SWMM5: The USEPA’s newest tool for urban drainage analysis. In *10th ICUD*, Copenhagen, 2005.
- [107] Rottensteiner. Status and further prospects of object extraction from Image and Laser data. In *2009 Urban Remote Sensing Joint Event*, Shanghai, IEEE computer Society, 2009.

-
- [108] S. R. Safavian and D. Landgrebe. A survey of decision tree classifier methodology. *IEEE transaction on Systems, Man, and Cybernetics*, 21(3):660–674, 1991.
- [109] M. Salah, J. Trinder, A. Shaker, M. Hamed, and A. Elzagheer. Aerial images and LiDAR data fusion for automatic feature extraction using the self-organizing map (SOM) classifier. In *Laser Scanning 2009, IAPRS*, volume XXXVII, Paris, France, 2009.
- [110] P. Sapkota. Segmentation of coloured point cloud data. MSc thesis, 2007. ITC, The Netherlands.
- [111] T. G. Schmitt, M. Thomas, and N. Ettrich. Analysis and modelling of flooding in urban drainage systems. *Journal of Hydrology*, 299:300–311, 2004.
- [112] T. G. Schmitt, M. Thomas, and N. Ettrich. Assessment of Urban flooding by dual drainage simulation model RisUrSim. *Water Science and Technology*, 52(5):264–274, 2005.
- [113] G.M. Senseman, C.F. Bagley, and S.A. Tweddale. Accuracy Assessment of the Discrete Classification of Remotely-Sensed Digital Data for Landcover Mapping. In *Construction Engineering Research Laboratories, USACERL Technical Report EN-94/04*, US Army Corps Of Engineers, 1995.
- [114] J. Serra. *Image Analysis and Mathematical Morphology*. Academic Press, London, 1982.
- [115] J. Shan and A. Shampath. Urban DEM generation from raw LiDAR data: a labelling algorithm and its performance. *Photogrammetric Engineering & Remote Sensing*, 71(2):217–226, 2005.
- [116] J. Shan and A. Shampath. Building roof segmentation and reconstruction from LiDAR data point clouds using clustering techniques. *International Archives of Photogrammetry, Remote Sensing and Spatial Information Sciences*, Vol. XXXVII(B3a):279–284, 2008.
- [117] R. Sibson. *A brief description of natural neighbour interpolation*. In V Barnett, editor, *Interpreting multivariate data*. Wiley, New York, USA, 1981.
- [118] G. Sithole. Filtering of laser altimetry data using a slope adaptive filter. *International archives of Photogrammetry, Remote Sensing and Spatial Information Sciences*, 34(3/W4):203–210, 2001.

- [119] G. Sithole and G. Vosselman. Experimental comparison of filter algorithms for bare-earth extraction from airborne laser scanning point clouds. *ISPRS Journal of Photogrammetry and Remote Sensing*, 59(1–2):85–101, 2004.
- [120] M. O. Smith, P. E. Johnson, and J. B. Adams. Quantitative determination of mineral types and abundances from reflectance spectra using principal component analysis. *Journal of Geophysical Research*, 90:792–804, 1985.
- [121] J. M. Stoker, S. K. Greenlee, D. B. Gesch, and J. C. Menig. CLICK: The New USGS Center for Lidar Information Coordination and Knowledge. *Photogrammetric Engineering & Remote Sensing*, 72(6):613–616, 2006.
- [122] J. A. Tullis and J. R. Jensen. Expert system house detection in high spatial resolution imagery using size, shape and context. *Geocarta International*, 18(1):5–15, 2003.
- [123] K. D. Vivienne, S. Arthur, and G. Pender. The use of a LiDAR DEM in modelling sewerage derived urban flood wave routing. In *11th International Conference on Urban Drainage*, Edinburgh, Scotland, 2008.
- [124] T. Vögtle and E. Steinle. 3D modeling of buildings using laser scanning and spectral information. In *The International Archives of the Photogrammetry and Remote Sensing*, volume XXXIII, pages 927–934, Amsterdam, The Netherlands, 2000.
- [125] Z. Vojinovic, S. D. Seyoum, J. M. Mwalwaka, and R. K. Price. Effects of model schematisation, geometry and parameter values on urban flood modelling. *Water Science and Technology*, 63(3):462–467, 2011.
- [126] G. Vosselman. 3d reconstruction of roads and trees for city modelling. In *Proceedings of the ISPRS working group III/3 workshop: 3-D reconstruction from airborne laser scanner and InSAR data*, volume 34, Institute of Photogrammetry and Remote Sensing Dresden University of Technology, Dresden, Germany, 2003.
- [127] G. Vosselman, B. G. H. Gorte, G. Sithole, and T. Rabbani. Recognising Structure in Laser Scanner Point Clouds. In *International Archives of Photogrammetry, Remote Sensing and Spatial Information Sciences*, volume 46(8/W2), pages 33–38, Freiburg, Germany, 2004.
- [128] G. Vosselmann. Slope-based filtering of laser altimetry data. *Int. arch. Photogrammetry Remote Sensing*, 33(B3/2):935–942, 2000.

- [129] M. Vyas. Advantages of LiDAR in Flood Modelling and Important Parameters for LiDAR . http://www.gisdevelopment.net/application/natural_hazards/floods/mi08_206.htm, 2008.
- [130] J. Wang and J. Shan. Segmentation of LiDAR point clouds for building extraction. In *ASPRS 2009 Annual Conference*, Baltimore, Maryland, 2009.
- [131] Y. Wang and J. Trinder. Road Network Extraction by Hierarchical Grouping. *IAPRS*, 33(B3/2):943–949, 2000.
- [132] C. Wiedemann and H. Ebner. Automatic Completion and Evaluation of Road Networks. In *International Archives of Photogrammetry and Remote Sensing*, volume XXXIII, pages 979–986, 2000.
- [133] C. Wu and A. T. Murray. Estimating impervious surface distribution by spectral mixture analysis. *Remote sensing of environment*, 84(4):493–505, 2002.
- [134] S. Xiaoxia, Z. Jixian, and L. Zhengjun. A comparison of object-oriented and pixel-based classification approaches using Quickbird imagery. In *Proceedings of International Symposium on Spatio-temporal Modeling, Spatial Reasoning, Analysis, Data Mining and Data Fusion*, Beijing, China, 2005.
- [135] K. Zaksek and N. Pfeifer. An improved morphological filter for selecting relief points from a LiDAR point cloud in steep areas with dense vegetation. In *Ljubliana, Slovenia, and Innsbruck, Austria: Institute of Anthropological and Spatial studies, Scientific research centre of the Slovenian Academy of sciences and arts, and Institute of Geography, Innsbruck University*, 2006.
- [136] C. Zhang. Towards an operational system for automated updating of road databases by integration of imagery and geodata. *ISPRS Journal of Photogrammetry and Remote sensing*, 58:166–186, 2004.
- [137] C. Zhang, E. Baltsavias, and A. Gruen. Knowledge-based image analysis for 3D roadreconstruction. *Asian Journal of Geoinformatics*, 1(4):3–14, 2001.
- [138] K. Zhang, J. Yan, and S. C. Chen. Automatic construction of building footprints from airborne LiDAR data. *IEEE Transaction on Geoscience and Remote Sensing*, 44(9):2523–2533, 2007.
- [139] K. Q. Zhang, S. C. Chen, D. Whitman, M. L. Shyu, J. H. Yan, and C. C. Zhang. A progressive morphological filter for removing non-ground measurements from airborne LiDAR data. *IEEE transaction on Geoscience and Remote sensing*, 41:872–882, 2003.

- [140] P. Zhu, Z. Lu, X. Chen, K. Honda, and A. Eiumnoh. Extraction of City Roads Through Shadow Path Reconstruction Using Laser Data. *Photogrammetric Engineering & Remote Sensing*, 70(12):1433–1440, 2004.
- [141] http://en.wikipedia.org/wiki/Expert_system. accessed 10th April, 2011.
- [142] <http://www.infoweblinks.com>. accessed 11th April, 2011.
- [143] http://en.wikipedia.org/wiki/Cluster_analysis. accessed 29th March, 2011.
- [144] http://en.wikipedia.org/wiki/Data_mining. accessed 20th February, 2011.
- [145] URL: <http://alienryderflex.com/polygon>. accessed 25th March, 2011.
- [146] Delft Hydraulics Software. <http://delftsoftware.wldelft.nl>.
- [147] DHI Software. <http://www.dhi.org>.
- [148] Glossary of Remote Sensing Terms. <http://ccrs.nrcan.gc.ca/glossary>.
- [149] MOUSE, DHI Software. <http://www.dhigroup.com>.
- [150] PA Storm Water Management Model (SWMM). <http://www.epa.gov>.
- [151] Reference Manual PCSWMM 2002. <http://www.chiwater.com/Support/PCSWMM.NET/productupdates.asp>.
- [152] XP Software Inc. (2002), XP-SWMM Technical Description, Portland. <http://www.xpsoftware.com.au/products/pdfs/SWMMTech%20Description.pdf>.
- [153] SWMM Software. <http://www.epa.gov/ednnrmrl/models/swmm>, 1988.
- [154] INFOWORKS Software. <http://www.mwhsoft.com>, 2002.
- [155] MATLAB SOFTWARE. <http://www.mathworks.com>, 2009.
- [156] Definiens 2010, eCognition 8.0 User Guide, Definiens Imaging GmbH, Munich, Germany, 2010.
- [157] ESRI. <http://www.esri.com>, 2010.

Curriculum Vitae

Name: Md. Aktaruzzaman



Education

2008 – 2011: PhD in Remote Sensing, Geospatial data analysis and Flood modelling.
Department of Civil Engineering, University of Kaiserslautern, Germany.

2006-2008: University of Southampton, UK, Lund University, Sweden and ITC, the Netherlands. Master of Science (M.Sc.) in Geo-information Science and Earth Observation for Environmental modelling and management in March 2008.

1999-2004: Bangladesh University of Engineering and Technology, Dhaka.
Bachelor of Science (BSc.) in Civil Engineering in December 2005.

Career History

PhD researcher at IRTG, University of Kaiserslautern, Germany.
(April 2008- September 2011)

Visiting Researcher at GeoDa centre, Arizona State University, USA.
(August-December, 2009) and (September –December, 2010)

Student assistant at Institute of Engineering Design, University of Braunschweig,
Germany. (September 2005 - June2006)

Assistant Engineer at National Centre for Earthquake Engineering (NCEE), BUET, Dhaka,
Bangladesh. (January 2005 – August 2005)

**Schriftenreihe des Fachgebietes Siedlungswasserwirtschaft
der Technischen Universität Kaiserslautern**

- Band 1: Festschrift anlässlich des 60. Geburtstages von Prof. Dr.-Ing. K. Jacobitz, Kaiserslautern 1987 EUR 20,--
- Band 2: Horster, Monika: Untersuchungen zur Stickstoffelimination in Belebungsanlagen mit separater Belüftung des Rücklaufschlammes, Dissertation Kaiserslautern 1990 EUR 12,--
- Band 3: Festschrift zum 10-jährigem Jubiläum des Fachgebietes Siedlungswasserwirtschaft an der Universität Kaiserslautern: Vorträge zu aktuellen Problemen der Siedlungswasser- und Abfallwirtschaft am 25.10.1991, Kaiserslautern 1992 EUR 10,--
- Band 4: Wagner, Wolfgang: Optimierung der Sicherheit und Zuverlässigkeit von Kläranlagen auf der Basis von Risikoanalysen, Dissertation Kaiserslautern 1992 vergriffen
- Band 5: Burde, Michael: Vorsorgende und langfristige Grundwassersicherung durch Ausweisung von Grundwasservorranggebieten als Aufgabe von Raumplanung und Fachplanung, Dissertation Kaiserslautern 1992 EUR 15,--
- Band 6: Welker, Antje: Die Belastung von Reststoffen aus der Papierindustrie mit halogen-organischen Verbindungen – Aufklärung der chemischen Zusammensetzung und Folgerungen für die Reststoffentsorgung, Dissertation Kaiserslautern 1992 EUR 15,--
- Band 7: Vom Stadtbauwesen zur Siedlungswasserwirtschaft; Festschrift zur Verabschiedung von Prof. Dr.-Ing. K. Jacobitz, Kaiserslautern November 1995 EUR 15,--
- Band 8: Neuer Umgang mit Regenwasser in Siedlungen, Beiträge der 4. Umwelttage Kaiserslautern, Kaiserslautern 1995 EUR 20,--
- Band 9: Steinmetz, Heidrun: Einfluß von Abwasserinhaltsstoffen, Stoffwechselprozessen und Betriebsparametern von Belebungsanlagen auf den Sauerstoffeintrag in Abwasser-Belebtschlamm-Gemische, Dissertation Kaiserslautern 1996 EUR 15,--
- Band 10: Hansen, Joachim: Der Einsatz von Fuzzy Control für Regelungsaufgaben im Bereich der Nährstoffelimination in kommunalen Kläranlagen, Dissertation Kaiserslautern 1997 EUR 15,--
- Band 11: Fuzzy Control und Neuronale Netze zur Optimierung der Stickstoff- und Phosphorelimination, Beiträge der Fachtagung zum Einsatz innovativer Methoden der Steuerungstechnik in der Abwasserbehandlung, Kaiserslautern 1998 EUR 20,--
- Band 12: Dynamische Simulation als Werkzeug zur optimierten Planung und Betriebsführung von Abwasserreinigungsanlagen, Kaiserslautern 1999 EUR 20,--

- Band 13: Zettl, Ulrike: Einsatz der Dynamischen Simulation als Bemessungshilfe für Kläranlagen in Weinbaugebieten, Dissertation Kaiserslautern 2000
EUR 20,--
- Band 14: Einsatz der SBR-Technologie in der kommunalen und industriellen Abwasserbehandlung, Kaiserslautern 2001
EUR 20,--
- Band 15: Regenwasserbehandlung – Anwendungspraxis und Perspektiven, Kaiserslautern 2002
EUR 20,--
- Band 16: Leinweber, Ulla: Anforderungen an die integrierte Modellierung von Entwässerungssystem und Kläranlage, Dissertation Kaiserslautern 2002
EUR 20,--
- Band 17: Kasting, Ulrich: Reinigungsleistung von zentralen Anlagen zur Behandlung von Abflüssen stark befahrener Straßen, Dissertation Kaiserslautern 2003
EUR 20,--
- Band 18: Blähschlamm, Schwimmschlamm und Schaum in kommunalen und industriellen Abwasserbehandlungsanlagen, Kaiserslautern 2003
EUR 20,--
- Band 19: Wiese, Jürgen: Entwicklung von Strategien für einen integrierten Betrieb von SBR-Kläranlagen und Mischkanalisationen – Simulation und Großtechnik, Dissertation Kaiserslautern 2005
EUR 20,--
- Band 20: Welker, Antje: Schadstoffströme im urbanen Wasserkreislauf – Aufkommen und Verteilung, insbesondere in den Abwasserentsorgungssystemen, Habilitation Kaiserslautern 2005
EUR 20,--
- Band 21: Integrale Betrachtung von Kanalnetz, Kläranlage und Gewässer, Kaiserslautern 2005
EUR 20,--
- Band 22: Klepischewski, Kai: Analyse und modelltechnische Nachbildung der Reinigungswirkung eines kombinierten Bauwerks zur Mischwasserbehandlung, Dissertation Kaiserslautern 2006
EUR 20,--
- Band 23: Dittmer, Ulrich: Prozesse des Rückhaltes und Umsatzes von Kohlenstoff- und Stickstoffverbindungen in Retentionsbodenfiltern zur Mischwasserbehandlung, Dissertation Kaiserslautern 2006
EUR 20,--
- Band 24: Wozniak, Renata: Ermittlung von Belastungsgrenzen an Bodensubstraten zu weitergehenden Mischwasserbehandlung in Retentionsbodenfiltern, Dissertation Kaiserslautern 2007
EUR 20,--
- Band 25: siwawi 2030 – Themen und Lösungsansätze für die nächsten 25 Jahre, Kaiserslautern 2006
vergriffen
- Band 26: Ökoeffizienz in der Wasserwirtschaft – Schwerpunkt Energieoptimierung von Kläranlagen
vergriffen
- Band 27: Illgen, Marc: Das Versickerungsverhalten durchlässig befestigter Siedlungsflächen und seine urbanhydrologische Quantifizierung, Dissertation Kaiserslautern 2009
EUR 20,--

- Band 28: KOMPLETT – Ein innovatives System zur Schließung von Wasser- und Stoffkreisläufen EUR 20,--
- Band 29: Md. Aktaruzzaman: High Resolution Digital Surface Model (DSM) to Support Modelling of Urban Flooding, Dissertation Kaiserslautern 2011 EUR 20,--
- Band 30: Schlammfaulung statt aerober Stabilisierung – Trend der Zukunft? EUR 20,--
- Band 31: Meyer, Daniel: Modellierung und Simulation von Retentionsbodenfiltern zur weitergehenden Mischwasserbehandlung, Dissertation Kaiserlautern 2011 EUR 20,--